Doctoral Dissertation

Development of the measurement system of biological tissue optical properties for medical laser applications

Norihiro Honda

January 2013

Graduate School of Engineering,
Osaka University

Doctoral Dissertation

Development of the measurement system of biological tissue optical properties for medical laser applications

Norihiro Honda

January 2013

Graduate School of Engineering,
Osaka University

Director

Professor Kunio Awazu

Reviewer

Professor Shigehiro Nishijima

Professor Takayoshi Norimatsu

Abstract

Various laser devices have been applied as a tool in surgery and medicine, however the side effects have been reported. For realization of the safety and effective laser medicine, the determination of optical properties of biological tissues is important. In past years, a host of investigators have been reported values of the optical properties for a variety of tissues at a variety of wavelengths. However, there are a few reports on optical properties in a wide wavelength range and on changes of optical properties by laser treatments (laser coagulation therapy, photodynamic therapy (PDT), etc.). Objective of this study is the development of the measurement system of optical properties in a wide wavelength range to analyze the interaction between biological tissues and laser treatment for proposal of the optimal laser treatment planning.

The measurement system of the biological tissue optical properties in the wavelength range of 350–2100 nm by using a double integrating sphere apparatus and an inverse Monte Carlo (MC) technique have developed. Consequently, the optical properties measurement system could measure the optical properties conveniently and accurately.

The optical properties of laser treated biological tissue, which measured by the developed optical properties measurement system are presented. The optical properties of the tissue after laser coagulation were discussed. After the tissue coagulation, the optical properties changed. The effective laser setting during laser irradiation, which considering the optical properties change is discussed.

The optical properties of the tumor tissue and its change after PDT are discussed. The reduced scattering coefficient of tumor tissues increased after PDT. The optical properties change results in the optical penetration depth decreased after PDT. For more effective PDT, the optical properties change after PDT is needed to consider to setting the optimal irradiation parameters.

The optical properties of the Japanese skin tissue are discussed. The optical properties of Japanese skin tissue are measured and the thermal effect is simulated with MC technique to estimate the safety in laser therapy. The simulation results indicated that the probabilities of side effect of Japanese skin tissue by laser irradiation with a wavelength of 755 nm is higher than the Caucasian skin tissue. It is revealed that the side effect is able to control quantitatively by optimization of laser settings with a simulation and optical properties of Japanese skin tissue.

Contents

List of Acronyms

5-ALA	5-amino-levulinic acid
AD	adding-doubling
EVLA	endovenous laser ablation
LITT	laser induced thermotherapy
LLC	Lewis lung carcinoma
MC	Monte Carlo
NIR	near infrared
PDD	photodynamic diagnosis
PDT	photodynamic therapy
PpIX	protoporphyrin IX

Chapter 1
Introductions and Background

The goal of this dissertation is to answer the fundamental question "What is needed to carry out laser therapy or diagnosis more effectively and safely?" Since its introduction nearly 50 years ago, laser therapy remains the way as less invasive treatment for many diseases. Despite widespread use of lasers in medicine, it remains largely unknown how its benefits and deleterious side effects relate to parameters of laser treatment and subsequent healing. Since the light distribution in a tissue is dependent on its optical properties, the fundamental problem naturally splits into two related questions: "What are the optical properties of a tissue and how might they be measured?" and "What is the light distribution during irradiation in a tissue with known optical properties and the interactions of light with biological tissue vary with wavelength, pulse duration and intensity?"

In Chapter 2, the optical properties measurement system by using a double integrating sphere optics and an inverse Monte Carlo (MC) technique are developed. In Chapter 3, the optical properties of the tissue after laser coagulation were measured to estimate more effective laser irradiation parameters. In Chapter 4, the optical properties of the tumor tissues after photodynamic therapy (PDT) are presented. In Chapter 5, the optical properties of the Japanese skin tissue and the simulation of the photo-thermal interaction based on the skin tissue optical properties are presented. In the last chapter, the summary of this doctoral dissertation is described.

1.1 Motivation

Determination of tissue optical properties is fundamental for application of laser in either therapeutics or diagnostics procedures. Since being inventing by Maiman in 1960, laser systems have been applied as a tool in medicine. Recent technological advancements in the photonics industry have spurred real progress toward the development of clinical function imaging and surgical and therapeutic systems. Laser procedure often take less time and cost less money than traditional surgery. Steady growth in medical laser technology can be largely traced to two sources: innovation in the field and popular demand for procedures involving laser treatment. Lasers are generally becoming smaller, more precise and easier to use, to the benefit of both the medical field and the aging population alike.

Optical imaging techniques could be cheaper, less invasive and less toxic, because light is non-ionizing compared with the previous techniques. Of course, tissue is far from transparent to visible and near infrared (NIR) wavelengths when compared to much shorter wavelengths (X-rays), or to much longer wavelengths (radio waves). Therefore extraordinary measures must be taken to derive useful diagnostic imaging information from these wavelengths of light. Information may be acquired from photons that are scattered, from photons that are absorbed, and from photons that are re-emitted after being absorbed in tissue. Examples of the first class of techniques are optical coherence tomography[1] *in vivo* confocal microscopy[2], and light scattering spectroscopy[3]. Examples of the second class are the pulse oximeter for measuring blood oxygenation[4], diffuse optical tomography[5] and photoacoustic imaging and spectroscopy[6]. Examples of the third class include autofluorescence imaging[7], *in vivo* confocal fluorescence microscopy[8], and Raman spectroscopy[9].

Optical imaging is capable of producing information on the spatial location of lesions with varying degrees of resolution and by employing spectral analysis information can be obtained on the identity and relative concentration of tissue molecular constituents. One goal of optical imaging is the "optical biopsy". Because in principle optical imaging has the potential to provide the same sub-micron resolution that is taken for granted in optical microscopy, some investigators have tried to replicate diagnosis using non-invasive optical biopsies. This is more valuable when one considers that in conditions like Barrett's esophagus scores of random excisional biopsies may be taken, and in other anatomical locations such the coronary arteries taking any biopsies is impossible.

In practice since tissue is highly opaque the light is often delivered into the body and diagnostic information is retrieved via fiber optic catheters that can insert into hollow organs via endoscopes and even threaded through blood vessels. Another active area of research in optical diagnostic imaging is the use of optical contrast agents. These are exogenous chemicals that can act as optical reporters by such means as high scattering, fluorescence, phosphorescence, photoacoustic properties, etc.

Optical diagnosis relies on the structural and biochemical differences between cancer tissue and normal tissue that can be probed with visible or NIR light. Cancerous cells are more active and reproduce at an abnormally high rate. They also tend to have larger and more numerous nuclei. On the tissue level, tumors have immature collagen as well as a pronounced network of immature blood vessels due to angiogenesis, and therefore higher blood content. Exogenous substances that accumulate in tumor tissue can enhance the optical contrast between tumors and normal surrounding tissue. Fluorescent dyes have been developed that

can be used to delineate tumor borders or detect otherwise invisible lesions. Fluorescence markers might be in favor to illuminate cancerous tissue. In resent years, photodynamic diagnosis (PDD) for high-grade malignant gliomas have received increasing attention. In neurosurgery, several investigators have used photodynamic agents, such as protoporphyrin IX (PpIX) induced by intravesical administration of 5-amino-levulinic acid (5-ALA), to distinguish between malignant and benign tissue[10].

In PDD, the utility of ALA-induced PpIX for fluorescence guided resection of brain tumors, the visible fluorescence was highly predictive of tumor tissue, with a positive predictive value of 1.00 (ref. 10). This high predictive value of visible fluorescence for tumor tissue helps explain the excitement in the field for this technology. Nevertheless, it is observed that ALA-induced PpIX display low sensitivity for tumor tissues, with a positive predictive value of 0.85. And, it is appeared that differential trends in PpIX fluorescence as a function of tumor aggressiveness. It is known that a differential accumulation of PpIX in tumor types. However, mechanism of PpIX accumulation difference between tumor and normal is unknown. It is important to reveal the contribution of the fluence of excitation light in the tumor and surround tissue to fluorescence from the photosensitizer in PDD.

Therapeutic usage mostly includes application in laser surgery, such as PDT[11], laser-induced thermotherapy (LITT)[12], endovenous laser ablation (EVLA)[13]. PDT is a modality for the treatment of cancer involving excitation of nontoxic photosensitizers with harmless visible light-producing cytotoxic reactive oxygen species. Recently, PDT has been studied to apply the brain tumor in neurosurgery. For example, the safety and efficiency of PDT using talaporfin sodium in patients with surgically, completely unresectable malignant gliomas with invasion into the eloquent areas of the brain associated with language and motor functions are invesitagated[14]. PDT in addition to surgical resection achieved better therapeutic results than conventional protocols, especially in patients with newly diagnosed malignant gliomas. The knowledge of treatment depth and the treatmentable area are the one of the considerable parameters to control the damage to surrounding of tumor region for realization of safety and efficiency of PDT in neurosurgery. However, it is difficult to acquire the clinical data of PDT to the normal tissue in the view of ethics and the number of patients. The parameters of efficiency of PDT are an oxygen concentration, a drug concentration, and the light fluence in tissues. To estimate the treatment depth and treatment region in PDT, the spatial distribution of fluence in tissue is needed to understand.

Laser coagulation remains the standard of care for many ocular disorders[15]. Despite widespread use of lasers in retinal therapy, it remains largely unknown how its benefits and

deleterious side effects relate to parameters of laser treatment and subsequent retinal healing. It can reduce a patient's night vision or his/her ability to function well when going from a lighted environment to a darkened one. It can cause a loss of peripheral vision or blind spots in a person's central vision, depending upon where the laser burns are placed. The laser burns themselves can (rarely) become a site for the development of abnormal blood vessels beneath the retina, leading to vision loss. Finally, and most importantly, sometimes laser therapy does not work, and patients lose vision despite receiving timely treatment[16]. Thus strategies to reduce untoward effects of laser therapy while maintaining clinical benefit are highly desirable. And, thermal laser therapy has proved to be successful in treating or palliating solid malignant tumors at various site[17].

There are advantage and disadvantage in the phototherapy and diagnosis using light or laser[15]. Doctors can use the laser as a tool, and he must choice optimal a wavelength, a beam power, a spot size, and an irradiation time. Since small differences in any of these parameters can determine whether an application is efficacious or disastrous, some a priori knowledge about the effects of each parameter is needed. Tomographic imaging consists of directing X-rays at an object from multiple orientations and measuring the decrease in intensity along a series of linear paths. This decrease is characterized by Beer's Law, which describes intensity reduction as a function of X-ray energy, path length, and material linear attenuation coefficient[18]. A specialized algorithm is then used to reconstruct the distribution of X-ray attenuation in the volume being imaged. As in all radiotherapies, it is important to perform extensive computational dosimetry studies on a patient-specific basis in order to deliver an optimum treatment[19]. Similarly, many diagnostic and therapeutic applications require knowledge of the light flux through tissue. Photons that enter tissue are scattered once or multiple times until they either escape or are absorbed (Figure 1.1). Computer simulations that track the movement of photons through biological tissues are based on the absorption and scattering properties of each specific tissue. Then the knowledge of tissue optical properties is of great importance for the interpretation and quantification of the diagnostic data, and for the prediction of light distribution and absorbed energy for therapeutic and surgical use.

1.2 Optical properties measurement

Methods for determining the optical parameters of tissues can be divided into two large groups, direct and indirect methods[20]. Direct methods include those based on some fundamental concepts and rules such as Bouguer-Beer-Lambert law, the single-scattering

phase function for thin samples, or the effective light penetration depth for slabs. The parameters measured are the collimated light transmission T_c and the scattering indicatrix (angular dependence of the scattered light intensity) for thin samples or the fluence rate distribution inside a slab. The normalized scattering indicatrix is equal to the scattering phase function. These methods are advantageous in that they use very simple analytic expressions for data processing. Their disadvantages are related to necessity to strictly fulfill experimental conditions dictated by the selected model (single scattering in thin samples, exclusion of the effects of light polarization, and refraction at cuvette edges, etc.); in the case of slabs with multiple scattering, the recording detector (usually a fiber light guide with an isotropic scattering ball at the tip end) must be placed far from both the light source and the medium boundaries.

Indirect methods obtain the solution of the inverse scattering problem using a theoretical model of light propagation in a medium. They are in turn divided into iterative and non-iterative models. The former uses equations in which the optical properties are defined through parameters directly related to the quantities being evaluated. The latter are based on the two-flux Kubelka-Munk model and multiflux models[21]. In indirect iterative methods, the optical properties are implicitly defined through measured parameters. Quantities determining the optical properties of a scattering medium are enumerated until the estimated and measured values for reflectance and transmittance coincide with the desired accuracy. These methods are cumbersome, but the optical models currently in use may be even more complicated than those underlying non-iterative methods, such as the diffusion theory, inverse adding-doubling (AD)[22,23], and inverse MC methods[24–26].

In vitro evaluation is most often achieved by the double integrating sphere method combined with collimated transmittance T_c measurements. The total transmittance $T_t = T_c + T_d$ (T_d being diffuse transmittance), and diffuse reflectance R_d are measured with the double integrating spheres. The optical parameters of the tissue are deduced from these measurements using different theoretical expressions or numerical methods (two-flux and multiflux models, the inverse MC or inverse AD methods) relating the absorption coefficient μ_a, scattering coefficient μ_s, and anisotropy factor g to the parameters being investigated[27].

1.3 Definition and nomenclature

In this section, the nomenclature used in this dissertation is presented. In Section 1.3.1, definition on absorption coefficient is introduced. The next section introduces the scattering coefficient. In Section 1.3.3, the phase function is presented.

1.3.1 Absorption coefficient

Tissue is assumed to be a random turbid medium, with variations in the optical properties small enough to prevent localized absorption. In other words, tissue is considered to have volumetric scattering and absorption properties rather than being composed of discrete scattering and absorption centers distributed in a non-scattering, non-absorbing medium. The advantage to the distributed scattering center approach is that for perfect spheres the phase function is known, however there is little similarity between perfect spheres and tissue. Light-medium interaction due to absorption is described by the absorption coefficient, essentially defined as the cross-sectional area per unit volume of medium.

Absorption is the primary event that allows a light to cause potentially therapeutic effects on a tissue. Without absorption, there is no energy transfer to the tissue and the tissues are left unaffected by the light. Absorption of light provides a diagnostic role such as the spectroscopy of a tissue. Absorption can provide a clue as to the chemical composition of a tissue, and serve as a mechanism of optical constant during imaging. Absorption is used for both spectroscopic and imaging applications.

There are two major types of chromophores: electronic transitions and vibrational transitions. In the wavelength range of 180–800 nm, light is absorbed by many biological molecules via electronic transitions. But, there are also atomic absorptions of a light in the wavelength range. The absorption spectrum depends on the typical of predominant absorption enters and water content of tissues. The field infrared spectroscopy studies the variety of bonds, which can resonantly vibrate or twist in response to infrared wavelengths and thereby absorb such photons. In the infrared wavelength range, the absorption of water is the strongest contributor to tissue absorption.

In this dissertation, a chromophore idealized will be considered as a sphere with a particular geometrical size. And this sphere blocks incident light and casts a shadow, which constitutes absorption. It provides a simple concept, which captures the essence of the absorption coefficient, the parameter I use to describe the effectiveness of absorption. The size of absorption shadow is called the effective cross-section σ_a [cm^2 or mm^2] and can be smaller or larger than the geometrical size of the chromophore A [cm^2 or mm^2], related by the proportionality constant called the absorption efficiency Q_a [dimensionless]:

$$\sigma_a = Q_a A \tag{1.1}$$

The absorption coefficient μ_a [cm^{-1} or mm^{-1}] describes a medium containing many chromophores at a concentration described as a volume density ρ_a [cm^3 or mm^3]. The absorption coefficient is essentially the cross-sectional area per unit volume of medium.

$$\mu_a = \rho_a \sigma_a \tag{1.2}$$

Experimentally, the units [cm^{-1} or mm^{-1}] for μ_a are inverse length, such that the product $\mu_a L$ is dimensionless, where L [cm or mm] is a photon's pathlength of travel through the medium.

1.3.2 Scattering coefficient

Light scattering originates from the interaction of photons with structure heterogeneities present inside materials bodies at the wavelength scale. The interaction between a photon and a molecule results in a photon move into a different direction and a molecule that may maintain, increase, ore decrease its energy. If the energy of the scattered photon is the same as the incident photon, the interaction is noted as inelastic scattering. Rayleigh scattering is an example of elastic scattering, which occurs when light propagates through gases, while Raman scattering is an example of inelastic scattering. None of the inelastic scattering will be covered in this dissertation. The interaction due to scattering is described by the scattering coefficient μ_s and by the scattering phase function $p(\theta)$. θ is the scattering angle. The scattering coefficient μ_s is essentially the cross-sectional are per unit volume of medium.

Elastic light scattering originates from the heterogeneity of refractive index inside the medium[12]. In biomedical optics, scattering of photons is an important event. Scattering provides feedback during therapy. For example, for successful therapy planning and dosimetry in laser-induced interstitial heating of brain tumor[28,29], a database of the optical properties of tumors and of surrounding native during laser coagulation of tissue[30], and the onset of scattering is an observable endpoint that correlates with a desired therapeutic goal. Scattering also strongly affects the dosimetry of light during therapeutic goal. Scattering also strongly affects the dosimetry of light during therapeutic procedures that depend on absorption.

In this dissertation, the scatter is considered as a scattering particle idealized as a sphere with a particular geometrical size. And that this sphere redirects incident photons into new directions and so prevents the forward on-axis transmission of photons, thereby casting a shadow. This process provides a simple concept, which captures the essence of the scattering coefficient, a parameter analogous to absorption coefficient discussed in Section 1.3.1.

The size of the scattering shadow is called the effective cross-section σ_s [cm^2 or mm^2] and can be smaller or larger than the geometrical; size of the scattering particle, related by the proportionality constant called the scattering efficiency Q_s:

$$\sigma_s = Q_s A \tag{1.3}$$

The scattering coefficient μ_s [cm^{-1} or mm^{-1}] describes a medium containing many scattering particles at a concentration described as a volume density ρ_s [cm^{-3} or mm^{-3}]. The scattering coefficient is essentially the cross-sectional area per unit volume of medium.

$$\mu_s = \rho_s \sigma_s \tag{1.4}$$

1.3.3 Phase functions

The scattering phase function $p(\hat{s}, \hat{s}')$ is defined as the probability that a photon traveling in direction $\hat{s}$ is scattered with in the unit solid angle around the direction $\hat{s}'$. The scattering function has the dimensions of sr^{-1}. When, isotropic scatters is considered, the scattering function only depends on the scattering angle, i.e., the angle between directions $\hat{s}$ and $\hat{s}'$. The $p(\hat{s}, \hat{s}') = p(\theta)$. The following normalization for the scattering function is thus assumed:

$$\int_{4\pi} p(\hat{s}, \hat{s}') \mathrm{d}\omega = 2\pi \int_0^{\pi} p(\theta) \sin\theta \, \mathrm{d}\theta = 1 \tag{1.5}$$

where $\mathrm{d}\omega$ is a differential solid angel in the $\hat{s}$ direction.

An isotropic scattering function would scatter light with equal efficiency into all possible directions. Such a scattering function would have the form:

$$p(\theta) = \frac{1}{4\pi} \tag{1.6}$$

When propagation is dominated by multiple scattering, a single number can be sufficient to characterizing function. If the phase function is not isotropic, then a parameter called the average cosine of the phase function is used to describe the degree of anisotropy of the phase function. This parameter is often denoted by g and is defined as the integral over all angles of the phase function multiplied by the cosine of the angle:

$$g = <\cos\theta> = 2\pi \int_0^{\pi} \cos\theta \; p(\theta) \sin\theta \, \mathrm{d}\theta \tag{1.7}$$

The choice of a single scattering phase function is a compromise between realism and mathematical tractability. Henyey-Greenstein devised a useful identity function. The Henyey-Greenstein function allows the anisotropy factor g to specify $p(\theta)$ such that calculation of the

expectation value for $\cos\theta$ returns exactly the same value g. The Henyey-Greenstein function is:

$$p(\theta) = \frac{1}{4\pi} \frac{1-g^2}{\left(1+g^2-2g\cos\theta\right)^{3/2}} \tag{1.8}$$

1.3.4 Reduced scattering coefficient

For a non-absorbing turbid medium in which the interaction of light can be described with the scattering coefficient and the scattering function, the propagation of photons can be represented as a random walk in which they frequently change direction due to scattering. With reference to photons emitted in an infinite non-absorbing homogenous medium at $z = 0$ along the z-axis, if I indicate with (x_k, y_k, z_k) the coordinates of the point in which the k^{th} scattering event occurs, it has been shown[31] that

$$< x_k >=< y_k >= 0, < z_k >= \frac{1}{\mu_s} \sum_{i=0}^{k-1} g^i = \frac{1}{\mu_s} \frac{1-g^k}{1-g} \tag{1.9}$$

and the mean value of the square distance from the source after k scattering events becomes

$$< d_k^2 >=< x_k^2 + y_k^2 + z_k^2 >= \frac{2}{\mu_s^2} \frac{k-(k+1)g+g^{k+1}}{(1-g)^2} \tag{1.10}$$

Since $-1 \leq g \leq 1$, for large values of k the mean value of z_k reaches the value

$$\lim_{k\to\infty} < z_k >= \frac{1}{\mu_s} \frac{1}{1-g} = \frac{1}{\mu_s'} \tag{1.11}$$

and $<d_k^2>$ becomes

$$< d_k^2 >\cong \frac{2}{\mu_s^2} \frac{k(1-g)}{(1-g)^2} = \frac{2}{\mu_s'^2} k(1-g), \tag{1.12}$$

where

$$\mu_s' = \mu_s(1-g) \tag{1.13}$$

is the reduced scattering or transport coefficient of the medium. The quantity

$$l' = \frac{1}{\mu_s'} \tag{1.14}$$

is the transport mean free path. Equation (1.11) shows that for a homogenous non-absorbing medium the transport mean free path represents the mean distance traveled by along the

initial direction of propagation before they have effectively "forgotten" their original direction of motion.

1.3.5 Radiative transfer equation and diffusion equation

Most of the recent advances, the transfer of laser energy in tissue are based upon transport theory. This theory is preferred in tissue optics instead of analytic approaches using Maxwell equations because of inhomogeneity of biological tissue. According to transport theory, the radiance $L(\vec{r}, \hat{s}, t)$ [W/m^2 sr Hz or W/cm^2 sr Hz] of light at position $\vec{r}$ traveling in a direction of the unit vector $\hat{s}$ is decreased by absorption and scattering but it is increased by light that is scattered from $\hat{s}'$ directions into the direction s. The radiative transport equation which describes this light interaction is[32]

$$\frac{\partial}{c_m \partial t} L(\vec{r}, \hat{s}, t) + \hat{s} \cdot \nabla L(\vec{r}, \hat{s}, t) + (\mu_a + \mu_s) L(\vec{r}, \hat{s}, t) = \mu_s \int_{4\pi} p(\hat{s}, \hat{s}') L(\vec{r}, \hat{s}') d\omega' + \varepsilon(\vec{r}, \hat{s}, t) \tag{1.15}$$

where $d\omega'$ is the differential solid angle in the direction s', $p(s, s')$ is the phase function, c_m is the speed of light inside the medium, and ε is the source term that is the power emitted at the time t per unit volume.

The several numerical methods used to treat the radiative transfer equation are a consequence of the high complexity of this equation. No general analytical (closed-form) solutions of the radiative transfer equation are available, and simpler approximate models are usually sought. When propagation is dominated by multiple scattering, the most widely and successfully used model employs the diffusion approximation to yield a variety of solutions for both steady state and time dependent sources. The diffusion equation is a parabolic type partial differential equation largely applied in several physics fields.

In more general case of time-dependent sources, the diffusion approximation consists of two simplifying assumptions. The first one assumes the radiance inside a diffusive medium to be almost isotropic. The diffuse intensity $L(\vec{r}, \hat{s}, t)$ is approximated by the first two terms (isotropic and linearly anisotropic terms) of a series expansion in spherical harmonics:

$$L(\vec{r}, \hat{s}, t) = \frac{1}{4\pi} F(\vec{r}, t) + \frac{3}{4\pi} J(\vec{r}, t) \cdot \hat{s} \tag{1.16}$$

A spherical harmonic expansion truncated at the second term is usually denoted as the P_1 approximation. Equation (1.16) is a good approximation for the radiance if the

contribution of the higher-order spherical harmonics is negligible. This is usually true if the second term of the expansion is small with respect to the first, i.e., $F(\vec{r}\,,\,t) >> 3\vec{J}(\vec{r},t)\cdot\hat{s}$. Fluence rate $F(\vec{r}\,,\,t)$ [W/m^2 or W/cm^2] is obtained integrating the radiance over the entire solid angle

$$F(\vec{r},t) = \int_{4\pi} L(\vec{r},\hat{s},t)\,\mathrm{d}\omega \tag{1.17}$$

Another quantity useful in describing propagation is the flux vector [W/m^2 or W/cm^2], defined as

$$\vec{J}(\vec{r},t) = \int_{4\pi} L(\vec{r},\hat{s},t)\hat{s}\,\mathrm{d}\omega \tag{1.18}$$

which represents the amount and the direction of the net flux of power.

The second simplifying assumption assumes that the time variation of the diffuse flux vector $\vec{J}(\vec{r},t)$ over a time range $\Delta t = 1/c_{\mathrm{m}}\mu_{\mathrm{s}}'$ is negligible with respect to the vector itself and can be expressed as

$$\frac{1}{c_{\mathrm{m}}\mu_{\mathrm{s}}'}\left|\frac{\partial\vec{J}(\vec{r},t)}{\partial t}\right| << \left|\vec{J}(\vec{r},t)\right| \tag{1.19}$$

With equation (1.19), "slow" time variations of the flux are therefore assumed.

When steady-state sources are considered, the diffusion approximation is simply summarized by the expansion of the radiance in spherical harmonics, i.e.,

$$L(\vec{r},\hat{s}) = \frac{1}{4\pi}F(\vec{r}) + \frac{3}{4\pi}\vec{J}(\vec{r})\cdot\hat{s} \tag{1.20}$$

In general, equation (1.16), (1.19), and (1.20) are well fulfilled when photons have undergone many scattering events, since scattering tends to randomize the direction of light propagation. Conversely, absorption obstructs the diffusive regime.

The radiative transfer equation is an integro-differential equation for the radiance, while the diffusion equation is a partial-differential equation for the fluence rate. Thus, an integration procedure is required to obtain the diffusion equation from the radiative transfer equation.

In order to obtain the diffusion equation for time-dependent sources, equation (1.15) is integrated over all directions as follows:

$$\int_{4\pi}\left\{\frac{\partial}{c_m\partial t}L(\vec{r},\hat{s},t)+\nabla\cdot[\hat{s}L(\vec{r},\hat{s},t)]+(\mu_a+\mu_s)L(\vec{r},\hat{s},t)\right\}d\omega$$
$$=\int_{4\pi}[\mu_s\int_{4\pi}p(\hat{s},\hat{s}')L(\vec{r},\hat{s},t)d\omega'+\varepsilon(\vec{r},\hat{s},t)]\,d\omega \qquad (1.21)$$

From this equation, simply exchanging the order of derivatives and integrals and the orders of integration, the continuity equation is obtained without any need for simplifying assumptions:

$$\frac{\partial}{c_m\partial t}F(\vec{r},t)+\nabla\cdot\vec{J}(\vec{r},t)+\mu_a F(\vec{r},t)=\int_{4\pi}\varepsilon(\vec{r},\hat{s},t)\,d\omega \qquad (1.22)$$

To obtain the diffusion equation, the flux vector needs to be expressed as a function of the fluence rate. For this purpose, the radiative transfer equation (1.15) is multiplied by $\hat{s}$ and then integrated over all the directions as follows:

$$\int_{4\pi}\left\{\frac{\partial}{c_m\partial t}L(\vec{r},\hat{s},t)+\nabla\cdot[\hat{s}L(\vec{r},\hat{s},t)]+(\mu_a+\mu_s)L(\vec{r},\hat{s},t)\right\}\hat{s}\,d\omega$$
$$=\int_{4\pi}[\mu_s\int_{4\pi}p(\hat{s},\hat{s}')L(\vec{r},\hat{s},t)d\omega'+\varepsilon(\vec{r},\hat{s},t)]\,\hat{s}\,d\omega \qquad (1.23)$$

From equation (1.21), making use of the simplifying assumptions of the diffusion approximation, equation (1.16) and (1.19), Fick's law is obtained:

$$\vec{J}(\vec{r},t)=-D[\nabla F(\vec{r},t)-3\int_{4\pi}\varepsilon(\vec{r},\hat{s},t)\,\hat{s}\,d\omega] \qquad (1.24)$$

where D is the diffusion coefficient defined as

$$D=\frac{1}{3(\mu_a+\mu_s')} \qquad (1.25)$$

For media without sources or with isotropic sources, Fick's law becomes $\vec{J}(\vec{r},t)=-D\nabla F(\vec{r},t)$, which is the usual form used to represent the flux inside diffusive media.

Green's functions of the diffusion equation for other homogenous geometries like the finite cylinder are available. The solutions of the diffusion equation are approximate solutions of the radiative transfer equation. Let us consider an infinite homogenous medium characterized by μ_a, μ_s', and diffusion coefficient $D=1/(3\mu_s')$. Given a spatial and temporal isotropic Dirac delta sources of unitary strength is the origin

$$q_0(\vec{r},t)=\eta^3(\vec{r})\eta(t) \qquad (1.26)$$

where q_0 is source term of the diffusion equation. The diffusion equation for the fluence rate can be written as

$$(\frac{\partial}{c_m \partial t} - D\nabla^2 + \mu_a)F(\vec{r},t) = q_0(\vec{r},t) \tag{1.27}$$

The time-dependent Green's function for $t > 0$ is

$$F(\vec{r},t) = \frac{c_m}{(4\pi D c_m t)^{3/2}} \exp(-\frac{r^2}{4Dc_m t} - \mu_a c_m t) \tag{1.28}$$

with $r = |\vec{r}|$ as the distance from the source. Through the use of Fick's law (equation 1.24), the time-dependent Green's function for the flux for any $t > 0$ results in

$$\vec{J}(\vec{r},t) = \frac{r}{16(\pi D c_m)^{3/2} t^{5/2}} \exp(-\frac{r^2}{4Dc_m t} - \mu_a c_m t)\,\hat{r} \tag{1.29}$$

and the Green's functions for the radiance, using equation (1.16), (1.28), and (1.29), can be written as

$$L(\vec{r},\hat{s},t) = \frac{1}{(4\pi)^{5/2}(Dc_m t)^{3/2}} \exp(-\frac{r^2}{4Dc_m t} - \mu_a c_m t) \tag{1.30}$$

Integrating equations (1.28), (1.29), and (1.30) over the whole time range, the following expressions for the Green's functions for steady-state sources $F(\vec{r})$, $\vec{J}(\vec{r})$, and $L(\vec{r},\hat{s})$ are obtained:

$$F(\vec{r}) = \frac{1}{4\pi r D} \exp(-\mu_{eff} r) \tag{1.31}$$

$$\vec{J}(\vec{r}) = \frac{1}{4\pi r}(\frac{1}{r} + \mu_{eff}) \exp(-\mu_{eff} r)\hat{r} \tag{1.32}$$

$$L(\vec{r},\hat{s}) = \frac{1}{16\pi^2 r D}[1 + 3(\frac{D}{r} + \mu_{eff} D)(\hat{r}\cdot\hat{s})] \exp(-\mu_{eff} r) \tag{1.33}$$

where

$$\mu_{eff} = \sqrt{\mu_a / D} = \sqrt{3\mu_a \mu_s'} = 1/\delta \tag{1.34}$$

is the effective attenuation coefficient. δ is the optical penetration depth, which is determined by the distance over which the diffuse energy fluence rate drops to $1/e$ of its initial value.

It is important to stress that the analytical expression for the continuous wave flux, equation (1.32), is the exact solution of the radiative transfer equation for the case of a non-absorbing medium.

1.4 Optical properties of biological materials

Optical properties of biological tissues are vital to dosimetry studies. There are several major contributions to the absorption spectrum. In the infrared, the absorption increases with longer wavelengths due to tissue water content. In figure 1.2, scaling the pure water absorption by 75% mimics a typical tissue with 75% water content[33]. Whole blood is a strong absorber in the red-NIR wavelength range. Local absorption properties govern light-tissue interactions, and average absorption properties govern light transport[34]. Melanosomes are also strong absorbers. As shown in figure 1.2, the local interaction of light with the melanosomes is strong, but the melanosome contribution to the average absorption coefficient may modestly affect light transport[35]. As shown in figure 1.2, many laser surgeries utilize the light in the visible and NIR wavelength region. The optical properties in the wide wavelength range are important in laser medicine.

The optical properties of tissue samples are measured by different methods. *In vitro* evaluation is most often achieved[36,37]. However there are a few reports on the optical properties in the wide wavelength range.

The changes of the optical properties by laser treatments are particularly interesting[37,38]. The light propagations change by the kinetic changes of the optical properties during laser irradiation. This problem is clinically very important for the realization of optimal laser treatment because the understandings of the change of optical properties by several laser parameters can realize the pre-estimated treatment effects. However, to my knowledge, there are no experimental studies about alternation of the tissues considered from the aspect of the optical properties after many treatments (laser coagulation therapy, PDT, etc.).

1.6 Goals

The primary goal of this dissertation is to propose that the optimal laser irradiation parameters that can achieve optimal treatment results and fewer side effects. This goal has two separate but related tasks:

1. Development of methods to measure the optical properties of a tissue.
2. Determination of the optical properties of the biological tissue and of the optical properties change after laser treatment.

The first task is dealt with in the Chapter 2 according to the methods of solution. There are

- Development of an optical properties measurement system by combining a double integrating sphere apparatus and an inverse MC technique.

- Validation of the optical properties measurement system with a biological tissue phantom.

The double integrating sphere can measure optical parameter quickly, due to the apparatus can measure the R_d and T_t of the sample simultaneously. The MC method is very accurate way, due to the method is can calculate light propagation with index mismatching and anisotropic scattering. Consequently, the optical properties measurement system can measure the optical properties conveniently and accurately.

In Chapter 3 the optical properties of the tissue after laser coagulation are discussed. After the tissue coagulation, the optical properties changed. For more effective treatment in laser coagulation therapy, the setting of the irradiation parameter, which considering the optical properties change is presented.

In Chapter 4 the optical properties of the tumor tissue and its change after PDT are discussed. For more effective PDT, the optical properties change after PDT is needed to know.

In Chapter 5 the optical properties of the Japanese skin tissue are discussed. The Japanese skin tissue optical properties in wide wavelength range are needed in dermatology and plastic surgery. However, the Japanese skin tissue optical properties are rare. The optical properties were measured and the thermal effect was simulated with MC method to estimate the safety in laser therapy.

References

1. M. E. Brezinski, Optical coherence tomography: principles and applications, Academic Press, Boston, MA, 2006.
2. B. Selkin, M. Rajadhyaksha, S. Gonzalez, R. G. Langley, In vivo confocal microscopy in dermatology, *Dermatol. Clin.*, 19(2), 369–377, 2001.
3. L. T. Perelman, Optical diagnostic technology based on light scattering spectroscopy for early cancer detection, *Expert Rev. Med. Devices*, 3(6), 787–803, 2006.
4. N. S. Trivedi, A. F. Ghouri, N. K. Shah, E. Lai, and S. J. Barker, Effects of motion, ambient light, and hypoperfusion on pulse oximeter function, *J. Clin. Anesth.*, 9, 179–183, 1997.
5. S. van de Ven, S. Elias, A. Wiethoff, M. van der Voort, A. Leproux, T. Nielsen, B. Brendel, L. Bakker, M. van der Mark, W. Mali, and P. Luijten,. Diffuse optical tomography of the breast: initial validation in benign cysts, *Mol. Imaging Biol.*, 11, 64-70, 2009.

6. L. V. Wang, Photoacoustic imaging and spectroscopy, CRC Press, Boca Raton, FL, 2009.
7. S. Schmitz-Valckenberg, F. G. Holz, A. C. Bird, and R. F. Spaide, Fundus autofluorescence imaging: review and perspectives, *Retina*, 28, 385-409, 2008.
8. R. D. Goldman and D. L. Spector, Live cell imaging: a laboratory manual. Cold Spring Harbor Laboratory Press: Cold Spring Harbor, NY, 2005.
9. E. Smith and G. Dent, Modern Raman spectroscopy: a practical approach. J. Wiley: Hoboken, NJ, 2005.
10. Y. Tamura, T. Kuroiwa, Y. Kajimoto, Y. Miki, S. Miyatake, M. Tsuji, Endoscopic identification and biopsy sampling of an intraventricular malignant glioma using a 5-aminolevulinic acid-induced protoporphyrin IX fluorescence imaging system. Technical note, *J. Neurosurg.*, 106(3), 507–510, 2007.
11. A. P. Castano, T. N. Demidova, and M. R. Hamblin, Mechanisms in photodynamic therapy: part three-photosensitizer pharmacokinetics, biodistribution, tumor localization and modes of tumor destruction., *Photodiagnosis Photodyn. Ther.*, 2(2), 91–106, 2005.
12. C. T. Germer, C. Isbert, D. Albrecht, A. Roggan, J. Pelz, J. P. Ritz, G. Müller, H. J. Buhr, Laser-induced thermotherapy combined with hepatic arterial embolization in the treatment of liver tumors in a rat tumor model, *Ann. Surg.*, 230(1): 55–62, 1999.
13. L. Dzieciuchowicz, Z. Krasiński, L. Kruszyna, G. Espinosa, Assessment of the level of difficulty of four techniques of endovenous thermal ablation of the great saphenous vein and the echogenicity of the tip of the working device in vivo, *Ann Surg.* 230(1), 55, 1999.
14. J. Akimoto, J. Haraoka, and K. Aizawa, Preliminary clinical report on safety and efficacy of photodynamic therapy using talaporfin sodium for malignant gliomas, *Photodiagnosis Photodyn. Ther.*, 9(2): 91–99, 2012.
15. K. Awazu Supervisor, Novel photo therapy-mediation of laser technique to clinical, CMC Publishing, 2010.
16. 光凝固の一般的注意： 27–32，清水弘一，野寄喜美春，レーザー光凝固，医学書院，1982.
17. N. Krasner, Palliative laser therapy for tumors of the gastrointestinal tract, *Bailliere. Clin. Gastr.*, 5: 37–57, 1991.
18. J. H. Hubbell, Photon mass attenuation and energy-absorption coefficients from 1 keV to 20 MeV, *Int. J. Appl. Radiat. Isot.*, 33: 1269–1290, 1982.
19. M. F. Hawthorne, K. Shelly, R. J. Wiersema, (Eds.): Frontiers in neutron capture therapy, Springer, 2001.

20. W. Cheong, S. A. Prahl, and A. J. Welch, A review of the optical properties of biological tissues - Quantum Electronics, IEEE Journal of. IEEE Journal of Quantum Electronics, 26(12), 1–20, 1990.
21. D. W. Ebert, C. Roberts, S. K. Farrar, W. M. Johnston, A. S. Litsky, and A. L. Bertone, Articular Cartilage Optical Properties in the Spectral Range 300-850 nm, *J. Biomed. Opt.* 3, 326–333, 1998.
22. S. A. Prahl, Light Transport in Tissue, *PhD thesis*, University of Texas at Austin, 1988.
23. D. D. Royston, R. S. Poston, and S. A. Prahl, Optical properties of scattering and absorbing materials used in the development of optical phantoms at 1064 nm, *J. Biomedical Optics*, 1, 110–116, 1996.
24. H. Karlsson, I. Fredriksson, M. Larsson, and T. Stromberg, Inverse Monte Carlo for estimation of scattering and absorption in liquid optical phantoms, *Optical express*, 20(11), 12233–13346, 2012.
25. C. R. Simpson, M. Kohl, M. Essenpreis, and M. Cope, Near-infrared optical properties of *ex vivo* human skin and subcutaneous tissues measured using the Monte Carlo inversion technique, *Phys. Med. Biol.*, 43, 2465–2478, 1998.
26. A. N. Yaroslavsky, I. V. Yaroslavsky, T. Goldbach, and H.-J. Schwarzmaier, Influence of the scattering phase function approximation on the optical properties of blood determined from the integrating sphere measurements, *J. Biomed. Opt.* 4(1), 47–53, 1999.
27. V. V. Tuchin, Methods and algorithms for the measurement of the optical parameters of tissues, 143-256, Tissue Optics: light scattering methods and instruments for medical diagnosis, 2nd ed., SPIE Press, 2007.
28. Z. Amin, J. J. Donald, A. Masters, R. Kant, A. C. Steger, S. G. Brown, and W. R. Lees, Hepatic metastasis: interstitial laser photocoagulation with real-time US monitoring and dynamic CT evaluation of treatment *Radiology*, 187, 339–347, 1993.
29. T. Kahn, M. Bettag, and F. Ulrich, MRI-guided laser-induced interstitial thermotherapy of cerebral neoplasms, *J. Comput. Assist. Tomogr.*, 18, 519–32, 1994.
30. A. N. Yaroslavsky, P. C. Schulze, I. V. Yaroslavsky, R. Schober, F. Ulrich, and H.-J. Schwarzmaier, Optical properties of selected native and coagulated human brain tissues in vitro in the visible and near infrared spectral range, *Phys. Med. Biol.*, 47, 2059–2073, 2002.
31. G. Zaccanti, E. Battistelli, P. Bruscaglioni, and Q. N. Wei, Analytic relationships for the statistical moments of scattering point coordinates for photon migration in a scattering medium, *Pure Appl. Opt.*, 3. 897–905, 1994.

32. F. Martelli, S. D. Bianco, A. Ismaelli, and G. Zaccanti (eds.), Solutions of the diffusion equation for homogenous media, in: Light Propagation through Biological Tissue and other Diffusive Media. Washington: SPIE Press, 2010.
33. G. M. Hale, M. R. Querry, Optical constants of water in the 200 nm to 200 μm wavelength region, *Appl. Opt.*, 12, 555–563, 1973.
34. Oregon Medical Laser Center at Providence St. Vincent Medical Center: http://omlc.ogi.edu/spectra/hemoglobin/index.html.
35. Oregon Medical Laser Center at Providence St. Vincent Medical Center: http://omlc.ogi.edu/spectra/melanin/index.html.
36. S. C. Gebhart, W. C. Lin, and A. Mahadevan-Jansen, In vitro determination of normal and neoplastic human brain tissue optical properties using Inverse Adding-Doubling, *Phys. Med. Biol.*, 51, 2011–2027, 2006.
37. A. N. Bashkatov, E. A. Genina, V I. Kochubey, and V. V. Tuchin, Optical properties of human skin, subcutaneous and mucous tissues in the wavelength range from 400 to 2000 nm, *J. Phys. D: Appl. Phys.*, 38, 2543–2555, 2005.
38. J. P. Ritz, A. Roggan, C. Isbert, G. Müller, H. J. Buhr, and C. T. Germer, Optical properties of native and coagulated porcine liver tissue between 400 and 2400 nm, *Lasers Surg. Med.*, 29, 205–212, 2001.

Figures

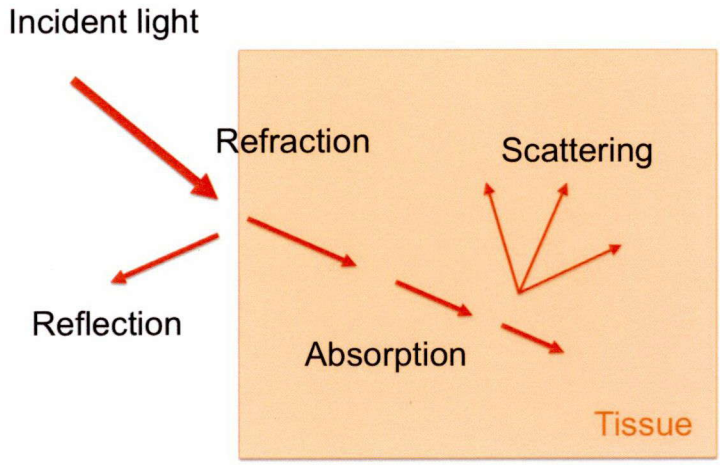

Figure 1.1 Physical phenomena induced by the interaction between light and biological tissue.

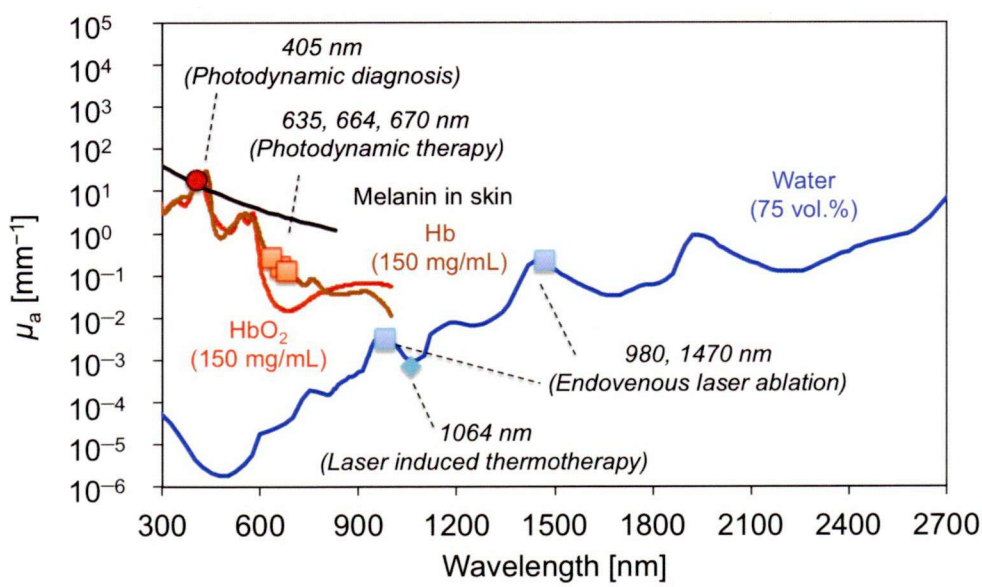

Figure 1.2 Absorption coefficient μ_a spectra for the chromophores in tissue.

Chapter 2
Optical Properties Measurement System

2.1 Introduction

Numerous instances have been presented using the integrating sphere as a tool to measure the total diffuse reflection and transmission of optically turbid and homogenous materials, including several biological tissues[1–4] since it was first described by Ulibricht[5] in 1900. MC models of light transport have been used with integrating sphere measurements to determine optical properties[6–11], an optimization routine finds the absorption and scattering coefficients by iteratively calculation the reflectance and transmittance.

The optical properties of a tissue are well known, however, there are a few reports on the optical properties in the wide wavelength range, and the dynamic of optical properties during or after a laser irradiation or a laser treatment.

The purpose of this work is to develop the accurate optical properties measurements system by using double integrating sphere and inverse MC techniques in the wavelength range of 350–2100 nm. An optical system of integrating sphere measurements is presented. And, tissue phantoms are utilized for the calibration of the optical properties measurement system.

2.2 Materials and Methods

The aim is to provide two methods using integrating spheres to indirectly determine the optical properties of a material and show that the process is accurate and consistent under a wide variety of experimental conditions.

2.2.1 Test samples

To show that my experimental method is robust, a sample is required that is simple, stable and whose absorption properties are known by independent means from the method presented here.

This chapter was originally published under the title, "Development of the tissue optical properties measurement system with double integrating sphere and inverse Monte Carlo techniques in the visible and near-infrared wavelength range" by N. Honda, K. Ishii, T. Nanjo and K. Awazu in Journal of Japan Society for Laser Surgery and Medicine, vol. 32, no. 4, 421, 2012.

For the estimation of a precision of the double integrating sphere optics, the phantom containing of 0.01, 0.02 and 0.04 mL/mL of aqueous suspensions of lipid droplets (Intralipid 20%, Terumo, Japan), 1.00×10^2 mg/mL gelatin powder (G2500-500G, Sigma-Aldrich, Japan), and solution of the hemoglobin (H7379-10G, Sigma-Aldrich) of 1.00 mg/mL was prepared. The sample was sandwiched with slide glasses. The sample thickness was 1.0 mm.

To validate the accuracy of the absorption coefficient measurement by using the optical measurement system, the phantom containing of 0.04 mL/mL of aqueous suspensions of lipid droplets (Intralipid 20%, Terumo, Japan) and 1.00×10^2 mg/mL gelatin powder (G2500-500G, Sigma-Aldrich, Japan) was prepared. This dilution contained exactly the same amount of scattering compounds as in the hemoglobin dilutions described below. Solution of the hemoglobin was prepared with concentration of 2.00, 1.00, 0.50, and 0.25 mg/mL. The sample was sandwiched with slide glasses. The sample thickness was 1.0 mm.

To validate the expected theoretical value of the absorption coefficient μ_a, spectrometer measurements were performed for hemoglobin diluted with water. Before mixing the hemoglobin phantoms, the hemoglobin dilution with water was prepared to determine the absorption coefficient of hemoglobin. The absorption coefficients as a function of hemoglobin concentration were measured in water. A solution of hemoglobin suspended in water was prepared at a concentration of 0.40, 0.20, 0.10, 0.05, and 0.03 mg/mL. The absorption coefficients μ_a for hemoglobin was estimated with a statement of Beer's Law of transmission.

$$\mu_a = -\frac{1}{L_m}\ln T \qquad (2.1)$$

where L_m [cm or mm] is a photon's path length of travel through the medium. The hemoglobin dilution was transferred to 10 mm path length cuvette placed in front of transmittance measurement system. Xenon lamp was used as a light source. Accounting for the beam diameter on the cuvette was 1 mm. The transmittance signal was sampled for 100 ms with a spectrometer (Maya2000 Pro, Ocean Optics, USA) through an optical fiber (CUSTOM-PATCH-2243142, Ocean Optics, USA).

Monodisperse latex microspheres suspensions (S37491, Invitrogen, USA) in water were used to validate the optical properties obtained from the double integrating sphere optics and the inverse MC technique. In this study, the optical properties of 0.01 g/L of monodisperse latex microspheres suspension in water were measured. Before measurement, the suspensions was mixed with the 1.00×10^2 mg/mL gelatin powder. The sample was sandwiched with slide glasses. Sample thickness was 1.0 mm.

To validate the expected theoretical value of the reduced scattering coefficients μ_s', the reduced scattering coefficients μ_s' was determined from the volume fraction of microsphere ϕ_m, the values for scattering efficiency Q_{scat} and the anisotropy coefficient g are calculated from the microsphere radius r, and the refractive indices of latex microspheres and water using Mie theory[12] program provided by Prahl at the Laser Research Center at St. Vincent Hospital, Portland Oregon[13]. In the calculation, the microsphere radius r was assumed as 200 nm. And, the refractive indices of polystyrene[14,15] which composed in latex beads and water[16] in the wavelength range of 350–1000 nm were assumed as 1.57–1.61 and 1.327–1.337, respectively (Table 2.2). The refractive indices of the polystyrene are assumed by applying a modified Cauchy' approximation in the form:

$$n^2(\lambda) = A_1 + A_2\lambda^2 + \frac{A_3}{\lambda^2} + \frac{A_4}{\lambda^4} + \frac{A_5}{\lambda^6} + \frac{A_6}{\lambda^8} \qquad (2.2)$$

where A_1, A_2, A_3, A_4, A_5, and A_6 are the calculated dispersion coefficients and λ is the wavelength expressed in microns. The dispersion coefficients from A_1 to A_6 for polystyrene were 2.610025, -6.143673×10^{-2}, -1.312267×10^{-1}, 6.865432×10^{-2}, -1.295968×10^{-2}, and 9.055861×10^{-4}, respectively.

The contributions of the Mie and Rayleigh scattering to the reduced scattering coefficients are reported[17]. An additional to the Mie scattering, the Rayleigh scattering is considered to estimate the expected theoretical value of the reduced scattering coefficients μ_s'. The Rayleigh scattering can be represented as[18]:

$$\mu_s' = b\lambda^{-4} \qquad (2.3)$$

where the factor b varied only with the magnitude of Rayleigh scattering and λ is in nanometers.

The measured reduced scattering coefficient spectrum, which is a combination of the Mie and Rayleigh scattering spectra, has been fitted by:

$$\mu_s'(\text{measured}) = \mu_s'(\text{Mie}) + \mu_s'(\text{Rayleigh}) \qquad (2.4)$$

An aqueous solution of lipid droplets is a fat emulsion that is typically used as a tissue phantom in the therapeutic window (600–1000 nm) since it has optical properties similar to tissue when its concentration is diluted to 0.5% fat by volume[19, 20]. The aqueous solution of lipid droplets was investigated within the wavelength range of 350–2100 nm as the sample of biological tissue phantom in order to evaluate the specific of the optical properties measurement system.

Three scattering phantoms, containing various proportions of 0.01, 0.02, and 0.04 mL/mL aqueous suspensions of lipid droplets, water, 1 mg/mL hemoglobin and 1.00×10^2 mg/mL gelatin were prepared for the measurement of optical properties over the wavelength region of 350 to 2100 nm. The sample thickness was 0.2 mm.

2.2.2 Double integrating sphere optics

Double integrating sphere experiments were performed as diagrammed in figure 2.1. The double integrating sphere systems was employed to measure the R_d and T_t. The sample was placed between two integrating spheres (CSTM-3P-GPS-033-SL, Labsphere, USA), which are coated with a diffusely reflective material suitable for this wavelength region. The entrance port size was 10.0 mm in diameter. Table 2.1 shows a light source and detector employed in this study. The sample illumination between 350 and 2100 nm is achieved using a xenon light source and a 150 W halogen light source. The reflected and transmission light were multiply scattered in spheres and recorded by spectrophotometer as R_d and T_t, respectively. The detector was cooled by peltier units (PS-50W, Takagi MFG, Co., LTD, Japan).

The fraction of light scattered from the sample collected by the integrating sphere was calculated as follows. The sample thickness was varied from 0.1 to 1.5 mm. The slide glass thickness is assumed as 1.0 mm. Refractive indices of the sample and slide glass are assumed as 1.33 and 1.38, and 1.524, respectively. The sample port diameter was assumes as 10.0 mm. The maximum solid angles of acceptance for the integrating sphere are shown in figure 2.2.

For all experiments, the reference was a 99% Spectralon reflection standard (Labsphere, Inc., USA) for reflection or an open port as the reference in transmission. The optical properties were determined from the measured reflectance and transmittance using an inverse MC program.

The signal to noise ration of the single beam of the double integration sphere optics were estimated in the following format:

$$\text{S/N ratio} = 10 \times \log_{10}\left\{\frac{\text{Average}\,(\lambda)}{\text{Maximum value}\,(\lambda) - \text{Minimum value}\,(\lambda)}\right\} \tag{2.5}$$

The precision of the measurement of the R_d and T_t were estimated by using of the phantom containing the aqueous solution of lipid drops varied with 0.01, 0.20, and 0.04 mL/mL, 1.00×10^2 mg/mL gelatin, and 1.0 mg/mL hemoglobin in the wavelength range of 350–2100 nm.

2.2.3 Inverse Monte Carlo technique

The inverse Monte Carlo technique was employed to calculate the optical properties of samples from measured value of R_d and T_t. A Monte Carlo simulations used in this study was developed by Wang *et al.* (ref. 21). In this study, the Monte Carlo code was included simplifying assumptions to take into account the exact geometrical configuration of port diameter of the integrating sphere (See Appendix A). This technique is an iterative process, which estimates the reflectance and transmittance from a set of optical parameters until the calculated reflectance and transmittance match the measured values. With this iterative process the set of optical properties that yields the closest match to the measured values of reflectance and transmittance are taken as optical properties of the tissue as shown in figure 2.3. This method allows one to determine the μ_a and μ_s of a tissue from the measured values.

In this study the anisotropy factor g was assumed as 0.9. Flock *et al.* have been reported that the anisotropy factor g of 0.1 mL/mL of aqueous suspensions of lipid droplets Intralipid can be presented as[22]

$$g = 2.25\lambda^{-0.155} \tag{2.6}$$

2.3 Results and Discussion

2.3.1 Measurement stability of double integrating sphere optics

To evaluate the stability of the double integrating sphere optics, the signal to noise ratio of the single beam and the reproducibility of the R_d and T_t of the sample were measured. Figure 2.4 shows the signal to noise ratio spectra in the wavelength range of 350–2100 nm. The minimum of the signal to noise ratio was over 20 dB. Figure 2.5(a) and (b) show the R_d and T_t spectra of the phantom varied with the aqueous solution of lipid drops 0.01, 0.20, and 0.04 mL/mL in the wavelength range of 350–2100 nm. The vertical lines show the maximum values and the minimum values of the measurement of five times. The maximum difference between the measured values and the average value in the wavelength range of 350–1000 nm and 1000–2100 nm were 1.2% and 1.7%, respectively. Then, the measurement stability of R_d and T_t is very high.

The dispersion of the R_d and T_t of the biological tissue has about a few percent, because the biological tissue is a turbid matter. Then, the measurement error of the R_d and T_t is needed to be less than 5%. In this study the maximum error of the R_d and T_t was 1.7%. The error of the single beam is needed to be less than 1%, results in the signal to noise ratio is

better to be higher than 23 dB. The signal to noise ratio spectra in the wavelength range of 2075–2100 nm were less than 23 dB, however, its were higher than 20 dB, which is necessary and sufficient to the measurement of the biological tissues (figure 2.4). Then, the double integrating sphere optics has high precision for the R_d and T_t measurement.

2.3.2 Absorption characterization

The absorption coefficients spectra as a function of hemoglobin concentration in aqueous suspension of lipid droplets and gelatin in the wavelength range of 350–700 nm are shown in figure 2.6. As shown in figure 2.6, absorption peak around 400 nm appeared in the spectra. The absorption coefficient at 403 nm relates only to the concentration of hemoglobin (C_{Hb}) by the relation:

$$\mu_a^{403} = a_1 C_{Hb} + \mu_{a0}^{403} \tag{2.7}$$

where a_1 = 1.1652 cm^{-1} mL/mg and μ_{a0}^{403} = 0.0004 mm^{-1} is the absorption coefficient for hemoglobin at the wavelength of 403 nm of the hemoglobin in aqueous suspension of lipid droplets and gelatin. The liner relations for the absorption coefficient are applicable for hemoglobin up to a concentration of at least 2.0 mg/mL (figure 2.7). The liner relations for the absorption coefficient of hemoglobin in solution measured by spectrometer are applicable for hemoglobin up to a concentration of at least 0.4 mg/mL. A comparison of the absorption from hemoglobin in solution measured by spectrometer and from the hemoglobin in aqueous suspension of lipid droplets and gelatin measured by the optical properties measurement system is shown in figure 2.7. A linear fit shows a strong correlation between the two methods of absorption coefficient measurement. The wavelength dependence of correlation between the hemoglobin concentration and absorption coefficient in the wavelength range 350–450 nm and 500–1000 nm as shown in 2.8 and 2.9, respectively. In the wavelength range from 350 to 600 nm, the absorption coefficient increases as the sample hemoglobin concentration increases. Results the absorption coefficient spectra in the wavelength range from 350 to 600 nm were correlated with hemoglobin concentration. This result indicates that the optical properties measurement system is able to measure the absorption coefficient of absorber in a turbid media within the concentration range of 0.33–2.33 mm^{-1} accurately.

2.3.3 Scatterer characterization

Figure 2.10 shows the typical agreement between theory and experimental measurements for the reduced scattering coefficient μ_s'. The factor b has been estimated from the fitting as 5.74

$\times 10^5$. The maximum relative error was 14.89% at 425 nm. The reduced scattering coefficient μ_s' at 425 nm was 7.21 mm^{-1} and 8.47 mm^{-1} for the experimental value and theoretical value, respectively.

2.3.4 Optical properties of phantom

The samples were measured in the spectral range of 350–2100 nm. As shown in figure 2.11(a), absorption peaks at 408, 963, 1189, 1447, and 1920 nm appeared in the spectra. The peak at 408 nm corresponded to the absorption of the hemoglobin[23]. The absorbance bands are observed at 963 nm corresponded to the absorption of the water, because of the second harmonics of the fundamental O-H stretching vibration[24]. The absorption peak at 1189 nm is the second overtone of the C-H stretching vibration in fatty acids. Water and lipid absorption bands overlap around 1200 nm[11]. It is well known that the bands near 1400 and 1900 nm can be attributed to free water. The absorption peak at 1447 nm is the overtones of O-H stretching. The band near 1920 nm represents the unique H-O-H bending and O-H stretching combination of molecular free water[24]. These results indicate that the optical properties measurement system can measure the absorption coefficient of the biological tissues.

Figure 2.11(b) shows the reduced scattering coefficient of the biological tissue phantom. As shown in figure 2.11(b), the reduced scattering coefficient increased as increase of the concentration of aqueous solution of lipid droplets. These results indicate that the optical properties measurement system can estimate the verification of the concentration of the scatter in the turbid media.

2.4 Conclusions

The optical properties measurement system combining of the double integrating sphere apparatus and inverse MC method allows the optical properties of turbid media accurately. Validation results indicate that the absorption coefficient of the turbid media have been measured accurately. And, the maximum relative error of the reduced scattering coefficient was 14.89%.

References

1. C. R. Simpson, M. Kohl, M. Essenpreis, and M. Cope, Near-infrared optical properties of ex vivo human skin and subcutaneous tissues measured using the Monte Carlo inversion technique, *Phys. Med. Biol.*, vol. 43, 2465–2478, 1998.

2. A. N. Bashkatov, E. A. Genina, V. I. Kochubey, and V. V. Tuchin, Optical properties of human skin, subcutaneous and mucous tissues in the wavelength range from 400 to 2000 nm, *J. Phys. D: Appl. Phys.*, vol. 38, 2543–2555, 2005.
3. S. C. Gebhart, W. C. Lin, and A. Mahadevan-Janseb, In vitro determination of normal and neoplastic human brain tissue optical properties using inverse adding- doubling, *Phys. Med. Biol.*, vol. 51, 2011–2027, 2006.
4. P. Parsa, S. L. Jacques, and N. S. Nishioka, Optical properties of rat liver between 350 and 2200 nm, *Applied Optics*, 28, 2325–2330, 1989.
5. R. Ulibricht, Photometer for mean spherical candle-power, *Electrotech. Zeit.*, 21, 595–597, 1900.
6. A. Roggan, M. Friebel, K. Dorschel, A. Hahn, and G. Muller, Optical properties of circulating human blood in the wavelength range 400-2500 nm, *J. Biomed. Opt.*, 4(1), 36–46, 1999.
7. T. L. Troy, and S. N., Thennadil, Optical properties of human skin in the near infrared wavelength range of 1000 to 2200 nm, *J. Biomed. Opt.*, 6(2), 167–176, 2001.
8. H.-J.Wei, D. Xing, G.-Y. Wu, H.-M. Gu, J.-J. Lu, Y. Jin, X.-Y. Li, Differences in optical properties between healthy and pathological human colon tissues using a Ti:sapphire laser: an in vitro study using the Monte Carlo inversion technique, *J. Biomed. Opt.*, 10(4), 044022; 1–8, 2005.
9. M. Meinke, G. Muller, J. Helfmann, and M. Friebel, Optical properties of platelets and blood plasma and their influence on the optical behavior of whole blood in the visible to near infrared wavelength range, *J. Biomed. Opt.*, 12(1), 014024; 1–9, 2007.
10. M. Friebel, A. Roggan, G. Muller, and M. Meinke, Determination of optical properties of human blood in the spectral range 250-1100 nm using Monte Carlo simulations with hematocrit-dependent effective scattering phase functions, *J. Biomed. Opt.*, 11(3), 034021; 1–10, 2006.
11. E. Salomatina, B. Jiang, J. Novak, and A. N. Yaroslavsky, Optical properties of normal and cancerous human skin in the visible and near-infrared spectral range, *J. Biomed. Opt.*, 11(6), 064026; 1–9, 2006.
12. C. F. Bohren, and D. R. Huffman, Absorption and Scattering of Light by Small Particles, Wiley, New York, 1983.
13. http://omlc.ogi.edu/software/mie/

14. K. Chen, A. Kromin, M. P. Ulmer, B. W. Wessels, and V. Backman, Nanoparticle sizing with a resolution beyond the diffraction limit using UV light scattering spectroscopy, Optics Communications, 228, 1–7, 2003.
15. S. N. Kasarova, N. G. Sultanova, C. D. Ivanov, and I. D. Nikolov, Analysis of the dispersion of optical plastic materials, *Optical Materials*, 29, 1481–1490, 2007.
16. G. M. Hale and M. R. Querry, Optical Constants of water in the 200-nm to 200-μm wavelength region, *Applied Optics*, 21(3), 555–563.
17. A. N. Bashkatov, E. A. Genina, V. I. Kochubey, V. V. Tuchin: Optical properties of human skin, subcutaneous and mucous tissues in the wavelength range from 400 to 2000 nm., *J. Phys. D. Appl. Phys.*, 38: 2543–2555, 2005.
18. S. L. Jacques: Modeling light transport in tissue, A. M. Verga Scheggi, S. Martellucci, A. N. Chester, R. Pratesi (eds), Biomedical Optical Instrumentation and Laser-Assisted Biotechnology, 21–32, Kluwer Academic, 1996.
19. H. J. van Staveren, C. J. M. Moes, J. van Marie, S. A. Prahl, and M. J. C. van Gemert, Light scattering in Intralipid-10% in the wavelength range of 400-1000 nm, *Appl. Opt.*, 30, 4507–4515, 1991.
20. S. T. Flock, S. L. Jacques, B. C. Wilson, W. M. Star, and M. J. C. van Gemert, Optical properties of Intralipid: a phantom medium for light propagation studies, *Lasers Surg. Med.*, 12, 510–519, 1992.
21. L.-H.Wang, S. L. Jacques, and L.-Q. Zheng, MCML-Monte Carlo modeling of photon transport in multi-layered tissues, *Comput. Methods Programs Biomed.*, 47(2), 131–146, 1995.
22. S. T. Flock, S. L. Jacques, B. C. Wilson, W. M. Star, M. J. C. van Gemert: Optical properties of intralipid: A phantom medium for light propagation studies. *Lasers Surg. Med.*, 12(5): 510–519, 1992.
23. Web site of Oregon Medical Laser Center at Providence St. Vincent Medical Center, http://omlc.ogi.edu/spectra/hemoglobin/index.html
24. 尾崎幸洋, 近赤外分光の基礎: 尾崎幸洋, 河田聡（編集）, 近赤外分光法, 11–58, 学会出版センター, 2005.

Figures

Table 2.1 Double integrating sphere system specifications.

	Measurement wavelength [nm]	
	350–1000	1000–2100
Light source	Xenon lamp (L2274(GS) and C8849, Hamamatsu Photonics K.K.)	Halogen lamp (LS-H150IR-FBC, Sumita Optical Glass Inc.)
Detector	Wavelength dispersive spectrometer (Maya2000 Pro, Ocean Optics)	Wavelength dispersive spectrometer (NIR256-2.5, Ocean Optics)
Wavelength resolution [nm]	0.42–0.47	6.77–7.82
Integration time [ms]	100	600
Spetra averaged	200	5
S/N ratio (max.) [dB]	36.305	32.944
S/N ratio (min.) [dB]	23.210	20.636
Dispersion of measurement [%]	<1.2	<1.7

Table 2.2 Refractive indices of polystyrene[14,15] which composed in latex beads and water[16].

Wavelength	Refractive index		Wavelength	Refractive index	
[nm]	Polystyrene	Water	[nm]	Polystyrene	Water
450	1.61	1.337	750	1.58	1.330
475	1.61	1.336	775	1.58	1.330
500	1.60	1.335	800	1.58	1.329
525	1.60	1.334	825	1.58	1.329
550	1.60	1.333	850	1.58	1.329
575	1.59	1.333	875	1.58	1.328
600	1.59	1.332	900	1.57	1.328
625	1.59	1.332	925	1.57	1.328
650	1.59	1.331	950	1.57	1.327
675	1.58	1.331	975	1.57	1.327
700	1.58	1.331	1000	1.57	1.327
725	1.58	1.330			

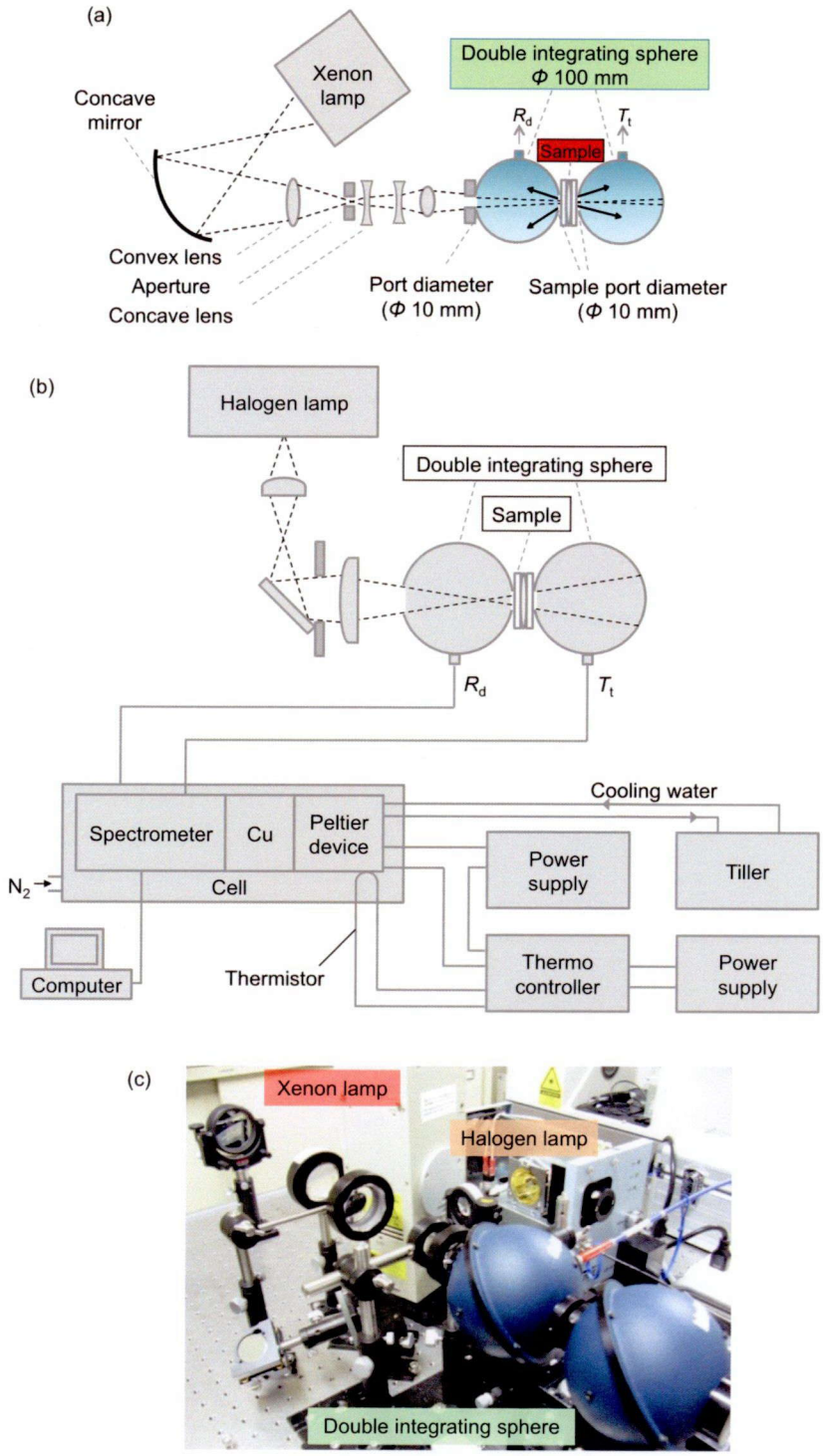

Figure 2.1 Schematic of the experimental setup of double integrating sphere system. (a) The optical system in the wavelength range of 350–1000 nm. (b) The optical system in the wavelength range of 1000–2100 nm. (c) Photograph of the double integrating sphere optics.

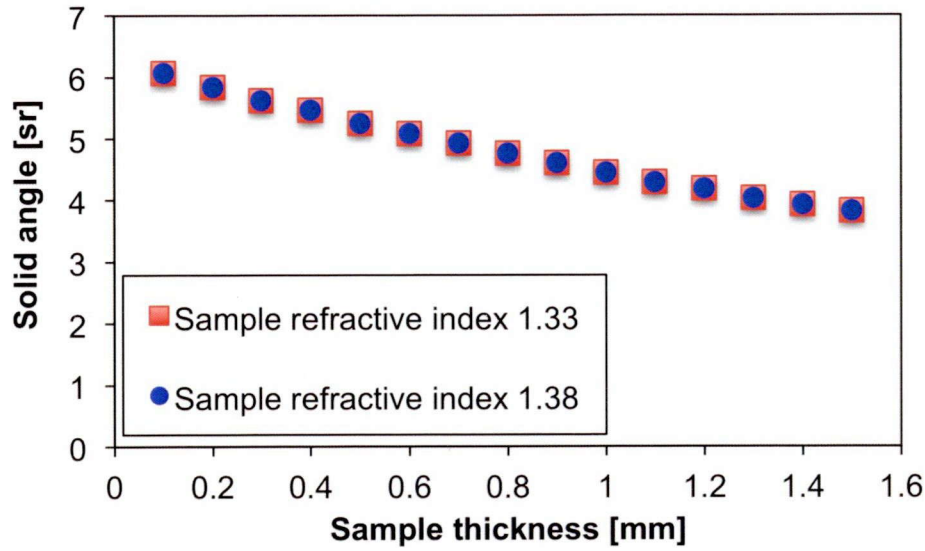

Figure 2.2 Solid angle of acceptance for the integrating sphere dependence of sample thickness. Refractive index of the sample was varied 1.33 and 1.38.

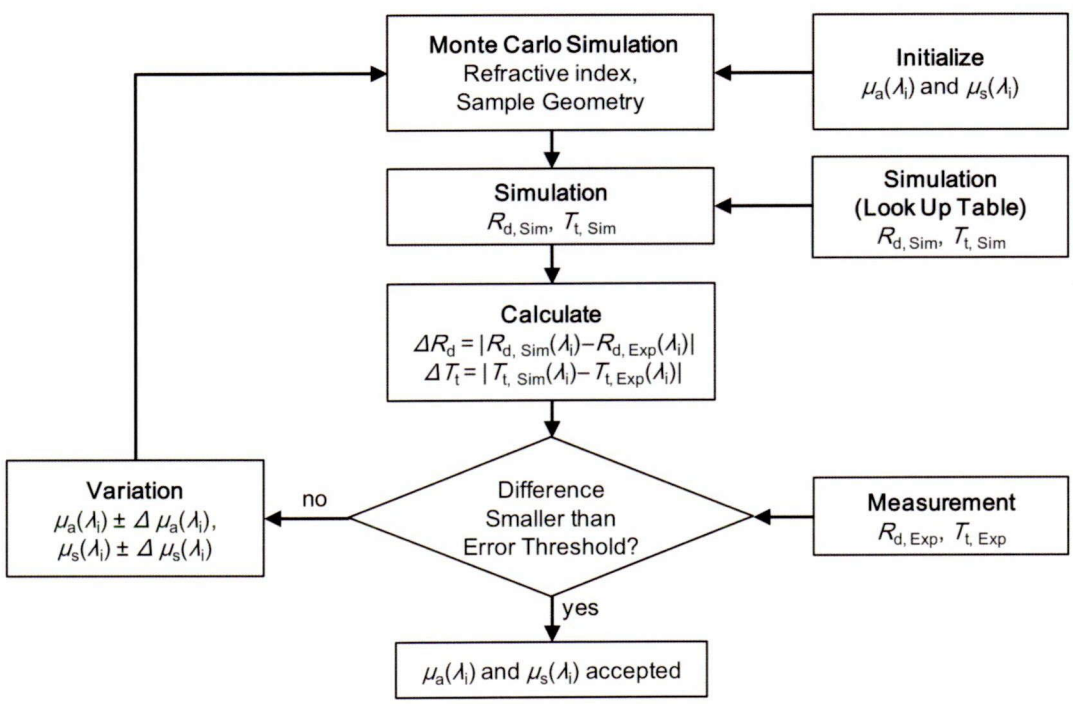

Figure 2.3 Flow chart of inverse MC simulation for calculation of optical properties.

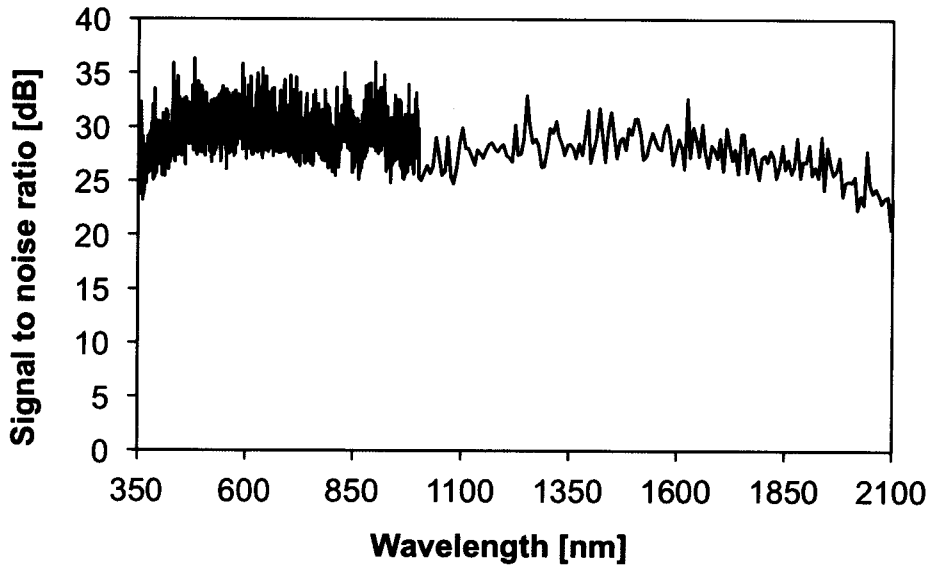

Figure 2.4 Signal to noise ration of the single beam of the double integrating sphere optics.

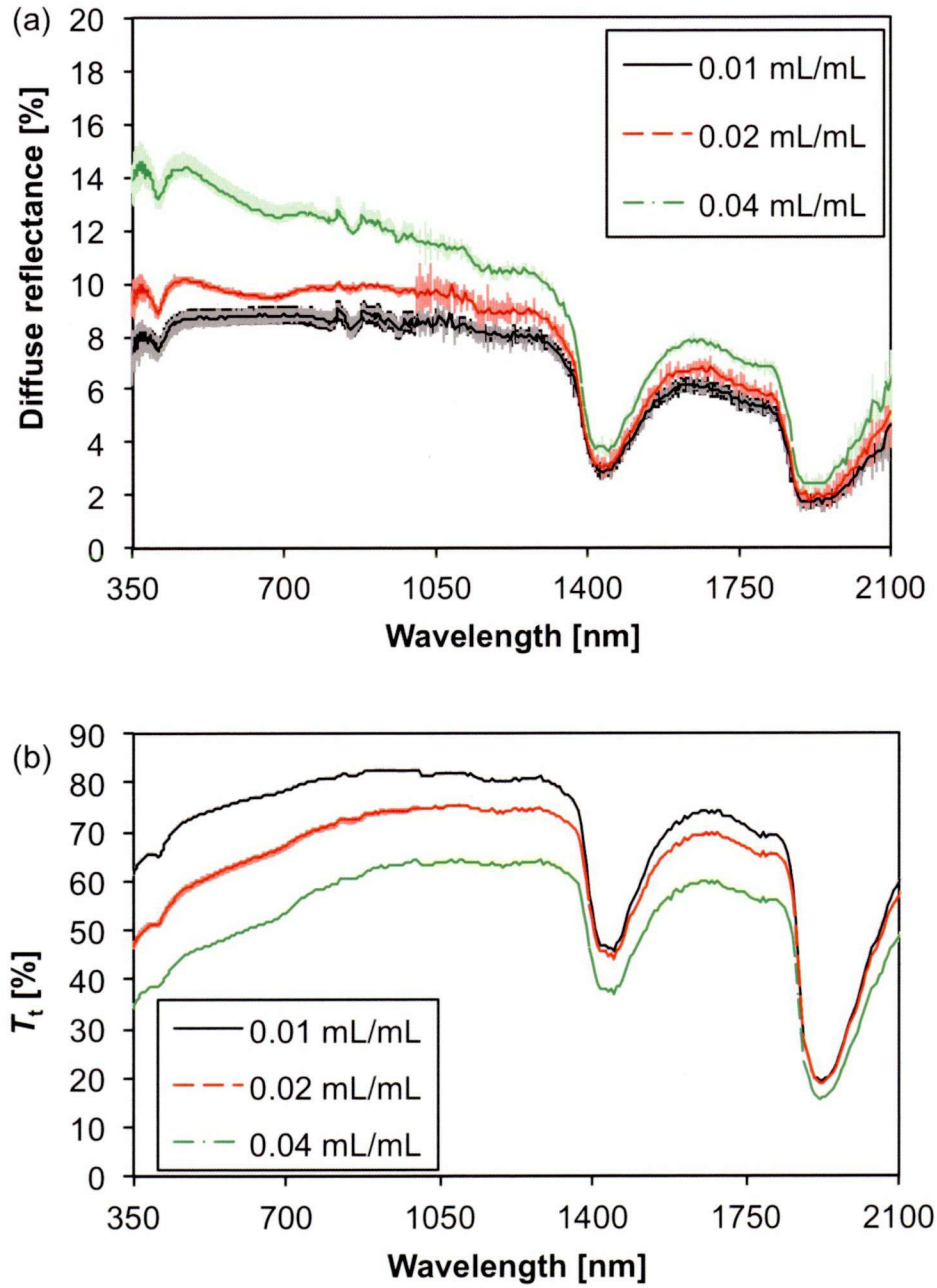

Figure 2.5 Diffuse reflectance R_d spectra (a) and transmittance T_t spectra (b) of the phantom varied with the aqueous solution of lipid drops 0.01, 0.20, and 0.04 mL/mL in the wavelength range of 350–2100 nm. The vertical lines show the maximum values and the minimum vaues of the measurement of five times.

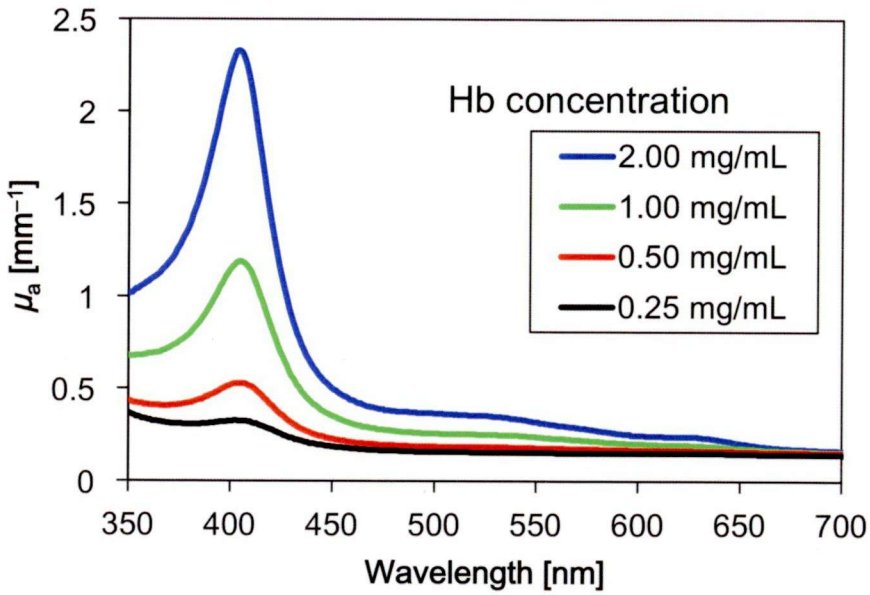

Figure 2.6 Absorption coefficient μ_a spectra of 0.25, 0.50, 1.00, and 2.00 mg/mL hemoglobin in 0.04 mL/mL aqueous solution of lipid droplets and 1.00×10^2 mg/mL gelatin.

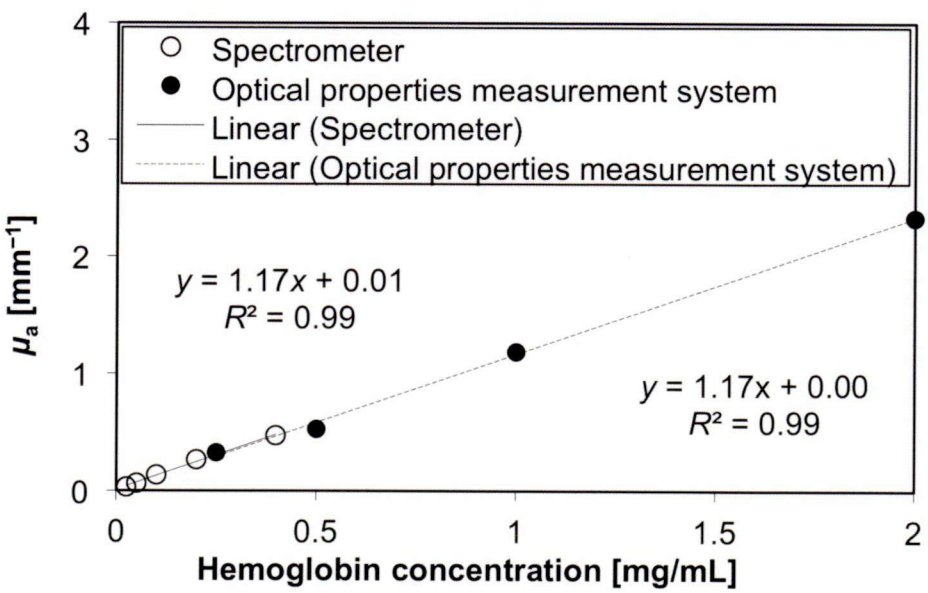

Figure 2.7 The absorption coefficient μ_a at the wavelength of 403 nm as a function of hemoglobin concentration in aqueous suspension of lipid droplets measured by the optical properties measurement system (solid circles). The open circles show the absorption coefficient at 403 nm as a function of hemoglobin concentration in water measured by the spectrometer.

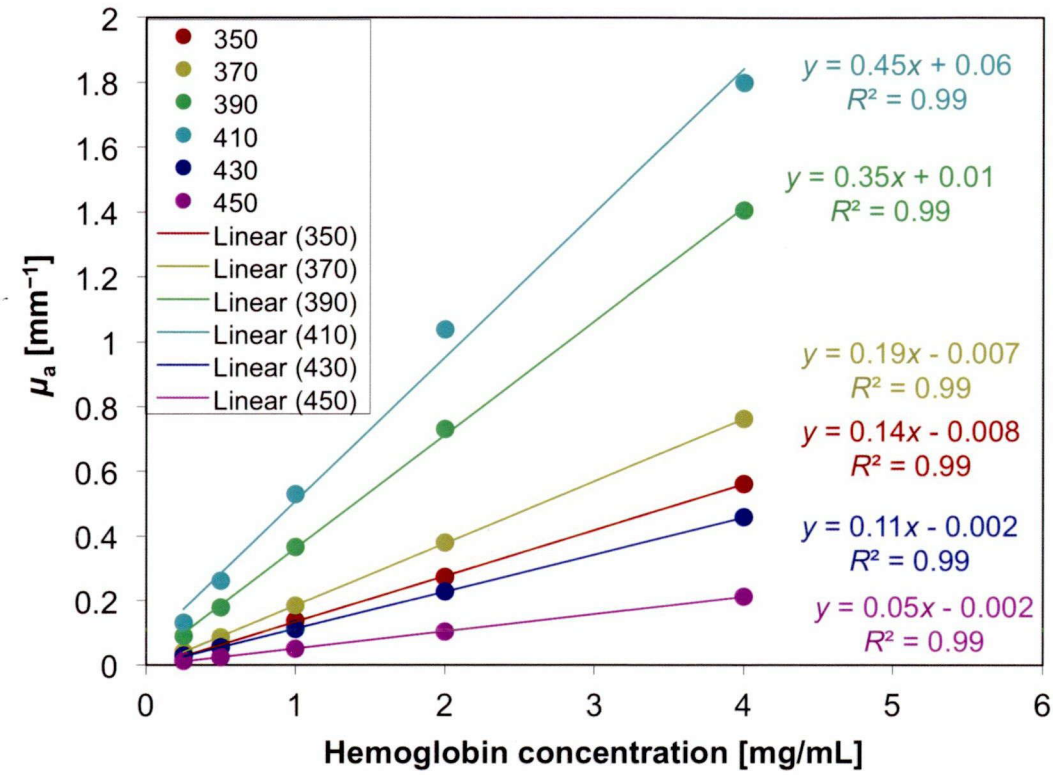

Figure 2.8 Absorption coefficient μ_a at 350, 370, 390, 410, 430, 450 nm as a function of hemoglobin concentration in aqueous suspension of lipid droplets.

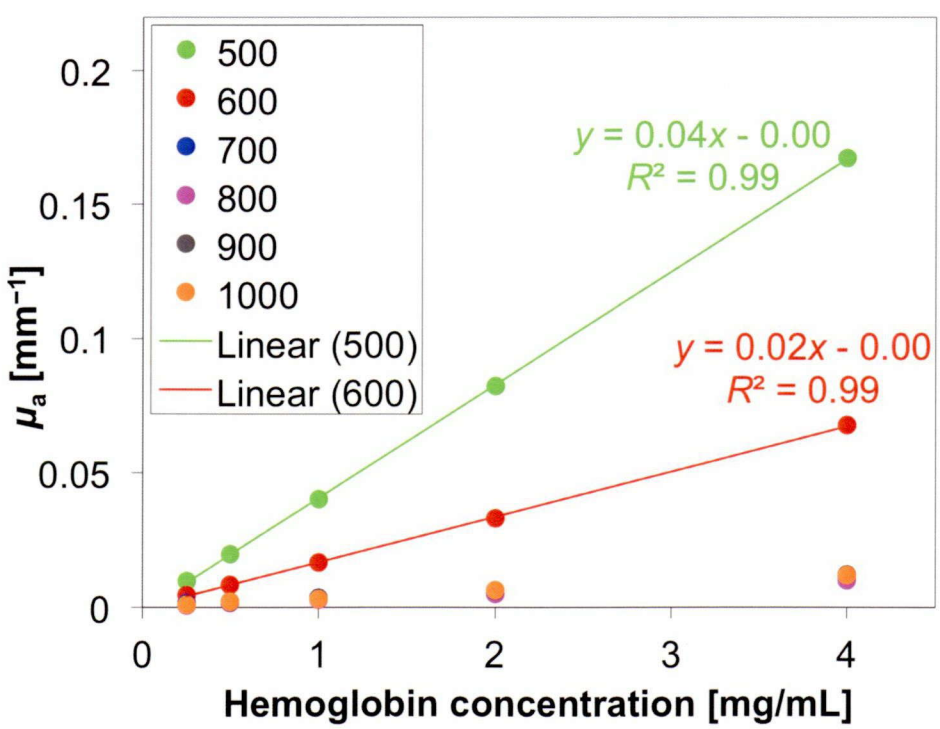

Figure 2.9 Absorption coefficient μ_a at 350, 370, 390, 410, 430, 450 nm as a function of hemoglobin concentration in aqueous suspension of lipid droplets.

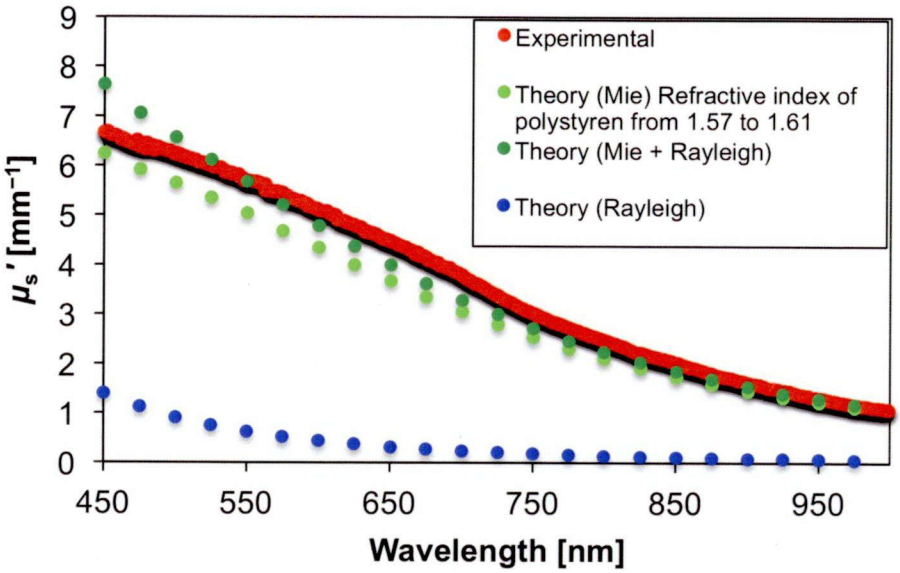

Figure 2.10 Reduced scattering coefficient μ_s' spectra of latex microspheres suspensions in gelatin water within the wavelength range of 450–1000 nm. The particle diameters and volume fraction are 200 nm and 0.01 mg/mL, respectively. The bold solid line is the experimentally measured values, and the dashed lines that predicted by the Mie scattering theory or Rayleigh scattering. The solid line shows the combination of the Mie and Rayleigh scattering.

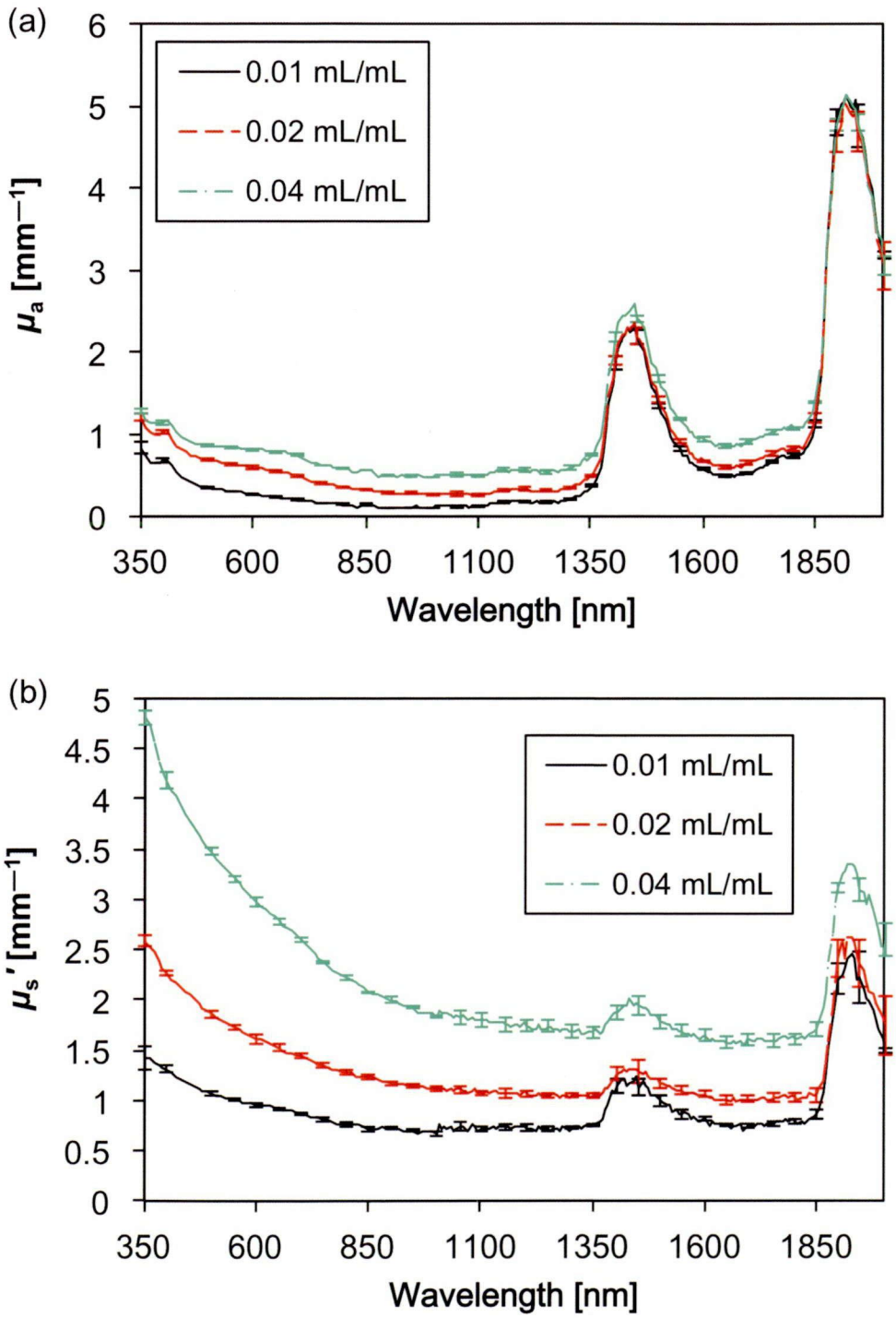

Figure 2.11 Absorption coefficient μ_a and the reduced scattering coefficient μ_s' spectra of the sample which is composed of 1.0 mg/mL hemoglobin, 0.01–0.04 mL/mL aqueous suspensions of lipid droplets and 1.00×10^2 mg/mL gelatin in the wavelength range of 350–2100 nm. The vertical lines show the SD values. (a) The absorption coefficient μ_a spectra of the sample. (b) The reduced scattering coefficient μ_s' spectra of the sample.

Chapter 3

Optical Properties Measurement of Laser Coagulated Tissues in the Wavelength Range of 350 to 2100 nm

3.1 Introduction

The propagation of light within tissues is an important issue in the dosimetry of the laser treatment. The knowledge of tissue optical properties are needed due to the light distribution within tissue depends on the optical properties[1]. For example, LITT of tumor tissues[2,3] is established alternatives to surgical resection for treating tumor tissue.

Deep-seated tumors, however, are not accessible in the noncontact mode owing to limited light penetration. For that purpose, the light may be delivered interstitially by implanting the laser fiber directly into the malignant tissue. This type of therapy has been applied experimentally and clinically with varying degrees of success to brain, skin, pancreatic, and hepatic tumors. Three different methods of thermal destruction can be distinguished de- pending mainly on the exposure time to an increased tissue temperature (determined by laser parameters and tissue optical- and thermal properties)[4,5]: (1) hyperthermia at temperatures of 42–45°C, causing reversible damage to cellular enzymes that may become irreversible after longer exposer times (25 minutes to several hours), (2) coagulation and vaporization at temperatures of 60–140°C, causing protein denaturation, hyalinization of collagen, and cell shrinkage, which can be observed macroscopically by tissue blanching, and (3) carbonization and ablation at temperatures of 300–1000°C, causing charring with increased light absorption and smoke generation.

Until now, thermal interstitial laser destruction has been achieved by either hyperthermia or tissue carbonization combined with coagulation. The concept of hyperthermia is based on a possible higher susceptibility of the malignant tissue to slight temperature increase[6,7]. The tissue temperature can be kept at the indicated level of about 43°C using temperature feedback systems and frosted or water-cooled fiber ends. Disadvantages of hyperthermia, however, are the long exposure times and unpredictable sensitivity of the malignant tissue.

This chapter was originally published under the titile, "Optical properties measurement of laser coagulated tissues with double integrating sphere and inverse Monte Carlo technique in the wavelength range from 350 to 2100 nm" by N. Honda, T. Nanjo, K. Ishii, K. Awazu in Proceedings of SPIE, 8221: 82211F, 2012

Tissue ablation combined with coagulation has been applied most commonly with a bare-tip fiber. This is a normal flexible quartz fiber of which the distal cladding has been stripped for 3–4 mm. The heat generated by this fiber, however, is very localized and intense, as the emission of laser light is concentrated at the fiber tip. Several studies have reported the development of a blackish clot at the insertion site, which absorbed the laser light efficiently and suppressed the transmission into the tissue by several orders[8-10]. Thus a charred fiber acts as a hot tip, which may limit precision and extent of the induced necrosis by depending on heat diffusion rather than light penetration and subsequent heat diffusion[11].

For selective coagulation of malignant tumor within the tissue in thermal laser coagulation, the understanding of light distribution is needed. The change of tissue optical properties by laser treatments is particularly interesting[3,12]. The light propagations change according to the change of tissue optical properties in laser irradiation. This phenomenon is clinically very important for realization of effective laser treatments because the understanding of change of optical properties can realize the pre-estimated treatment effects. The optical properties of various normal and pathologic tissues have been determined at single wavelength or over broad wavelength range. However, to my knowledge, there are a few experimental studies about alternation of the tissues considered from the aspect of the optical properties after laser coagulation[3,12]. Therefore, the aim of this Chapter is to determine and compare the optical properties of native and coagulated tissues in the spectral range from 350 nm to 2100 nm using a double integrating sphere optical system combined with an inverse MC method. The double integrating sphere setup[13–17] and inverse MC method[15-20] are used for determination of optical properties of tissue samples. The simple geometry of the *in vitro* measurement allowed optical properties of tissue: reduced scattering coefficient μ_s' and absorption coefficient μ_a. These tissue parameters become available for more models to predict optical distributions in tissues. This paper presents 1) the measurement of optical properties of the native state and laser coagulated tissue, and 2) the estimation of optical penetration depth of the tissues, and 3) the estimation of light distribution in the laser irradiated tissue by MC simulation.

3.2 Materials and Methods

3.2.1 Sample preparation

The optical properties of the laser coagulated chicken breast tissue were measured. The tissue was irradiated with a CO_2 laser emitting continuous wave laser light at a wavelength of 10.6 μm. Irradiation conditions were as follows. Power density was 2.1 W/cm^2. Irradiation time

was 30 s. After laser irradiation, samples were cut using a surgical knife and scissors. The samples, native and coagulated, were 1.0 mm in thickness. Cut tissues were placed on a glass slide and were covered with another glass slide to minimize the usual irregularities in the tissue surface. One specimen was investigated.

3.2.2 Optical properties measurement system

In R_d and T_t measurement by using a double integrating sphere, the entrance port size was 10.0 mm in diameter. The sample illumination between 350 and 2100 nm was achieved using a xenon light source and a 150 W halogen light source. The detector was cooled by using the peltier units (PS-50W, Takagi MFG, Japan).

3.2.3 Simulation of light distribution in tissues

To simulate of the light transport in tumor tissues, the MC technique[1] was employed. A total of 1×10^6 photons were launched for specified wavelength in order to simulate the light distribution with adequate precision. The incident photon beam was a flat with total energy of 5 and 10 J and radius of 0.1 cm. The light distribution in the tissue by laser irradiation of 1060 nm continuous wave laser was estimated. The model mimics the native and coagulated tissues. In the coagulated model, I considered the tissue formed by two flat layer and infinite layers. In coagulation tissue model, the first layer was 0.1 cm thick coagulated tissue. The second layer was 0.6 cm thick native tissue. Each layer is described by the measured optical properties.

3.2.4 Heat transfer analysis

The heat deposition was individually calculated for each voxel after each time interval, considering a single-layer rectangle with edges, which runs parallel with the x and z, coordinate directions, respectively. Initially (time t = 0 s) the two-dimensional isotropic composite slab is at a specified temperature. Then, for $t > 0$, I assumed the start of the laser energy deposition on the soft tissue. After the calculation of the fluence during laser irradiation, the temperature rise due to laser absorption in target tissue is calculated by the next equation:

$$\Delta T(x,z,t) = \mu_a F(x,z,t)\, t \frac{1}{\rho C} \tag{3.1}$$

where $T(x, z, t)$ is the skin temperature [°C], and $F(x, z, t)$ is fluence rate [W/cm^2]. A constant initial tissue temperature of 27°C was used for the entire tissue volume. The thermo-physical

properties of soft tissue[21] used in this study were density ρ = 1020 kg/m^3, specific heat capacity C = 3450 J kg^{-1} K^{-1}, thermal conductivity k = 0.501 W m^{-1} K^{-1}, and the heat transfer coefficient[22] between the skin surface and the above medium h = 4000 W m^{-2} K^{-1}. The Crank-Nicolson finite difference method was used to solve the two-dimensional transient form of the heat-conduction equation in the following format:

$$\frac{k}{\rho C}\left\{\frac{\partial T^2(x,z,t)}{\partial^2 x}+\frac{\partial T^2(x,z,t)}{\partial^2 z}\right\}+\frac{S(x,z,t)}{\rho C}=\frac{\partial T(x,z,t)}{\partial t} \qquad (3.2)$$

where $S(x, z, t)$ is the heat source term [W m^{-3}]. The latent heat of water vaporization is not accounted in this study. The second term on the left hand side of Eq. (3.2) include the metabolic heat source. The metabolic heat generation rate was assumed as 300 W/m^3. Convection surface boundary condition was used for the solution of the bio-heat conduction model:

$$-k\left.\frac{\partial T(x,z,t)}{\partial z}\right|_{z=0}=h(T_{\text{med}}-T(x,z,t)|_{z=0}) \qquad (3.3)$$

where T_{med} is the temperature of the medium above the tissue surface (°C). In the simulation, irradiation power was assumed as 2 W. The radius of incident light is assumed as 0.2 mm. The fluence rate was 1592 W/cm^2. The 1 mm surface layer was assumed as coagulated region due to its temperature over 53 °C after 22 s irradiation. The affect of the induced coagulation zone was investigated by comparison of the fluence rate of incident light.

3.3 Results and Discussion

3.3.1 Absorption coefficient spectra of native and coagulated tissue

The samples were measured in the spectral range from 350 to 2100 nm. The μ_a and μ_s' of the sample were calculated using inverse MC technique. Absorption and scattering coefficients of native and coagulated of soft tissue are shown in figures 3.2 and 3.3. As shown in figure 3.2, absorption peaks around 410 and 540 nm appear in the spectra. For the native sample, the peaks are at 410 and 540 with μ_a values of 0.63 and 0.24 mm^{-1}, respectively. These peaks corresponded to the absorption of the hemoglobin[23]. Absorption of the native tissue in the near-infrared region is determined by water and lipid content. Water and lipid absorption bands overlap around 1200 nm[20]. The μ_a value at the wavelength of 1200 nm is 0.19 mm^{-1}. The stronger absorption was observed in the wavelength range from 1300 to 1600 nm. The μ_a value at the wavelength of 1460 nm is 1.26 mm^{-1}. And, the stronger absorption was observed in the wavelength range from 1800 to 2100 nm. The μ_a value at the wavelength of 1940 nm is

1.27 mm^{-1}. The values above 1300 nm follow the known water-induced absorption curve with two other typical bands of increased absorption at 1460 and 1940 nm[24]. The μ_a is not change significantly after tissue coagulation.

3.3.2 Reduced scattering coefficient spectra of native and coagulated tissue

There are considerable differences in the optical properties of native and laser coagulated tissue. The μ_s' in this study a continuous decrease from 1.4 mm^{-1} at the wavelength of 350 nm to 0.44 mm^{-1} at the wavelength of 2100 nm. This behavior of μ_s' has been described in the literature for many tissues[3,20]. In coagulated tissue, the value of μ_s' increased by a factor of 5 at the wavelength of 640 nm.

3.3.3 Penetration depth of light

Optical penetration depth δ into a tissue is an important parameter for the correct determination of the irradiation dose in laser treatment. Estimation of the light penetration depth can be performed with the equation[25]

$$\delta = \frac{1}{\sqrt{3\mu_a(\mu_a + \mu_s')}} \tag{3.4}$$

Calculation of the δ has been performed with μ_a and μ_s' values presented in figure 3.2 and 3.3 and the result is presented in figure 3.4. After coagulation, the δ decreased significantly in the wavelength range from 350 to 1300 nm. The value of δ of the coagulated tissues at the wavelength of 1060 nm is 2 times lower than the native state. The decreasing of optical penetration depth at the wavelength of 1060 nm might be primarily attributed to the marked change in scattering behavior.

3.3.4 Simulation of light distribution in tissues

Figure 3.5(a)–(c) shows the MC simulation results for fluence inside the tissues using the measured μ_a and μ_s' at the wavelength of 1060 nm. The results are shown as contour maps versus sample depth and radial distance, in which the values marked on the contours of figure 3.5(a)–(c) represent the light energy distribution inside the tissue, expressed in the units of J/cm^2. The coagulated layer, as shown in figure 3.5(a) and 3.5(b), influenced the fluence distribution in the tissue. Coagulated tissue with a large μ_s' scatters light energy, and consequently it is more difficult for light to propagate into the deeper area. If the light energy is 2 times higher than the ordinary irradiation energy, the depth of light energy distribution of

coagulated tissue is corresponding to the depth of the native tissue as shown in figure 3.5(c). This optimized light energy density is determined from the evaluated optical property of the coagulated tissue. In this way, the evaluation of light energy distribution by the determination of the tissues optical properties could be useful for optimization of the treatment procedure in LITT.

3.3.5 Temperature distribution

The basic principle of photocoagulation is to apply light source to the soft tissue through the optical fiber. The light energy is absorbed by the soft tissue and heats it. The soft tissue is destroyed after it is heated to a high enough temperature for coagulation. The ultimate goal of photocoagulation technology is to kill the cancer cells, while effectively preserving the healthy around normal tissue. Figure 3.6 shows the simulated results of temperature distribution in soft tissues based on a wavelength of 1064 nm and irradiation power of 2 W. The temperature distribution for energy deposition of 150 J shown in figure 3.6(a) and (b) are obtained from the native model and the model including the coagulation area on the surface, respectively. The depth over 53 °C in figure 3.6(a) and (b) was 4 and 3 mm, respectively. These results indicate that the coagulation depth decreases during the photocoagulation. It is fond that the temperature distribution in soft tissue is different due to the difference of fluence in tissue corresponding of the soft tissue coagulation. Figure 3.6(b) and (c) shows the comparison of temperature distribution between in case of the fluence rate of 1.6×10^3 W/cm^2 and 3.2×10^3 W/cm^2. In the case of figure 3.6(c) the depth over the 53 °C was 6 mm. These results show coagulation depth can be improved by the change of fluence rate of incident light.

3.3.6 Histological analysis

The reduced scattering coefficient of the coagulated tissues and the native tissues were 1.3 and 0.3 mm^{-1} at the wavelength of 1060 nm, respectively. The cause of this difference is investigated by the histological analysis. Figure 3.7 shows the cross section of the chicken breast tissue irradiated with CO_2 laser. It has been shown that specific phenomena, such as macroscopic shrinkage of breast tissue after coagulation. As a result, concentration of scattering inhomogeneities increases and tissues become optically denser, which leads to a significant increase of scattering coefficients. Furthermore, the scattering coefficient dependency of the scatter size was investigated by using Mie calculator[26]. For mimicking the optical properties of native tissue, the input parameters were set as below. Sphere diameter

was 10.0 microns, refractive index of medium was1.0, real refractive index of sphere was 1.4, imaginary refractive index of sphere was 0, wavelength in vacuum was 1.06 microns, and concentration of spheres was 0.00001 spheres/micron^3. Then, the reduced scattering coefficient at the wavelength of 1060 nm was calculated as 0.3 mm^{-1} by Mie theory. Likewise, the reduced scattering coefficient of coagulated tissue was calculated using Mie theory with below parameters. Sphere diameter was 22.33 microns, refractive index of medium was1.0, real refractive index of sphere was 1.4, imaginary refractive index of sphere was 0, wavelength in vacuum was 1.06 microns, and concentration was 0.00001 spheres/micron^3. As a results, when the scatter size doubles, the reduced scattering coefficient becomes1.3 mm^{-1} from 0.3 mm^{-1}. The increase of the reduced scattering coefficient after laser irradiation might be induced by the scatter size increase and/or the increase of the tissue inhomogeneities.

3.4 Conclusions

Optical properties of native and laser coagulated soft tissue were measured by the optical properties measurement system using the double integrating sphere system and inverse MC technique. In the wavelength range from 350 to 1300 nm, the μ_s' of coagulated tissues increased and the δ of the tissues decreased. Coagulated tissue with a large μ_s' scatters light energy, and consequently it is more difficult for light to propagate into the deeper area. The evaluation of light energy distribution by the determination of the tissues optical properties could be useful for optimization of the treatment procedure in LITT.

References

1. L.-H. Wang, S. L. Jacques, and L.-Q. Zheng, MCML-Monte Carlo modeling of photon transport in multi-layered tissues, *Comput. Methods Programs Biomed.* 47(2), 131–146 1995.
2. C. T. Germer, C. Isbert, D. Albrecht, A. Roggan, J. Pelz, J. P. Ritz, G. Muller, and H. J. Buhr, Laser-induced thermotherapy combined with hepatic arterial embolization in the treatment of liver tumors in a rat tumor model, *Ann. Surg.* 230(1), 55–62, 1999.
3. J.-P. Ritz, A. Roggan, C. Isbert, G. Muller, H. J. Buhr, and C.-T. Germer, Optical properties of native and coagulated porcine liver tissue between 400 and 2400 nm, *Lasers Surg. Med.*, 29(3), 205–212, 2001.
4. S. Thomsen, Pathologic analysis of photothermal and photomechanical effects of laser-tissue interactions, *Photochem. Photobiol.*, 53, 825–835, 1991.

5. A. J. Welch, M. Motamedi, S. Rastegar, G. L. LeCarpentier, and D. Jansen, Laser thermal ablation, *Photochem. Photobiol.* 53, 815–823, 1991.
6. S. B. Field, Hyperthermia in the treatment of cancer, *Phys. Med. Biol.*, 32, 789–811, 1987.
7. H. I. Robins, A. Hugander, and J. D. Cohen. Whole body hyperthermia in the treatment of neoplastic disease, *Radiol. Clin. N. Am.*, 9, 183–185, 1989.
8. K. Matthewson, P. Colderidge-Smith, J. P. O'Sullivan, T. C. Northfield, and S. G. Bown, Biological effects of intrahepatic Neodymium: Yttrium-Aluminum-Garnet laser photocoagulation in rats, *Gastroenterology*, 93, 550–557, 1987.
9. M. Panjehpour, B. F. Overholt, A. J. Milligan, M. W. Swaggerty, J. E. Wilkinson, and E. R. Klebanow, Nd:YAG laser-induced interstitial hyperthermia using a long frosted contact probe, *Lasers. Surg. Med.*, 10, 16–24, 1990.
10. Z. Elias, S. K. Powers, E. Atstupenas, and J. T. Brown, Hyperthermia from interstitial laser irradiation in normal rat brain, *Lasers Surg. Med.* 7, 370–375, 1987.
11. L. O. Svaasand, T. Boerslid, and M. Oeveraasen, Thermal and optical properties of living tissue: Application to laser induced hyperthermia, *Lasers Surg. Med.*, 5, 589–602, 1985.
12. A. N. Yaroslavsky, P. C. Schulze, I. V. Yaroslavsky, R. Schober, F. Ulrich, and H.-J. Schwarzmaier, Optical properties of selected native and coagulated human brain tissues in vitro in the visible and near infrared spectral range, *Phys. Med. Biol.*, 47, 2059–2073, 2002.
13. J. W. Pickering, S. A. Prahl, N. van Wieringen, J. F. Beek, H. J. C. M. Sterenborg, and van M. J. C. Gemert, Double-integrating-sphere system for measuring the optical properties of tissue, *Appl. Opt.*, 32(4), 399–410, 1993.
14. G. de Vries, J. F. Beek, G. W. Lucassen, and M. J. C. van Gemert, The effect of light losses in double integrating spheres on optical properties estimation, *IEEE J. Select. Top. Quantum Electron.*, 5(4), 944–947, 1993.
15. A. Roggan, M. Friebel, K. Dorschel, A. Hahn, and G. Muller, Optical properties of circulating human blood in the wavelength range 400-2500 nm, *J. Biomed. Opt.*, 4(1), 36–46, 1999.
16. T. L. Troy, and S. N. Thennadil, Optical properties of human skin in the near infrared wavelength range of 1000 to 2200 nm, *J. Biomed. Opt.*, 6(2), 167–176, 2001.
17. H.-J. Wei, D. Xing, G.-Y., Wu, H.-M. Gu, J.-J. Lu, Y. Jin, and X.-Y. Li, Differences in optical properties between healthy and pathological human colon tissues using a Ti:sapphire laser: an *in vitro* study using the Monte Carlo inversion technique, *J. Biomed. Opt.*, 10(4), 044022; 1–8, 2005.

18. M. Meinke, G. Muller, J. Helfmann, and M. Friebel, Optical properties of platelets and blood plasma and their influence on the optical behavior of whole blood in the visible to near infrared wavelength range, *J. Biomed. Opt.*, 12(1), 014024; 1–9, 2007.
19. M. Friebel, A. Roggan, G. Muller, and M. Meinke, Determination of optical properties of human blood in the spectral range 250 to 1100 nm using Monte Carlo simulations with hematocrit-dependent effective scattering phase functions, *J. Biomed. Opt.*, 11(3), 034021; 1–10, 2006.
20. E. Salomatina, B. Jiang, J. Novak, and A. N. Yaroslavsky, Optical properties of normal and cancerous human skin in the visible and near-infrared spectral range, *J. Biomed. Opt.*, 11(6), 064026; 1–9, 2006.
21. B. Choi, and A. J. Welch, Analysis of thermal relaxation during laser irradiation of tissue. *Lasers Surg. Med.*, 29, 351–359, 2001.
22. J. W. Tunnell, L. V. Wang, and B. Anvari, Optimum pulse duration and radiant exposure for vascular laser therapy of dark port-wine skin: a theoretical study, *Appl. Opt.*, 42, 1367–1378, 2003.
23. Web site of Oregon Medical Laser Center at Providence St. Vincent Medical Center, http://omlc.ogi.edu/spectra/hemoglobin/index.html
24. Web site of Oregon Medical Laser Center at Providence St. Vincent Medical Center, http://omlc.ogi.edu/spectra/water/index.html
25. R. Splinter and B. A. Hooper, "Light-tissue interaction variables," Chap. 5 in An Introduction to Biomedical Optics, 121-154, Taylor & Francis Group, New York, 2007.
26. Web site of Oregon Medical Laser Center at Providence St. Vincent Medical Center, http://omlc.ogi.edu/software/mie/

Figures

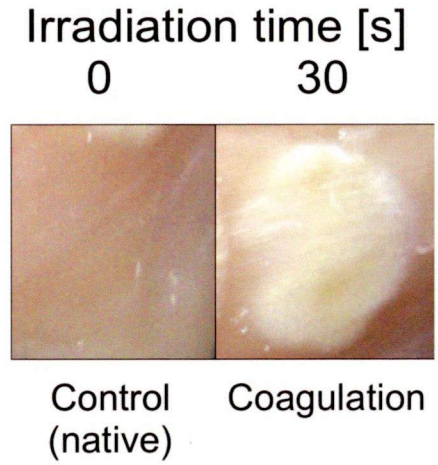

Figure 3.1 Photograph of the biological tissues after laser coagulation irradiated by CO_2 laser.

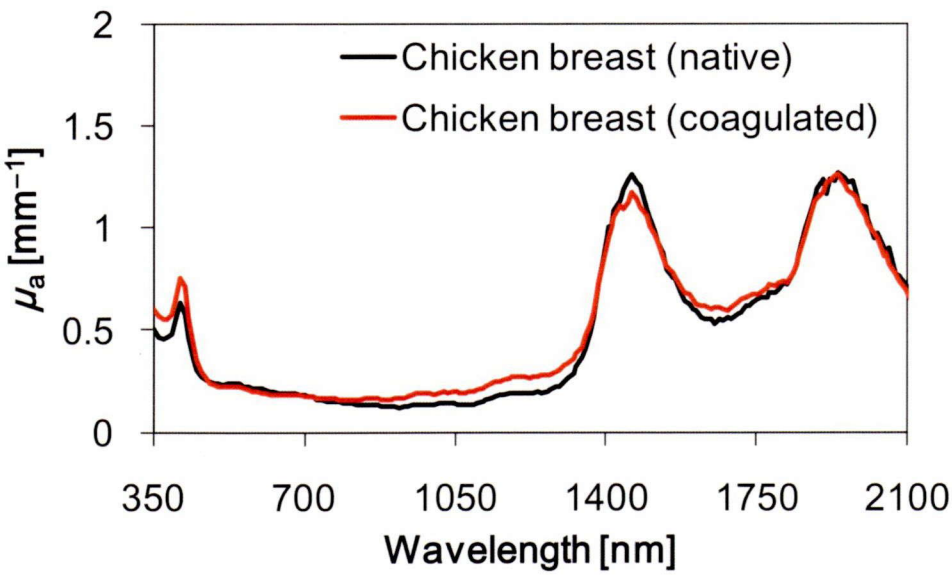

Figure 3.2 Absorption coefficient μ_a spectra of native and coagulated tissues. The tissue was irradiated with a 10.6 μm CO_2 laser. Power density was 2.1 W/cm^2. Irradiation time was 30 s.

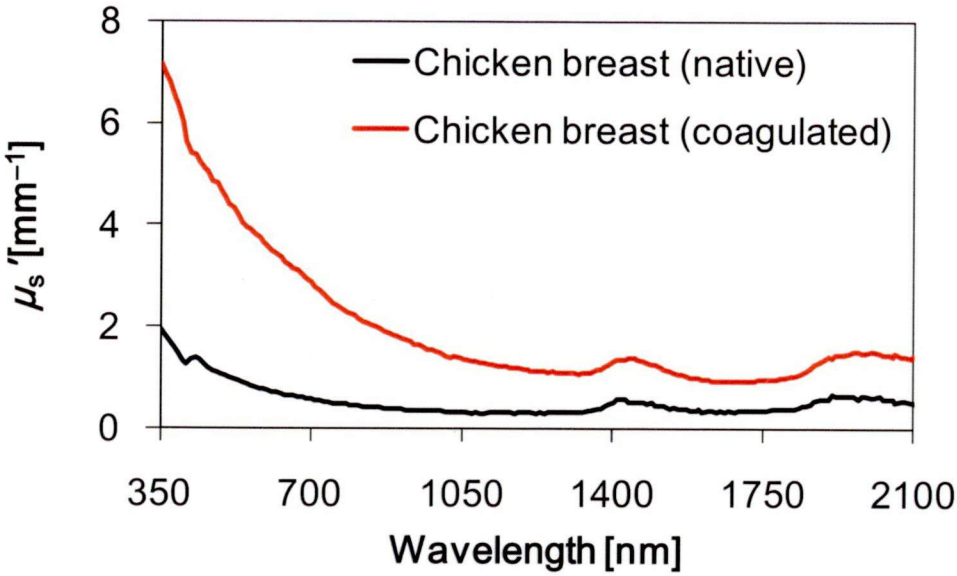

Figure 3.3 Reduced scattering coefficient μ_s' spectra of native and coagulated tissues. The tissue was irradiated with a 10.6 μm CO_2 laser. Power density was 2.1 W/cm^2. Irradiation time was 30 s.

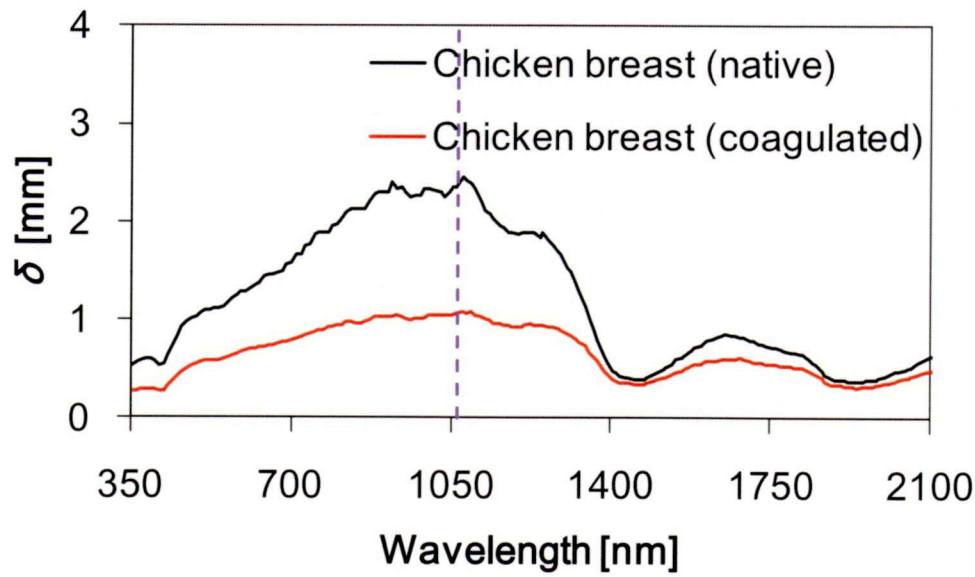

Figure 3.4 Optical penetration depth δ of the chicken breast tissue in native and coagulated in the wavelength range from 350 to 2100 nm. The dot line indicates at the wavelength of 1064 nm.

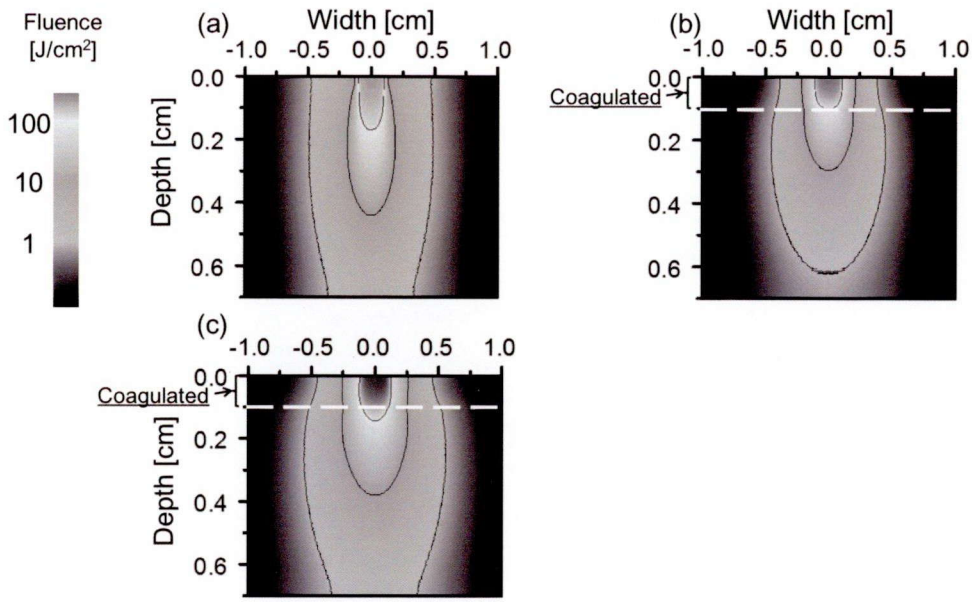

Figure 3.5 Monte Carlo simulation results for fluence inside the tissues using the measured μ_a and μ_s' at the wavelength of 1060 nm. (a) Native tissue model. (b) The simulation model composes of two layers. The type of tissue combines the 0.1 cm coagulated layer and the 0.6 cm native layer. (c) Laser energy of incident of light was doubled by changing incident light energy in figure 3.5(b).

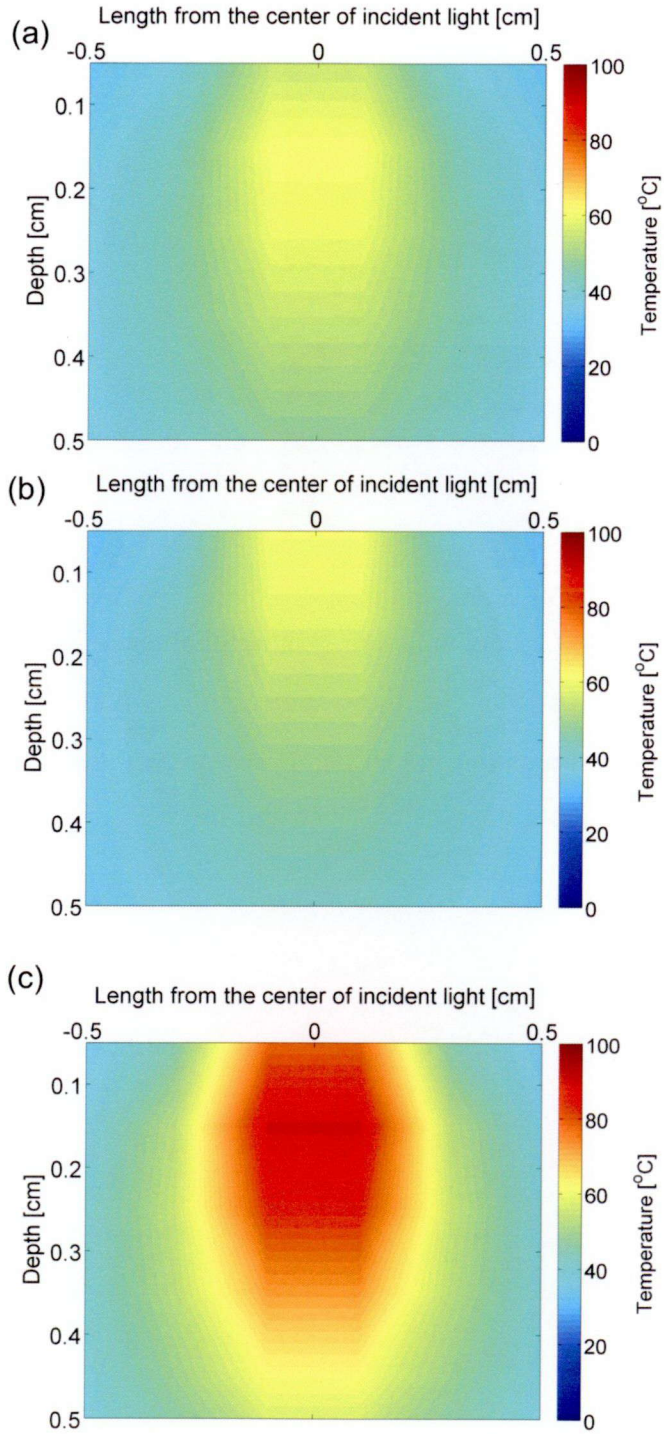

Figure 3.6 Temperature distribution in soft tissue for various model and fluence rate. (a) Native tissue model. (b) The simulation model composes of two layers. The type of tissue combines the 0.1 cm coagulated layer and the 0.6 cm native layer. (c) The fluence rate of incident light was doubled by changing in figure (b).

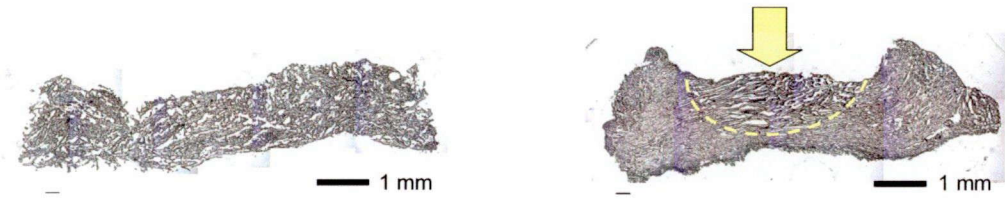

Figure 3.7 Morphological change of the breast tissue after the coagulation by laser irradiation. Left figure shows the cross section of the native chicken breast tissue. Right figure shows the cross section of the coagulated tissue. Arrow indicates the irradiation direction.

Chapter 4

Optical Properties of Tumor Tissues during and after Photodynamic Therapy

4.1 Introduction

PDT uses a photosensitizer or a photoactivated dye in combination with a visible light that produces a reactive oxygen species and destroys both tumor cells and malignant tissue[1]. The PDT efficacy depends on the light excitation energy distribution, photosensitizer concentration, and oxygen transport and consumption during the treatment. However, conventional PDT does not consider the laser irradiation dose during PDT. For the optimization of treatment planning, it is essential to know how light is transported within the tissue. Using knowledge of the optical properties of the target tissue, the light distribution and propagation within the tissue can be estimated[2].

The change of optical properties by laser treatments is particularly interesting. The light propagation within the tissue changes according to the change of optical properties in laser irradiation[3,4]. Recently, the optical properties of various normal and pathologic tissues have been determined at a single wavelength or over a broad wavelength range. However, there is little information about the change of the optical properties of tissues by PDT in the wide wavelength range[5–8]. The light fluence rate in tissue by the determining the optical properties of PDT treated tissue in PDT realizes a pre-estimated and safe treatment effect.

The objective of this study is to determine the optical properties of tissues, which are treated by PDT in the wavelength range from 350 nm to 1000 nm. In this study, the mouse tumor model which inoculated Lewis lung carcinoma cells was used to perform PDT-treatment on tumor tissue. The optical properties of tissues were determined by using the double integrating sphere measurement system[9–13] combined with the inverse MC method[11–16]. This paper presents the determination of the optical properties of mouse tumor tissues during and after PDT *in vitro*, and the optical penetration depth of the tumor tissue.

This chapter was originally published under the title, "Determination of the tumor tissue optical properties during and after photodynamic therapy using inverse Monte Carlo method and double integrating sphere between 350 and 1000 nm" by Norihiro Honda, Katsunori Ishii, Takaya Terada, Takuya Nanjo, and Kunio Awazu in Journal of Biomedical Optics, vol. 16, no. 5, 058003, 2011.

4.2 Materials and methods

4.2.1 Animals model and sample preparation

19 syngeneic male C57BL/6 mice at 6 weeks of age were used. The Lewis lung carcinoma (LLC) cells were maintained at 37 degrees Celsius and 5% CO_2 in Dulbecco's Modified Eagle's Medium (Sigma-Aldrich Inc., USA) containing 10% fetal calf serum (BioWest Inc., France), 100 units/mL penicillin, and 0.1 mg/mL streptomycin (Nacalai Tesque Inc., Japan). Cells were prepared at 1×10^7 cells/mL for injection. All animals received subcutaneous bolus injections of 0.1 mL of cell suspension in the lower dorsal region using a 23 gauge needle. Each tumor was grown for 7 days. Tumor diameter was reached about 11.5 mm on average. For optical property measurement of tissues, the animals were euthanized by an overdose of anesthesia. The tumor tissues were resected using a surgical knife. Then, the skin and the scab of the tissue were removed. The sample was approximately 2 mm in thickness except the sample, which obtained 7 days after treatment. The sample thickness of the tissue obtained 7 days after treatment was 1 mm due to the removed sample was 1 mm in thickness. Each section was positioned between slide glasses. The optical properties of the tissue were measured with the double integrating sphere setup within 30 minutes after sacrifice. The animal experimentation was carried out according to the guideline of animal experimentation of Osaka University.

4.2.2 PDT treatment

As a photosensitizer, talaporfin sodium (Laserphyrin®, MEIJI SEIKA KAISHA, Japan)[17] was used. 16 tumor-bearing mice were intravenously injected with talaporfin sodium. While the remaining 4 were control groups without injection. Before injection, talaporfin sodium was reconstituted in the physiological saline and used at a concentration of 5 mg/kg body weight. Talaporfin sodium was injected via the tail vein 2 hours prior to light exposure. The tumor surface was irradiated superficially through the skin with a laser diode emitting continuous wave laser light at a wavelength of 664 nm (UM1000 Dental_665, JENOPTIK unique-mode, Germany)[18]. The light was collimated with a lens, and the spot diameter was 12.5 mm. The animals were chosen at random to populate. Table 4.1 summarizes the treatment conditions. For determination of the tumor tissue optical properties during PDT, the irradiation was performed 1 minute to 5 mice before each measurement of the optical property. And, the light irradiation of 5 minutes was carried out to 5 mice. The average power density on the tumor surface was 100 mW/cm^2. For determination of the tissue optical properties after PDT, each tumor of 6 mice were irradiated with a light dose of 100 J/cm^2. The average power density on

the tumor surface was 100 mW/cm^2. During light irradiation individual animals were restrained un-anesthetized in holders. Then, 1, 2 and 7 days after PDT, the tumor tissue was resected and the tissue optical properties were measured.

4.2.3 Optical properties measurement

A double integrating sphere system was designed for the measurement of optical properties of biological tissues. This is also a convenient tool since it simultaneously measures R_d and T_t. Using an integrating sphere as both a diffuse illumination source and a detector provides a technically simple measurement apparatus. Balanced deuterium tungsten halogen source (DH-2000-BAL, Ocean Optics, USA) combined with high-powered halogen light source (HL-2000-HP, Ocean Optics, USA) were employed as a light source. Specimens were placed between two integrating spheres (FOIS-1, Ocean Optics, USA). The integrating sphere was 38.1 mm inner diameter. The inside surface of the sphere was coated with diffusely reflective material, Spectralon^{TM}. The entrance port size of the reflectance sphere was 8.0 mm in diameter and the sample port of both spheres was 9.5 mm in diameter. The beam-illuminated area was 3 mm in diameter on the sample. The incident light was diffusely reflected from the sample surface and the light was diffusely transmitted during the sample. Then, the reflected and transmission light were multiply scattered in spheres and recorded by spectrometer (Maya2000 Pro, Ocean Optics, USA) as R_d and T_t, respectively. From these experimental data, the set of optical properties were calculated using the inverse MC method.

The inverse MC method was employed to calculate the optical properties of samples from measured values of R_d and T_t. Calculation of the tissue optical properties was performed at each wavelength point. The algorithm consists of following steps:

a. To calculate the optical parameters (R_d and T_t) with MC simulations, which was developed by Wang *et al.*,[2] an initial set of optical properties had been estimated.
b. The MC simulation was performed on this initial set of data.
c. A simulated set of the optical parameters was compared to the actual measurements. If agreement between calculated and measured data was within a defined error limit (<0.5%), the set of optical parameters was accepted for the sample.
d. This procedure was repeated with a new set of optical properties until the error threshold was achieved. With this iterative process, the set of optical properties that yields the closest match to the measured values of reflectance and transmittance are taken as optical properties of the tissue. This method allows one to determine the μ_a and μ_s of a tissue from the measured values.

In these calculations, g was fixed at 0.9, since this value is typical for many tissues[19]. It is known that the volume-averaged refractive index of most biological tissue falls within 1.34 to 1.62 (Ref. 20) and the refractive index of the lung tissue is 1.38 (Ref. 21). Therefore, the refractive index of the sample is assumed to be 1.38 in this study.

4.2.4 Histological Study

Tumors were harvested after PDT and fixed in 8% buffered formalin. The tumors were then embedded in paraffin, and sliced. Sections were mounted on glass slides and stained with hematoxylin and eosin.

4.2.5 Statistical Analysis

A Student's t-test was used to evaluate the significance of the difference between obtained optical properties of tumor tissues. The differences between optical coefficients of control and PDT-treated tissues were considered to be statistically significant when the calculated probability valued (p value) was equal or less than 0.05. P value ≤ 0.05 means that the probability that the two data sets are different is $\geq$ 95%. This level of significance is considered acceptable for the biological samples.

4.3 Results

4.3.1 Macroscopic observations of photodynamic therapy effect

The tumor tissues after 1 and 5 minutes of irradiation did not show significant changes as shown in figure 4.1(b) and 4.1(d). However, the PDT-treated tumors showed changes 1, 2 and 7 days after PDT as shown in figure 4.1(f), 4.1(g) and 4.1(h). After PDT, a tumor showed a dusky black discoloration.

4.3.2 Tumor tissue optical properties during photodynamic therapy

Optical properties were calculated from the experimental measurements of R_d and T_t of 1 minute and 5 minutes irradiated tumor tissues for the determination of the optical property of the tumor tissue during PDT. The R_d and T_t spectra of the tumor tissues are shown in figure 4.2(a) and 4.2(b), respectively. The μ_a and μ_s' spectra of tumor tissues were shown in figure 4.3(a) and 4.3(b), respectively. There were several peaks in the μa spectra as shown in figure 4.3(a). For tumor tissues before PDT, the peaks were at 439 and 553 nm with mean μ_a values of 1.18 and 0.77 mm^{-1}, respectively. These peaks corresponded to the absorption of the hemoglobin[22]. Scattering, depicted in figure 4.3(b), was greater at shorter wavelength with a

peak value of about 1.52 mm^{-1} at the wavelength of 350 nm and declined smoothly over the visible range to a level of about 0.41 mm^{-1} at the wavelength of 1000 nm. During PDT, the μ_a and μ_s' spectra were not changed.

4.3.3 Tumor tissue optical properties after photodynamic therapy

The μ_a and μ_s' spectra of the tumor tissues 1, 2 and 7 days after PDT are shown in figure 4.4(a) and 4.4(b), respectively. The considerable difference of the mouse tumor tissue optical properties, before and after PDT, was observed. Table 4.2 summarizes optical properties changes observed in PDT-treated tumor tissues compared with before treatment tissues in a specific region for PDT-treatment from 600 to 700 nm for the individual wavelengths, such as 632, 664 and 690 nm. After PDT, the values of μ_s' increased with the passage of time as shown in figure 4.4(b).

4.4 Discussion

4.4.1 Histological analysis

It seems clear that a significant increase of μ_s' should be a result of substantial structural changes. As shown in figure 4.5, corresponding changes of mouse tumor tissue structures after PDT were revealed by a histological evaluation of the tumor samples and were compared to sections from non-PDT treated tissue. A histological analysis has shown that PDT causes the blood vessel disruption and leak of erythrocytes (figure 4.5 (e)). My histological findings confirm the results obtained by Nelson *et al.*[23] for mouse tumor tissues. It has been shown that specific phenomena, such as micro vascular disruption, occur after the completion of PDT. Furthermore, a leak of erythrocytes is caused by vascular damage. A mouse's red blood cell size is about 6 μm in diameter[24]. Blood is a scattering system that consists of scattering particles, such as red blood cells, their aggregates and the surrounding media (i.e. plasma). The refractive index mismatching between red blood cells cytoplasm and blood plasma is the major source of light scattering in blood[25]. The scattering properties of blood are dependent on RBC volume[11]. As a result, the concentration of chromophores and scattering inhomogeneities increases and tissues become optically denser, which likely leads to a significant increase of μ_s' in the spectral range from 600 to 1000 nm. 7 days after PDT, the PDT-treated tissues showed the decrease of tumor cells and fibrosis as shown in figure 4.5(f). This pathological change has been observed in the clinical treatment[26]. And, μ_s' of the tissue increased as shown in figure 4.4(b). Saidi *et al.* found that the large collagen fibers of the dermis were primarily responsible for the light scattering in the skin[27]. They indicated that

scattering of normally incident light by a single fiber, as predicted by Mie theory, was dependent on the wavelength of the indices of refraction of the fibers and of the surrounding medium. Perhaps, the collagen fibers shown in the PDT-treated tissue played a role of the scatter in the tissue. Then, the μ_s' of the treated tissue measured 7 days after treatment increased.

4.4.2 Penetration depth of light within tumor tissues during photodynamic therapy

The penetration depth[28] of light into a biological tissue is an important parameter for the correct determination of the irradiation dose in the PDT of various diseases. The estimation of the light penetration depth was performed with the equation (3.1) in Chapter 3.

The optical penetration depth of tumor tissues during PDT was calculated with the calculated optical properties presented in figure 4.3 and the results are presented in figure 4.6(a). The optical penetration depth of the tumor tissues after PDT was calculated with the optical properties presented in figure 4.4 and the result presented in figure 4.6(b). Table 4.3 summarizes optical penetration depth changes observed in PDT-treated tumor tissues compared with before treatment tissues in a specific region for PDT-treatment from 600 to 700 nm for the individual wavelengths, such as 632, 664 and 690 nm. Comparison of the tumor tissue optical properties before PDT obtained in this study and those presented by Bargo *et al.*[29] shows an agreement between them. The μ_a and μ_s' spectra of the sample are qualitatively similar to the reported spectra in the spectral range from 600 to 900 nm. Literature values[29] for *in vivo* optical properties of human lung tumor tissues at the wavelength of 630 nm have μa ranging from 0.097 to 0.488 mm^{-1} and μ_s' ranging from 0.63 to 1.15 mm^{-1}, which are in agreement with the results obtained in this study.

During PDT, the penetration depth of light was not changed. Recently, the optical properties of *in vivo* human prostate during motexafin lutetium-medicated photodynamic therapy has been presented by Zhu *et al.* for the wavelength 732 nm[8]. For the wavelength, the effective attenuation coefficient varied after PDT, although the magnitude of the change was generally much smaller. The inverse of the effective attenuation coefficient gives us an estimation of the penetration depth. These results are compatible with my results on the optical penetration depth obtained in this study. Swartling *et al.* researched the interstitial PDT with online feedback to deliver a tailored light fluence dose, exceeding a predefined threshold dose, to the whole prostate gland and adapt the dose plan in cases where the optical attenuation changes during the therapy[30]. They have reported that the optical properties of the gland tissue did not vary markedly during the treatment with Foscan® in clinical study. But,

Thompson *et al.* reported that light transmission decreased in nodular basal cell carcinomas during 5-amino levulinic acid mediated PDT[31]. They discuss that the light transmission changes are in fact due to the tissue oxygenation and changes in blood volume. Therefore, a system for interactively controlling the treatment to achieve the optimal therapy adapted for each case is needed in light dosimetry during PDT.

After PDT, the penetration depth decreased with the passage of time as shown in table 4.3. Compared to the tissue obtained before the treatment, the optical penetration depth of the tissue 7 days after PDT decreased by 1.4–1.8 times. In general, if the cancer was not cured after the first PDT-treatment, a second treatment was carried out in PDT[32]. In this study, we found the fact that the optical properties of PDT-treated tumor were changed. As a result, the light penetration depth of the mouse tumor tissues decreased after PDT. For conducting the re-irradiation of PDT precisely, the irradiation dose might be determined based on the optical properties of the PDT-treated tissues. The PDT-treated tissue optical properties until a complete recovery are being studied for future work.

It is difficult to accurate estimate the experimental error in a study of this type in which many independent measurements are conducted. Experimental contributions to the error included the inaccuracy of the spectrometer, which I estimate to be < 1% of the corresponding 100% value. This error becomes more prominent as the measured values of R_d and T_t become smaller, such as in the wavelength between 350 nm to 600 nm. Furthermore there is a significant biological variability between the samples. For example, if the blood of the samples varied, this would be particularly noticeable in the wavelength range between 350 to 600 nm. This may have introduced an error in the μ_s' spectra as shown in figure 4.3(b) and 4.4(b).

4. 5 Conclusions

The change of the optical properties of mouse tumor tissues by PDT in the wavelength range of 350–1000 nm was measured with the double integrating sphere system and the inverse MC technique. No significantly change could be detected during PDT. The optical property of the tumor tissue changed dramatically after PDT. Especially, the μ_s' increased after PDT. After PDT-treatment, resulting in the change of mouse tumor tissue optical property, the light penetration depth into the tumor tissue decreased with the passage of time. To ensure the effective treatment procedure, an adjustment of the laser parameter in view of the decreasing penetration depth is recommended for the re-irradiation PDT. These tissue parameters become available for more models to predict optical distributions in tissues. The optical

property obtained *in vitro* using the combination of double integrating sphere measurements and inverse MC method are clearly useful for in vivo applications.

References

1. A. P. Castano, T. N. Demidova, and M. R. Hamblin, Mechanisms in photodynamic therapy: Part three-Photosensitizer pharmacokinetics, biodistribution, tumor localization and modes of tumor destruction, *Photodiagnosis Photodyn. Ther.* 2(2), 91–106, 2005.
2. L.-H. Wang, S. L. Jacques, and L. Q. Zheng, MCML - Monte Carlo modeling of photon transport in multi-layered tissues, *Comput. Methods Programs Biomed.* 47(2), 131–146, 1995.
3. A. N. Yaroslavsky, P. C. Schulze, I. V. Yaroslavsky, R. Schober, F. Ulrich, and H.-J. Schwarzmaier, Optical properties of selected native and coagulated human brain tissues in vitro in the visible and near infrared spectral range, *Phys. Med. Biol.*, 47(12), 2059–2073, 2002.
4. J.-P. Ritz, A. Roggan, C. Isbert, G. Muller, H. J. Buhr, and C.-T. Germer, Optical properties of native and coagulated porcine liver tissue between 400 and 2400 nm, *Lasers Surg. Med.*, 29(3), 205–212, 2001.
5. R. van Hillegersberg, J. W. Pickering, M. Aalders, and J. F. Beek, Optical properties of rat liver and tumor at 633 nm and 1064 nm, Photofrin enhances scattering," *Lasers Surg. Med.*, 13(1), 31–39, 1993.
6. A. M. K. Nilsson, R. Berg, and S. Andersson-Engels, Measurements of the optical properties of tissue in conjunction with photodynamic therapy, *Appl. Opt.*, 34(21), 4609–4619, 1995.
7. H.-J. Wei, D. Xing, J.-J. Lu, H.-M. Gu, G.-Y. Wu, and Y. Jin, Determination of optical properties of normal and adenomatous human colon tissues *in vitro* using integrating sphere techniques, *World J. Gastroenterol.*, 11(16), 2413–2419, 2005.
8. T. C. Zhu, A. Dimofte, J. C. Finlay, D. Stripp, T. Busch, J. Miles, R. Whittington, S. B. Malkowicz, Z. Tochner, E. Glatstein, and S. M. Hahn, Determination of the distribution of light, optical properties, drug concentration, and tissue oxygenation in-vivo in human prostate during motexafin lutetium-mediated photodynamic therapy, *J. Photochem. Photobiol. B, Biol.*, 79(3), 231–241, 2005.
9. J. W. Pickering, S. A. Prahl, N. van Wieringen, J. F. Beek, H. J. C. M. Sterenborg, and M. J. C. van Gemert, Double-integrating-sphere system for measuring the optical properties of tissue, *Appl. Opt.*, 32(4), 399–410, 1993.

10. G. de Vries, J. F. Beek, G. W. Lucassen, and M. J. C. van Gemert, The effect of light losses in double integrating spheres on optical properties estimation, *IEEE J. Sel. Top. Quantum Electron.*, 5, 944–947, 1999.
11. A. Roggan, M. Friebel, K. Dörschel, A. Hahn, and G. Müller, Optical properties of circulating human blood in the wavelength range 400-2500 nm, *J. Biomed. Opt.*, 4(1), 36–46, 1999.
12. T. L. Troy, and S. N. Thennadil, Optical properties of human skin in the near infrared wavelength range of 1000 to 2200 nm, *J. Biomed. Opt.*, 6(2), 167–176, 2001.
13. H.-J. Wei, D. Xing, G.-Y. Wu, H.-M. Gu, J.-J. Lu, Y. Jin, and X.-Y. Li, Differences in optical properties between healthy and pathological human colon tissues using a Ti:sapphire laser: an *in vitro* study using the Monte Carlo inversion technique, *J. Biomed. Opt.*, 10(4), 044022;1–8, 2005.
14. M. Meinke, G. Müller, J. Helfmann, and M. Friebel, Optical properties of platelets and blood plasma and their influence on the optical behavior of whole blood in the visible to near infrared wavelength range, *J. Biomed. Opt.*, 12(1), 014024;1–9, 2007.
15. M. Friebel, A. Roggan, G. Müller, and M. Meinke, Determination of optical properties of human blood in the spectral range 250 to 1100 nm using Monte Carlo simulations with hematocrit-dependent effective scattering phase functions, *J. Biomed. Opt.*, 11(3), 034021; 1–10, 2006.
16. E. Salomatina, B. Jiang, J. Novak, and A. N. Yaroslavsky, Optical properties of normal and cancerous human skin in the visible and near-infrared spectral range, *J. Biomed. Opt.*, 11(6), 064026;1–9, 2006.
17. Meiji Seika Pharma Co., LTD., http://www.meiji-seika-pharma.co.jp/
18. JENOPTIK unique-mode GmbH, http://www.photonicsonline.com/storefronts/uniquemode.html/
19. V. V. Tuchin, Optical Properties of Tissues with Strong (Multiple) Scattering, Chap. 1 in *Tissue Optics*, 3–17, SPIE Press, Bellingham, 2007.
20. L.-H. V. Wang, and H. Wu, Scattering and its biological origins, Chap. 1 in *Biomedical Optics: Principles and Imaging*, 1–16, Wiley, Hoboken, NJ , 2007.
21. F. P. Bolin, L. E. Preuss, R. C. Taylor, and R. J. Ference, Refractive index of some mammalian tissues using a fiber optic cladding method, *Appl. Opt.*, 28(12), 2297–2303, 1989.

22. Oregon Medical Laser Center at Providence St. Vincent Medical Center: http://omlc.ogi.edu/spectra/hemoglobin/index.html.
23. J. S. Nelson, L.-H. Liaw, A. Orenstein, W. G. Roberts, and M. W. Berns, Mechanism of tumor destruction following photodynamic therapy with hematoporphyrin derivative, chlorin, and phthalocyanine, *J. Natl. Cancer Inst.*, 80(20), 1599–1605, 1988.
24. H. Joshima, M. Kashima, and O. Matsuoka, Diminished osmotic fragility of mouse erythrocytes following intravenous injection of polymeric plutonium, *J. Radiat. Res. (Tokyo)*, 25(4), 290–295, 1984.
25. X. Xu, R. K. Wang, J. B. Elder, and V. V. Tuchin, Effect of dextran-induced changes in refractive index and aggregation of optical properties of whole blood, *Phys. Med. Biol.*, 48, 1205–1221, 2003.
26. K. F. M. Fan, C. Hopper, P. M. Speight, G. A. Buonaccorsi, and S. G. Bown, Photodynamic therapy using mTHPC for malignant disease in the oral cavity, *Int. J. Cancer*, 73(1), 25–32, 1997.
27. I. S. Saidi, S. L. Jacques, and F. K. Tittel, Mie and Rayleigh modeling of visible-light scattering in neonatal skin, *Appl. Opt.*, 34(31), 7410–7418, 1995.
28. R. Splinter and B. A. Hooper, Light-tissue interaction variables, Chap. 5 in *An Introduction to Biomedical Optics*, 121–154, Taylor & Francis Group, New York, 2007.
29. P. R. Bargo, S. A. Prahl, T. T. Goodell, R. A. Sleven, G. Koval, G. Blair, and S. L. Jacques, *In vivo* determination of optical properties of normal and tumor tissue with white light reflectance and an empirical light transport model during endoscopy, *J. Biomed. Opt.*, 10(3), 034018;1–13, 2005.
30. J. Swartling, J. Axelsson, G. Ahlgren, K. M. Kälkner, S. Nilsson, S. Svanberg, K. Svanberg, and S. Andersson-Engels, System for interstitial photodynamic therapy with online dosimetry: first clinical experience of prostate cancer, *J. Biomed. Opt.*, 15(5), 058003;1–9, 2010.
31. M. S. Thompson, A. Johansson, T. Johansson, S. Andersson-Engels, S. Svanberg, N. Bendsoe, and K. Svanberg, Clinical system for interstitial photodynamic therapy with combined on-line dosimetry measurements, *Appl. Opt.*, 44(19), 4023–4031, 2005.
32. C. Fritsch, G. Goerz, and T. Ruzicka, Photodynamic therapy in dermatology, *Arch. Dermatol.*, 134, 207–214, 1998.

Figures

Table 4.1 Experimental conditions of PDT

Photosensitizer	Talaporfin sodium (Laserphyrin®, MEIJI SEIKA Pharma, Japan)		
Injected dose	5 [mg/kg]		
Laser	UM1000 Dental_665 (uniQue m.o.d.e, Germany)		
Wavelength	664 [nm]		
Energy density	100 [mW/cm^2]		
Irradiation condtion①	1, 5, 10 [min]		(Evaluation of optical property during PDT)
Irradiation condtion②	100 [J/cm^2]	(16 min 40 sec)	(Evaluation of optical property 1, 2, 7 days after PDT)

Table 4.2 Tumor tissue optical properties during and after PDT

Wavelength [nm]	Post-treatment [days]	μ_a [mm^{-1}] Mean±S. D.	μ_s' [mm^{-1}] Mean±S. D.
632	Before PDT	0.19±0.01	0.69±0.03
	1	0.22±0.04	0.85±0.07
	2	0.32±0.04	0.92±0.05
	7	0.35	1.30
664	Before PDT	0.17±0.01	0.64±0.02
	1	0.19±0.02	0.80±0.07
	2	0.26±0.04	0.90±0.08
	7	0.29	1.24
690	Before PDT	0.16±0.01	0.60±0.01
	1	0.16±0.01	0.76±0.07
	2	0.22±0.03	0.87±0.09
	7	0.25	1.18

Table 4.3 Optical penetration depth of tumor tissues during and after PDT.

Wavelength [nm]	Post-treatment [days]	Penetration depth [mm] Mean±S. D.
632	Before PDT	1.40±0.06
	1	1.20±0.14
	2	0.92±0.02
	7	0.76
664	Before PDT	1.54±0.05
	1	1.35±0.10
	2	1.05±0.05
	7	0.87
690	Before PDT	1.69±0.02
	1	1.49±0.09
	2	1.19±0.05
	7	0.97

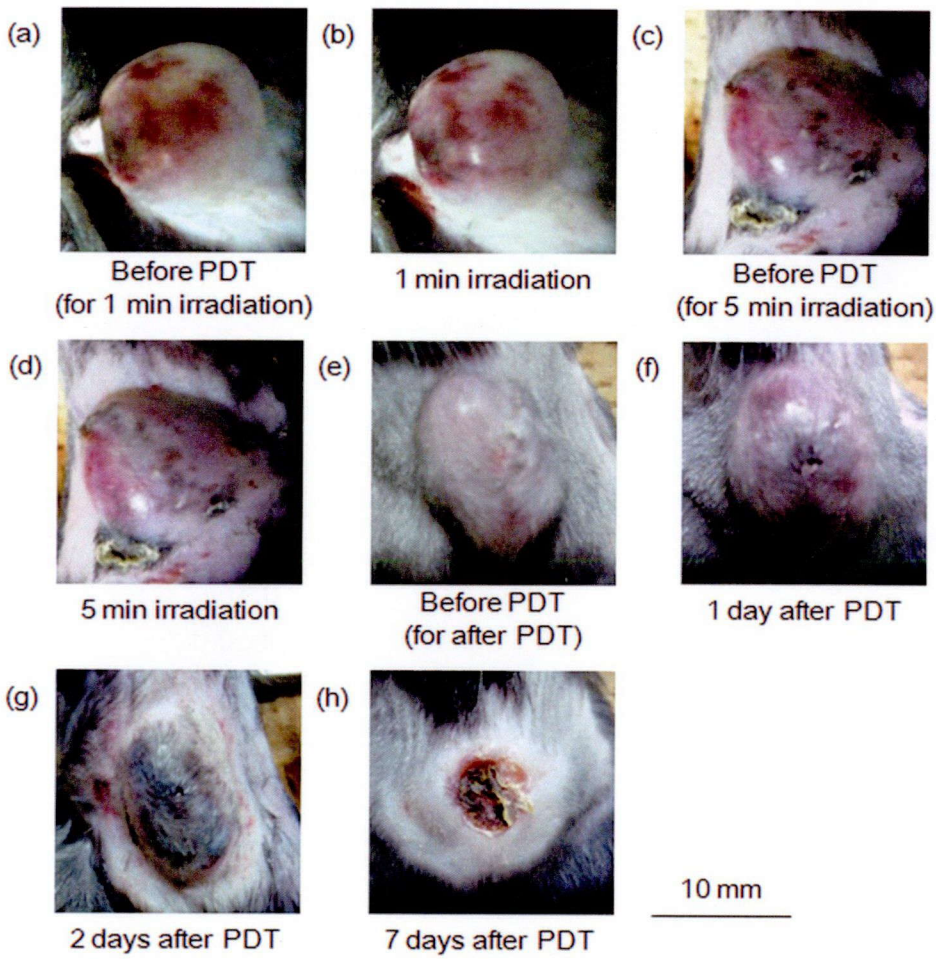

Figure 4.1 Photographs of tumor tissues during and after PDT. (a) Gross lesion of tissue before PDT. (b) Tumor tissue after irradiation of 100 mW/cm^2 for 1 min. (c) Gross lesion of untreated tissue. (d) PDT-treated tissue after completion of irradiation of 100 mW/cm^2 for 5 min. (e) Tumor tissue before PDT. (f) One day after PDT. Laser irradiation was performed with 100 mW/cm^2 for 1000 s. (g) Two days after PDT. Tumor was irradiated with 100 mW/cm^2 for 1000 s. (h) Seven days after PDT. Tumor was irradiated with 100 mW/cm^2 for 1000 s.

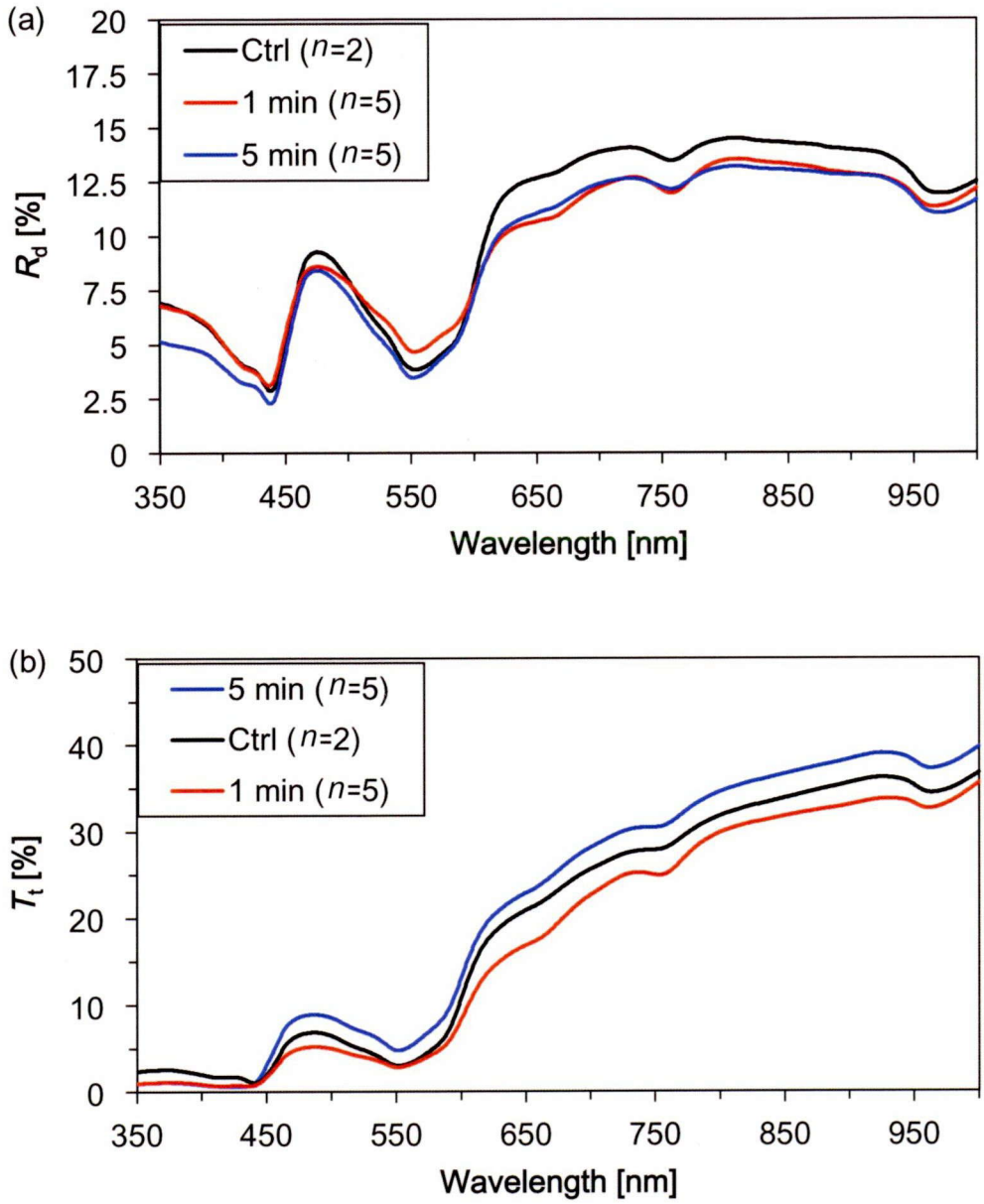

Figure 4.2 Diffuse reflectance R_d and transmittance T_t spectra of tumor tissues during PDT. (a) R_d spectra of tumor tissues performed 1 and 5 min irradiation. (b) T_t spectra of the tumor tissues.

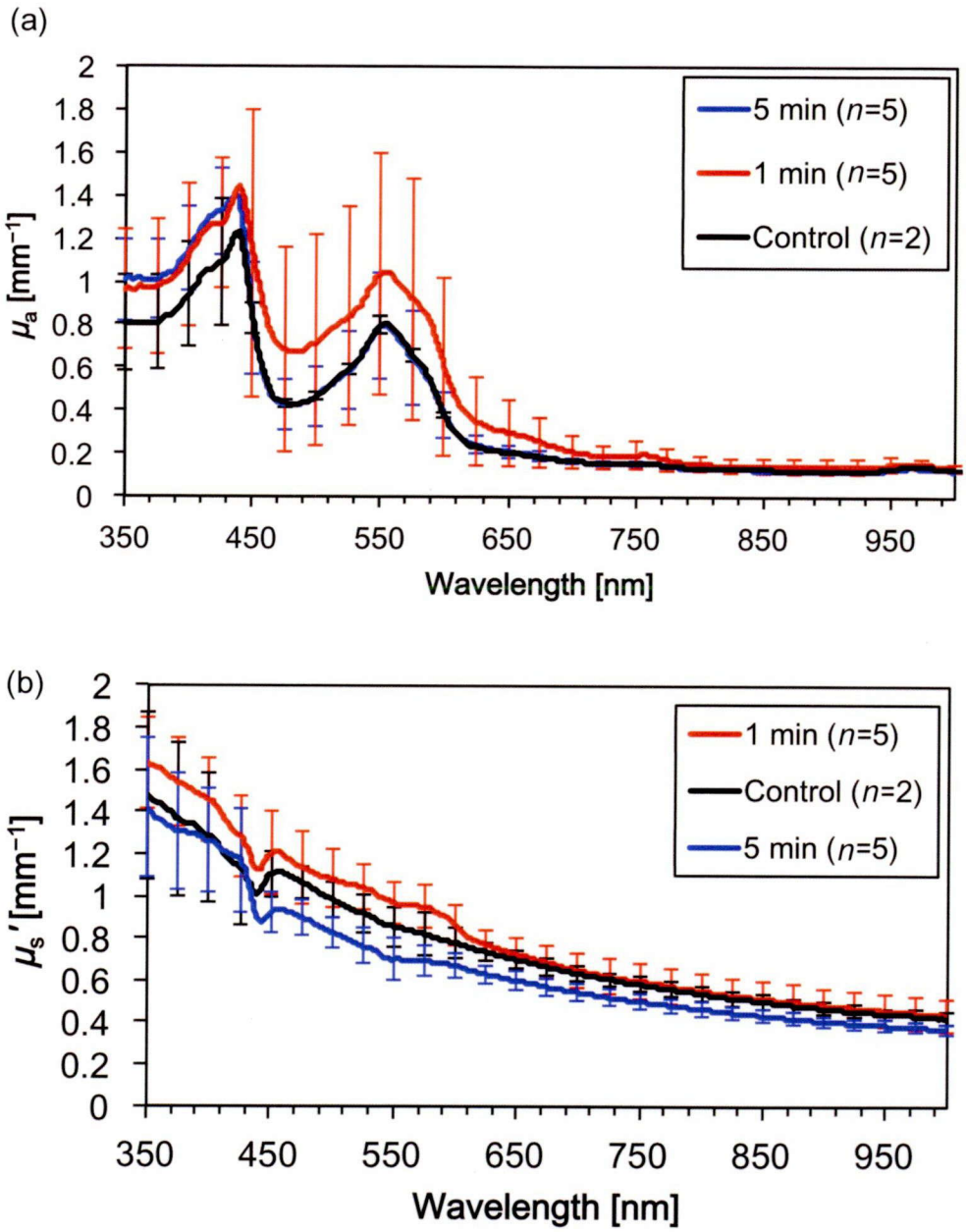

Figure 4.3 Absorption coefficient μ_a spectra and reduced scattering coefficient μ_s' spectra of tumor tissues during PDT. (a) μ_a spectra of tumor tissues performed 1 and 5 min irradiation. (b) μ_s' spectra of the tumor tissues.

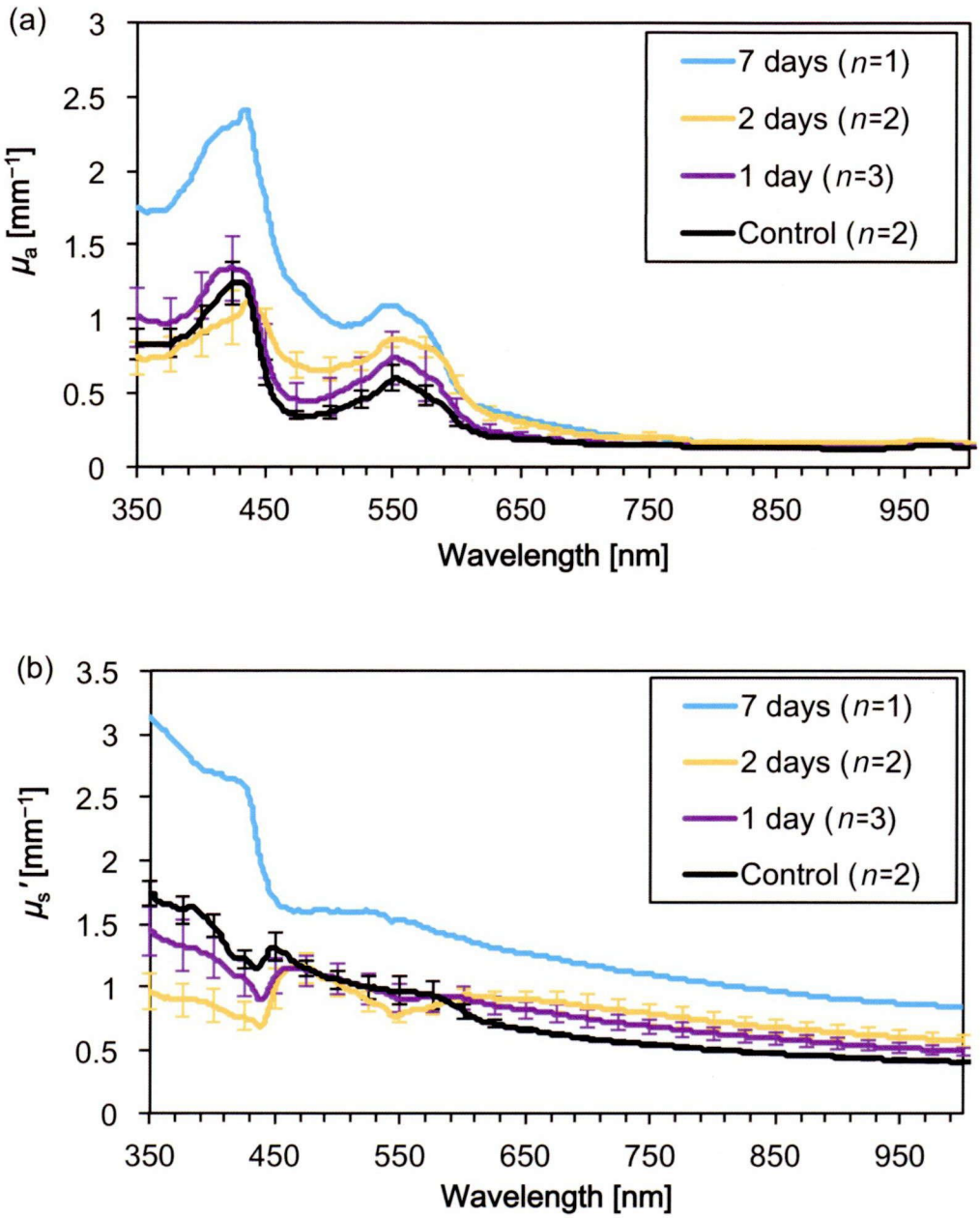

Figure 4.4 Absorption coefficient μ_a spectra and reduced scattering coefficient μ_s' spectra of tumor tissues after after 1, 2 and 7 days after PDT. (a) μ_a spectra of tumor tissues. (b) μ_s' spectra of the tumor tissues.

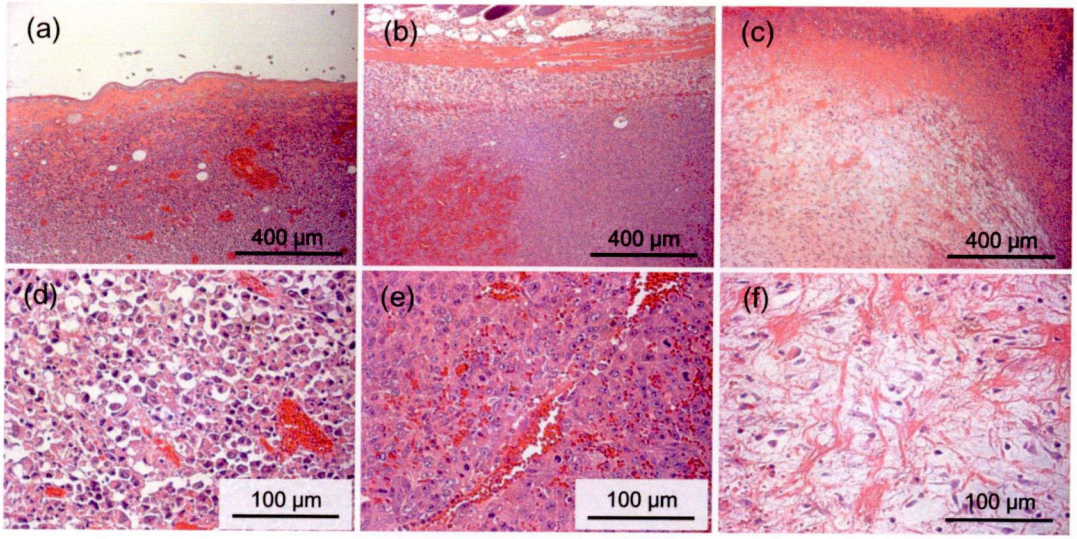

Figure 4.5 Hematoxylin and eosin staining images of tumor tissues. (a) and (d) show the Lewis lung carcinoma tissue before PDT. Tumor microvessels are shown. (b) and (e) show the tumor tissues 1 day after PDT. The blood vessel damage and leak of erythrocyte are shown after PDT. (c) and (f) show the PDT treated tumor tissue seven days after PDT. Decrease of tumor cells has been observed. The PDT treated tissue has shown fibrosis.

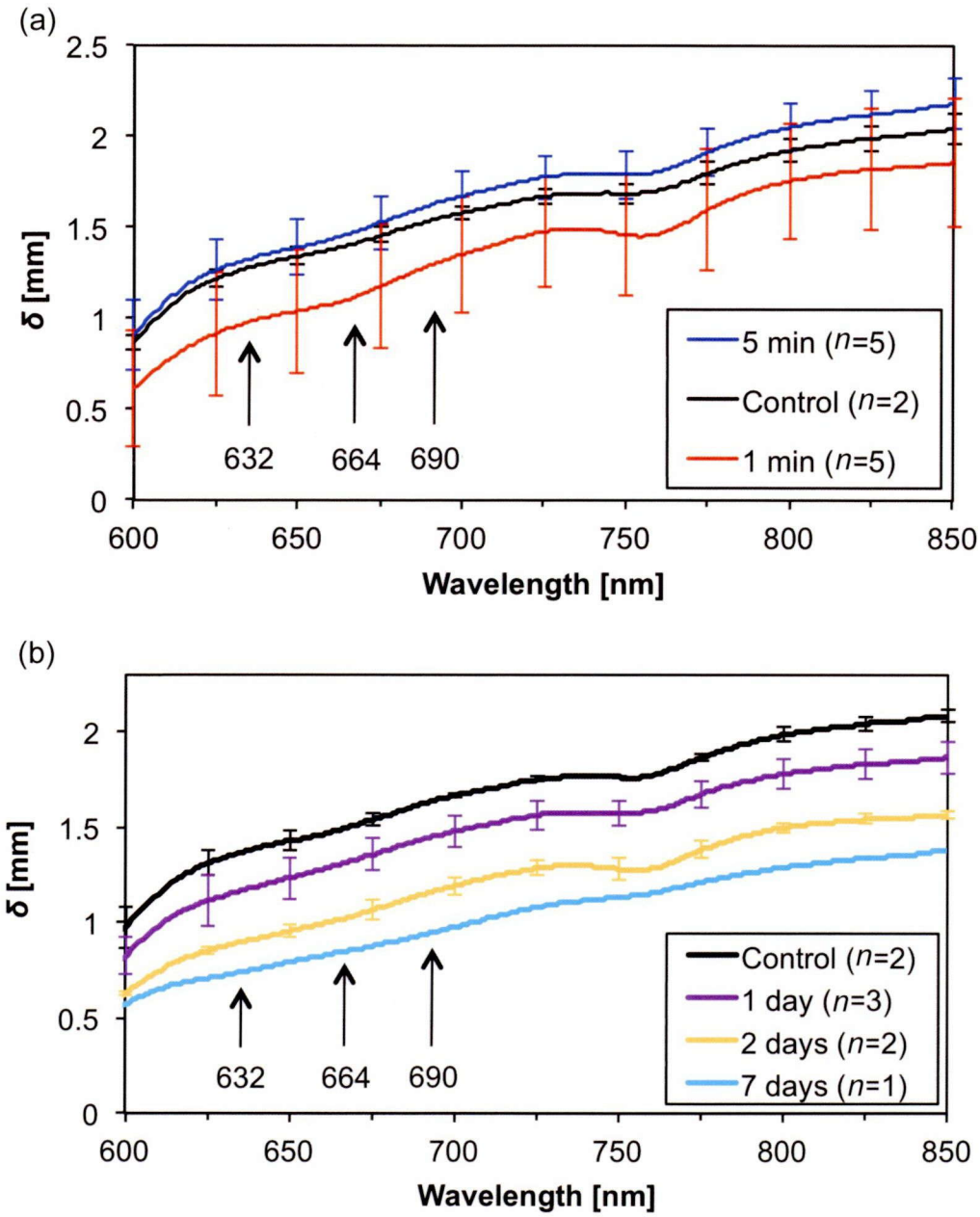

Figure 4.6 Optical penetration depths of PDT-treated tumor tissues. (a)The optical penetration depths of tumor tissues during PDT. (b) The optical penetration depths of tumor tissues after PDT.

Chapter 5

Determination of Optical Properties of Japanese Human Skin

5.1 Introduction

Laser hair removal is performed in dermatology and plastic surgery. Laser assisted hair removal uses the principle of selective photothermolysis[1], which depends on the absorption of the laser energy by the melanin pigment within the hair follicle and the stem cells near hair bulge. Melanin can be targeted by ruby, alexandrite, diode, and Nd:YAG lasers; more recently, intense pulsed light is used[2]. However, the use of these devices for hair removal is associated with pain and side effects, especially when treating dark or tanned skin, including Asian skin[3–5]. Due to increased epidermal melanin content in individuals with dark skin, there is a higher risk of thermal damage to the skin.

An understanding of hair anatomy, growth and physiology, together with a thorough understanding of laser-tissue interaction, in particular within the context of choosing optimal laser parameters for effective laser hair removal, should be acquired before using lasers for hair removal. It is necessary to understand the principles of biological tissue optics, light delivery into the tissue, the resultant heat production, the heat distribution, and the thermal damage to optimize the hair-removal process[6–8].

The knowledge of tissue optical properties is essential for mathematical analysis of light propagation in the skin to propose the optimal laser treatment parameters. Many authors have studied optical properties of the skin tissue[1,9–12]. However, to my knowledge, there are a few articles about the optical properties in the normal Japanese skin tissue.

This study aims to investigate the effect of 755 nm Alexandrite hair-removal lasers on the patterns of heat distribution and thermal damage in the skin tissue with the skin tissue optical properties and a simulation. I hope that this study's results offer dermatologists and plastic surgeons a better understanding of how any changes in the skin types can cause thermal damage to skin.

5.2 Materials and methods

5.2.1 Materials

Optical properties measurements have been carried out *in vitro* with skin samples obtained from fresh tissue samples taken from patients during planned surgery as shown in Figure 5.1. Table 5.1 is a summary of the skin tissue demographics. The samples were obtained from

International Goodwill Hospital (Yokohama, Japan) with prior patient consent. The tissue samples were wrapped in saline soaked gauze, transported to Osaka University and measured within 36 h of excision. For the measurements, the subcutaneous fat was removed using surgical scissors. The thickness of the layer with epidermis and dermis of the samples ranged from 1 to 2 mm. The lateral size of the sectioned tissues was in the 6 to 19 mm range. The sample was placed between two glass plates.

5.2.2 Optical properties measurement

The optical properties of the tissue are measured by the way described in Chapter 2. In the double integrating sphere apparatus, the entrance port size of the reflectance sphere was 10.0 mm in diameter, and the sample port of both spheres was 5.0 mm in diameter. The inverse MC technique was employed to calculate the optical properties of samples from measured value of R_d and T_t described earlier[13]. A MC simulations used in this study was developed by Wang *et al.*[14] In these calculations, g was fixed at 0.8[15]. The refractive index n of the sample was fixed to be 1.4 (Ref. 16,17). From diffusion theory[18], the optical penetration depth δ was calculated.

5.2.3 Calculation of light distribution

To calculate the distribution of absorbed light in the skin tissue, a mathematical model consisted of a MC algorithm developed by Wang *et al.*[14] was used. The skin tissue is modeled by forming uniform planar layers defined by factors such as thickness, optical properties, and thermal properties. I assumed that the skin surface was smooth and has a semi-infinite one-layer geometry to simulate the skin, which is 6.0 mm thick. The internal fluence is calculated using MC simulation[14] for 1 million photon packets. I assumed that the laser-beam energy was incident perpendicularly to the skin surface. MC simulation calculates the fluence in all the voxels during laser irradiation. The grid line separation and number of grid elements in the depth z direction are 0.01 cm and 60, respectively. The grid line separation and number of grid elements in the lateral distance x with the origin at the beam center are 0.01 cm and 300, respectively.

5.2.4 Calculation of the heat transfer

The heat deposition is individually calculated for each voxel after each time interval, considering a single-layer rectangle with edges, which runs parallel with the x and z, coordinate directions, respectively. Initially (time t = 0 s) the two-dimensional isotropic

composite slab is at a specified temperature. Then, for $t > 0$, I assumed the start of the laser energy deposition. After the calculation of the fluence during laser irradiation, the temperature rise due to laser absorption in target tissue is calculated by the next equation:

$$\Delta T(x,z,t) = \mu_a F(x,z,t)\, t \frac{1}{\rho C} \tag{5.1}$$

where $T(x, z, t)$ is the skin temperature [°C], and $F(x, z, t)$ is fluence rate [W/cm^2]. A constant initial skin temperature of 34°C was used for the entire tissue volume. The thermo-physical properties of skin[19] used in this study were density ρ = 1020 kg/m^3, specific heat capacity C = 3450 J kg^{-1} K^{-1}, thermal conductivity k = 0.501 W m^{-1} K^{-1}, and the heat transfer coefficient[20] between the skin surface and the above medium h = 4000 W m^{-2} K^{-1}. I use the Crank-Nicolson finite difference method to solve the two-dimensional transient form of the heat-conduction equation in the following format:

$$\frac{k}{\rho C}\left\{\frac{\partial T^2(x,z,t)}{\partial^2 x} + \frac{\partial T^2(x,z,t)}{\partial^2 z}\right\} + \frac{S(x,z,t)}{\rho C} = \frac{\partial T(x,z,t)}{\partial t} \tag{5.2}$$

where $S(x, z, t)$ is the heat source term [W m^{-3}]. I did not account for the latent heat of water vaporization. Convection surface boundary condition was used for the solution of the bio-heat conduction model:

$$-k\frac{\partial T(x,z,t)}{\partial z}\bigg|_{z=0} = h(T_{\text{med}} - T(x,z,t)|_{z=0}) \tag{5.3}$$

where T_{med} is the temperature of the medium above the skin surface (°C). The validation of Eq. (5.2) is shown in appendix B.

5.2.5 Arrhenius damage integral

The Arrhenius rate process integral was used to quantify thermal damage. I use an index, Ω, to quantify the sensitivity of thermal damage and assume that the rate of change of Ω follows an Arrhenius relationship:

$$d\Omega/dt = Ae^{-\Delta E/RT} \tag{5.4}$$

where A [s^{-1}] and ΔE [J mol^{-1}] are constants, R is the universal gas constant (8.314 [J mol^{-1} K^{-1}]) and T [K] is absolute temperature. Total damage accumulated over a period t is obtained by an integrating equation (5.4). At any time during a model calculation, the relative concentration (i.e. the % probability) of damaged proteins can be predicted from[21]: 100× {1 – exp (−Ω)}. Arrhenius parameters corresponding to microvascular blood flow stasis in response to heat were derived from measurements of changes in blood flow when muscle

tissue was heated[22]. Arrhenius parameters for burns in skin tissue were measured by Pearce[21]. I assumed the empirical values of $A = 1.98\times10^{106}$ s^{-1}, and $\Delta E = 6.67\times10^{5}$ J/mol for when microvascular blood flow stasis occurs[22]. I assumed the two empirical values of $A = 8.82\times10^{94}$ s^{-1}, and $\Delta E = 6.028\times10^{5}$ J/mol, $T \leq 53$ °C; and $A = 1.297\times10^{31}$ s^{-1}, and $\Delta E = 2.04\times10^{5}$ J/mol, $T > 53$ °C for when burns in skin tissue occurs[21].

5.2.6 Laser systems

In this study, I estimated reported three reported laser settings. One laser setting consisted of a 755 nm, a 18 mm spot size, a fluence of 18 J/cm^2, and pulse durations of 3 ms with 30 ms cryogen spray cooling (tetrafluorethane). The time delay between the termination of the cryogen spurt and the onset of laser pulse was 30 ms (Ref. 23). The second setting consisted of a 755 nm, an 18 mm spot size, a fluence of 16 J/cm^2, and pulse durations of 3 ms with 60 ms cryogen spray cooling. The time delay between the termination of the cryogen spurt and the onset of laser pulse was 60 ms (Ref. 24). The third setting consisted of a 755 nm, an 12 mm spot size, a fluence of 16 J/cm^2, and pulse durations of 3 ms with 60 ms cryogen spray cooling. The time delay between the termination of the cryogen spurt and the onset of laser pulse was 60 ms (Ref. 24). I assumed that the heat flux of spray cooling was 20 W/cm^2 (Ref.25).

5.3 Results and Discussion

5.3.1 Optical properties of Japanese skin

The μ_a and μ_s' spectra of the skin tissues were presented in figure 5.2 and 5.3, respectively. The μa of the skin tissues increased with decreasing of the wavelength as shown in figure 5.2(a). The μ_a spectra were manifested by two pronounced peaks of hemoglobin around the wavelength of 410 nm and 550 nm. The average of the μa spectra of the Japanese skin tissue is higher in the wavelength range from 400 to 900 nm than the reported value of the Caucasian skin tissue[9] (figure 5.2(b)). The average of the μ_a spectra of the Japanese skin tissue are lower in the wavelength range from 650 to 900 nm than the reported value of the African skin tissue[9] (figure 5.2 (b)). The μ_a of the Japanese skin tissues in the wavelength range from 650 to 900 nm are between the μ_a of the African and the Caucasian.

As shown in figure 5.3 (a), the μ_s' spectra of skin tissues in the wavelength range from 400 to 1000 nm was greater at a shorter wavelength with a peak value of about 5.1 mm^{-1} at the wavelength of 400 nm and decreased with an increase in the wavelength. As shown in

figure 5.3, these groups of the μ_s' spectra are similar in magnitude and slope in the wavelength range from 400 to 1000 nm.

Calculation of the optical penetration depth has been performed with the absorption and the μ_s' values presented in figure 5.2 and 5.3, respectively, and the result is presented in figure 5.4. From figure 5.4 it is seen that, depending on the wavelength, the penetration depth varies considerably. Table 5.2 summarizes the δ of the Japanese skin tissues in a specific region from 400 to 1000 nm, which are frequently used in PDT and photothermal-treatment for the individual wavelengths, such as 405, 532, 595, 632, 755, 800 and 980 nm.

5.3.2 Validity of Japanese skin optical property

Interestingly, in agreement with these results, the μ_a of the Asian skin tissue is higher than those of Caucasians[9]. Darkly pigmented skin contains more melanin than lightly pigmented skin[26]. Anderson and Parrish[1] reported that the absorption of melanin increases steadily toward a shorter wavelength over the broad spectrum of 250 to 1200 nm. Therefore, the effect of melanin of the epidermis appeared in the μ_a spectrum, especially in measurements lower than 600 nm.

As shown in figure 5.2(a), the μ_s' spectra of skin tissue in the wavelength range from 400 to 1000 nm decreased with an increase in the wavelength. A comparison of the measured data with the μ_s' spectra of the skin tissue was presented by Bashkatov *et al.*[11] and Tseng *et al.*[9] as shown in figure 5.2(b). The figure also shows a good agreement between them, which means that the skin of these groups has a similar composition in terms of the average scatter size and density.

It is difficult to accurately estimate the experimental error in a study of this type in which many independent measurements are conducted. Experimental contributions to the error include the inaccuracy of the spectrometer, which I estimate to be 0.5% of the corresponding 100% value. This error becomes more prominent as the measured value of T_t becomes smaller, such as in the wavelength range from 350 to 437 nm. This may have introduced an error in the μ_s' spectra as shown in figure 5.3(a).

The δ of the Japanese skin tissues are presented in figure 5.4. Table 5.2 summarizes the δ of the skin tissues in a specific region for PDT and photothermal-treatment from 400 to 1000 nm for the individual wavelengths. The δ greatly decreased at shorter wavelengths. Since the optical penetration depth of the Japanese skin is wavelength-dependent, the fluence rate in the tissue will be deeply affected by wavelength.

5.3.3 Predicted thermal distributions and thermal affection

Figure 5.5 shows the calculated response of the skin temperature to a 755 nm treatment pulse (3 ms pulse duration, fluence of 18 J/cm^2) following cryogen spray cooling (30 ms spurt duration, 30 ms delay). As the laser irradiates the treatment area, the 18 J/cm^2 fluence heats a 0.25 mm deep layer to approximately 60, 52 and 45°C in African, Japanese and Caucasian skin, respectively (Figure 5.5(a), 5.5(b), and 5.5(c)). As a result, the probability of microvascular blood flow stasis of African skin, Japanese skin, and Caucasian skin are 100%, 7.2%, and 0.1%, respectively. And, the probability of burns of African skin, Japanese skin, and Caucasian skin are 10.6%, 0.2%, and 0.02%, respectively. The simulation results indicated that the probabilities of side effect of Japanese skin tissue by Alexandrite laser is higher than the Caucasian skin tissue.

5.3.4 Effect of laser settings

As shown in figure 5.6, the thermal distribution within the Japanese skin varied with the laser settings. Results in, the probabilities of burns of the skin by the first, second, and third settings were 0.2%, 0.04%, and 0.02%, respectively. When the spurt duration and delay time increased, the probability of burns decreased. When the laser diameter decreased, the probability of burns unchanged. The temperature increment in the deep part was confirmed as a result that beam diameter spread. These results indicate that it is useful to optimize the laser parameters by a simulation model using the optical properties of Japanese human skin tissue for the safety of treatment using a 755 nm hair-removal lasers.

5.3.5 Comparing simulation to clinical data

Similar clinical studies have confirmed such an outcome. The first settings in a 755 nm Alexandrite laser can be safely applied on patients with skin types I-III[23] to achieve complete and permanent hair reduction without the risk of adverse thermal damage. Simulation results as shown in figure 5.5 are consistent with the clinical experience demonstrating a high degree of safety in patients with white skin.

This study does suffer from some limitations: for example, I neglected blood perfusion in the skin because of the short time scales (hundreds of milliseconds). I measured the optical properties of lightly pigmented skin in Japanese tissue, but in fact it differs according to the melanin in the skin. In reality, skin color in Japanese tissue may be widely different from patient to patient. It is certainly necessary to simulate the heat distribution and thermal damage of a group for various skin colors in Japanese people.

5.4 Conclusions

The optical properties of the typical Japanese skin consisting of epidermis and dermis for 5 objects were estimated with the double integrating sphere and inverse MC techniques. The μ_s' spectra of the Japanese, Caucasian[9,11] and African[11] skin tissues are very similar. According to simulation results, it seems that when the spurt duration and delay time increased, the probability of burns decreased. The temperature increment in the deep part was confirmed as a result that beam diameter spread. These results indicate that it is useful to optimize the laser parameters by a simulation model using the optical properties of Japanese human skin tissue. This mathematical model should serve as a useful tool to estimate the safety of the laser hair removal in Japanese skin. The results presented could be useful for evaluation of light distribution in the organ under examination or treatment, e.g., PDT, photothermal-treatment, etc., and for the development of optical techniques.

Reference

1. R. R. Anderson, and J. A. Parrish, The optics of human skin, *J. Invest. Dermatol.* 77, 13–19, 1981.
2. O. A. Ibrahimi, M. M. Avram, C. W. Hanke, S. L. Kilmer, and R. R. Anderson, Laser hair removal, *Dermatologic therapy*, 24, 94–107, 2011.
3. T. Omi, M. Honda, K. Yamamoto, M. Hata, M. Akimoto, G. Asano, and S. Kawana Histologic effects of ruby laser hair removal in Japanese patients, *Lasers Surg. Med.*, 25, 451–455, 1999.
4. M. Hussain, N. Polnikorn, and D. J. Goldberg, Laser-assisted hair removal in Asian skin: efficacy, complications, and the effect of single versus multiple treatments, *Dermatol. Surg.*, 29, 249–254, 2003.
5. C. K. Yeung, S. Y. Shek, and H. H. Chan, Hair removal with neodymium-doped yttrium aluminum garnet laser and pneumatic skin flattening in Asians, *Dermatol. Surg.*, 36, 1664–1670, 2010.
6. L. Ataie-Fashtami, A. Shirkavand, S. Sarkar, M. Alinaghizadeh, M. Hejazi, M. Fateh, G. E. Djavid, N. Zand, and H. Mohammadreza, Simulation of heat distribution and thermal damage patterns of diode hair-removal lasers: an applicable method for optimizing treatment parameters, *Photomed. Laser Surg.*, 29, 509–515, 2012.
7. B. Anvari, B. S. Tanenbaum, T. E. Milner, S. Kimel, L. O. Svaasand, and J. S. Nelson, A theoretical study of the thermal response of skin to cryogen spray cooling and pulsed

laser irradiation: implications for treatment of port wine stain birthmarks, *Phys. Med. Biol.*, 40, 1451–1465, 1996.

8. T. Dai, B. M. Pikkula, L. V. Wang, and B. Anvari, Comparison of human skin opto-thermal response to near-infrared and visible laser irradiations: a theoretical investigation, *Phys. Med. Biol.*, 49, 4861–4877, 2004.
9. S. H. Tseng, A. Grant, and A. J. Durkin, *In vivo* determination of skin near-infrared optical properties using diffuse optical spectroscopy, *J. Biomed. Opt.*, 13, 014016, 2008.
10. E. Salomatina, B. Jiang, J. Novak, and A. N. Yaroslavsky, Optical properties of normal and cancerous human skin in the visible and near-infrared spectral range, *J. Biomed. Opt.*, 11, 064026, 2006.
11. A. N. Bashkatov, E. A. Genina, V. I. Kochubey, and V. V. Tuchin, Optical properties of human skin, subcutaneous and mucous tissues in the wavelength range from 400 to 2000 nm, *J. Phys. D: Appl. Phys.*, 38, 2543–2555, 2005.
12. C. R. Simpson, M. Kohl, M. Essenpreis, and M. Cope, Near-infrared optical properties of ex vivo human skin and subcutaneous tissues measured using the Monte Carlo inversion technique, *Phys. Med. Biol.*, 43, 2465–2478, 1998.
13. N. Honda, K. Ishii, T. Nanjo, and K. Awazu, Development of the tissue optical properties measurement system with double integrating sphere and inverse Monte Carlo technique in the visible and near-infrared wavelength range, *The Journal of Japan Society for Laser Medicine*, 32, 421–428, 2012. (*in Japanese*).
14. L.-H. Wang, S. L. Jacques, and L. Q. Zheng, MCML - Monte Carlo modeling of light transport in multi-layered tissues, *Comput. Methods Programs Biomed.*, 47, 131–146, 1995.
15. S. L. Jacques, C. A. Alter, and S. A. Prahl, Angular dependence of He-Ne laser light scattering by human dermis, *Lasers Life Sci.*, 1, 309–334, 1987.
16. H. Ding, J. Q. Lu, W. A. Wooden, P. J. Kragel, and X. H. Hu, Refractive indices of human skin tissues at eight wavelengths and estimated dispersion relations between 300 and 1600 nm, *Phys. Med. Biol.*, 51, 1479–1489, 2006.
17. G. J. Tearney, M. E. Brezinski, J. F. Southern, B. E. Bouma, M. R. Hee, and J. G. Fujimoto, Determination of the refractive index of highly scattering human tissue by optical coherence tomography, *Opt. Lett.*, 20, 2258–2260, 1995.
18. F. Martelli, S. D. Bianco, A. Ismaelli, and G. Zaccanti (eds.), Solutions of the diffusion equation for homogenous media, in: Light Propagation through Biological Tissue and other Diffusive Media. Washington: SPIE Press, 57–92, 2010.

19. B. Choi, and A. J. Welch, Analysis of thermal relaxation during laser irradiation of tissue. *Lasers Surg. Med.*, 29, 351–359, 2001.
20. J. W. Tunnell, L. V. Wang, and B. Anvari, Optimum pulse duration and radiant exposure for vascular laser therapy of dark port-wine skin: a theoretical study, *Appl. Opt.* 42, 1367–1378, 2003.
21. J. A. Pearce, Relationship between Arrhenius models of thermal damage and the CEM 43 thermal dose. Proceedings of SPIE. 7181, 718104, 2009.
22. S. L. Brown, J. W. Hunt, and R. P. Hill, Differential thermal sensitivity of tumour and normal tissue microvascular response during hyperthermia, *Int. J. Hyperthermia.*, 8, 501–514, 1992.
23. S. P. Amin, and D. J. Goldberg, Clinical comparison of four hair removal lasers and light sources, *J. Cosmet. Laser Ther.*, 8, 65–68, 2006.
24. K. Nouri, H. Chen, S. Saghari, and C. A. Jr. Ricotti, Comparison 18- versus 12-mm spot size in hair removal using a gentlease 755-nm alexandrite laser, *Dermatol. Surg.*, 30, 494–497, 2004.
25. H. A. Waldorf, T. S. Alster, K. McMillan, A. N. Kauvar, R. G. Geronemus, and J. S. Nelson, Effect of dynamic cooling on 585-nm pulsed dye laser treatment of port-wine stain birthmarks, *Dermatol. Surg.*, 23, 657–662, 1997.
26. S. Alaluf, D. Atkins, K. Barrett, M. Blount, N. Carter, and A. Heath, Ethnic variation in melanin content and composition in photoexposed and photoprotected human skin, *Pigment Cell Res.*, 15, 112–118, 2002.

Figures

Table 5.1 Demographic summary of the skin samples.

Sample #	Age	Gender	Sample location
1	58	M	Back
2	49	F	Breast
3	67	M	Back
4	80	F	Breast
5	35	M	Right shoulder

Table 5.2 Optical properties of the typical Japanese skin tissues.

Wavelength [nm]	μ_a [mm^{-1}] Mean±S. D.	μ_s' [mm^{-1}] Mean±S. D.	δ [mm] Mean±S. D.
405	1.01±0.12	5.06±1.41	0.24±0.02
532	0.26±0.07	3.71±0.76	0.58±0.04
595	0.18±0.03	3.17±0.61	0.76±0.04
632	0.13±0.01	2.96±0.50	0.91±0.08
755	0.09±0.01	2.12±0.17	1.28±0.10
800	0.09±0.01	1.92±0.21	1.40±0.10
980	0.10±0.01	1.37±0.12	1.55±0.05

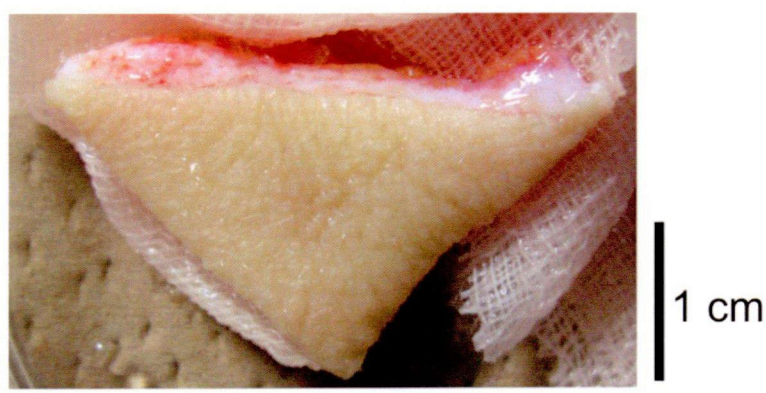

Figure 5.1 Photograph of the normal Japanese skin tissue.

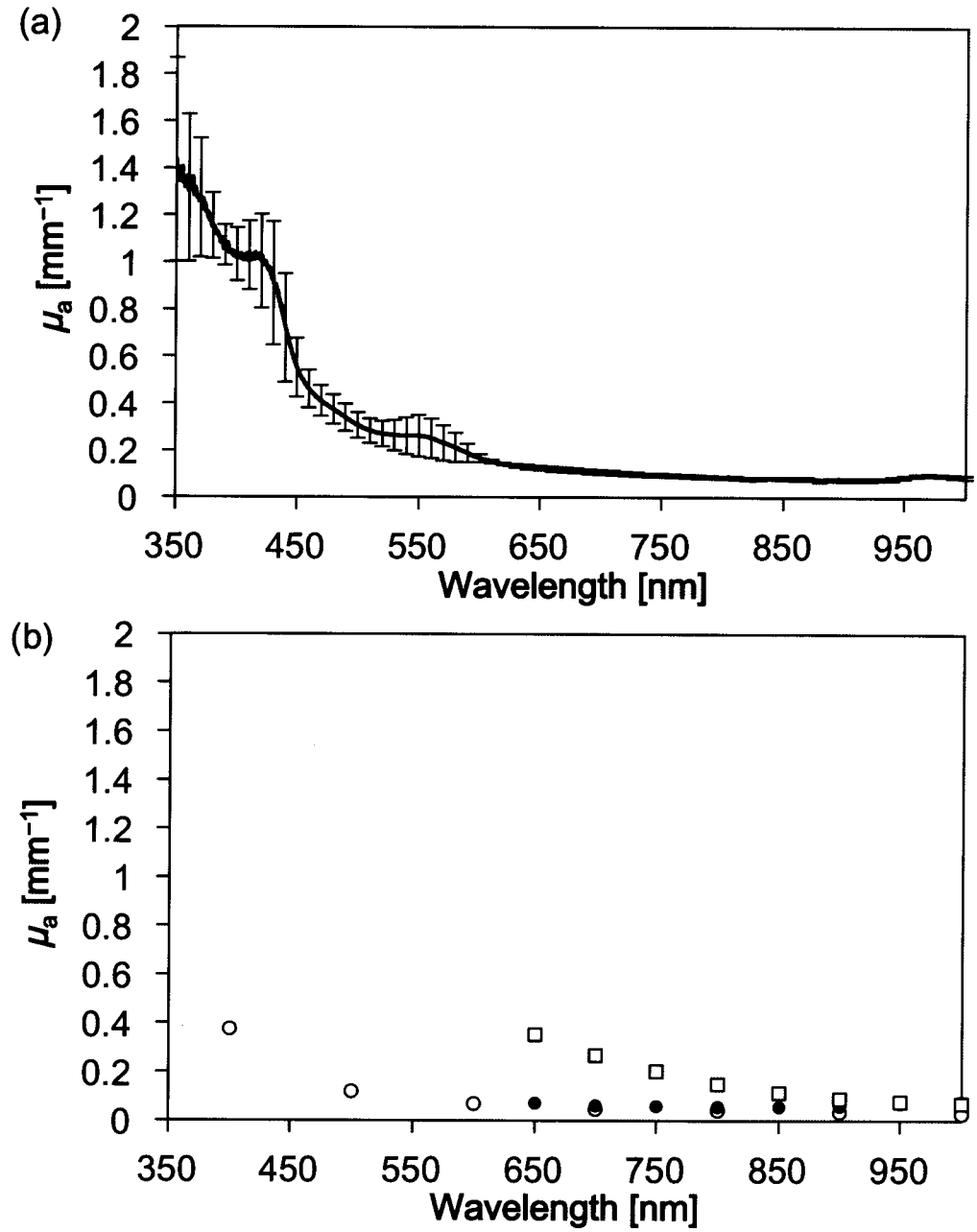

Figure 5.2 (a) Absorption coefficient μ_a spectra of the normal Japanese skin tissues. The lines and error bars represent the average and standard deviation of over five samples, respectively. (b) The symbols correspond to the experimental data presented in Ref. 9 and 11. The open circles correspond to the Caucasian skin data of Ref. 11, the circles correspond to the Caucasian skin data from graphs of Ref. 9, and the open squares correspond to the African skin data from graphs of Ref. 9.

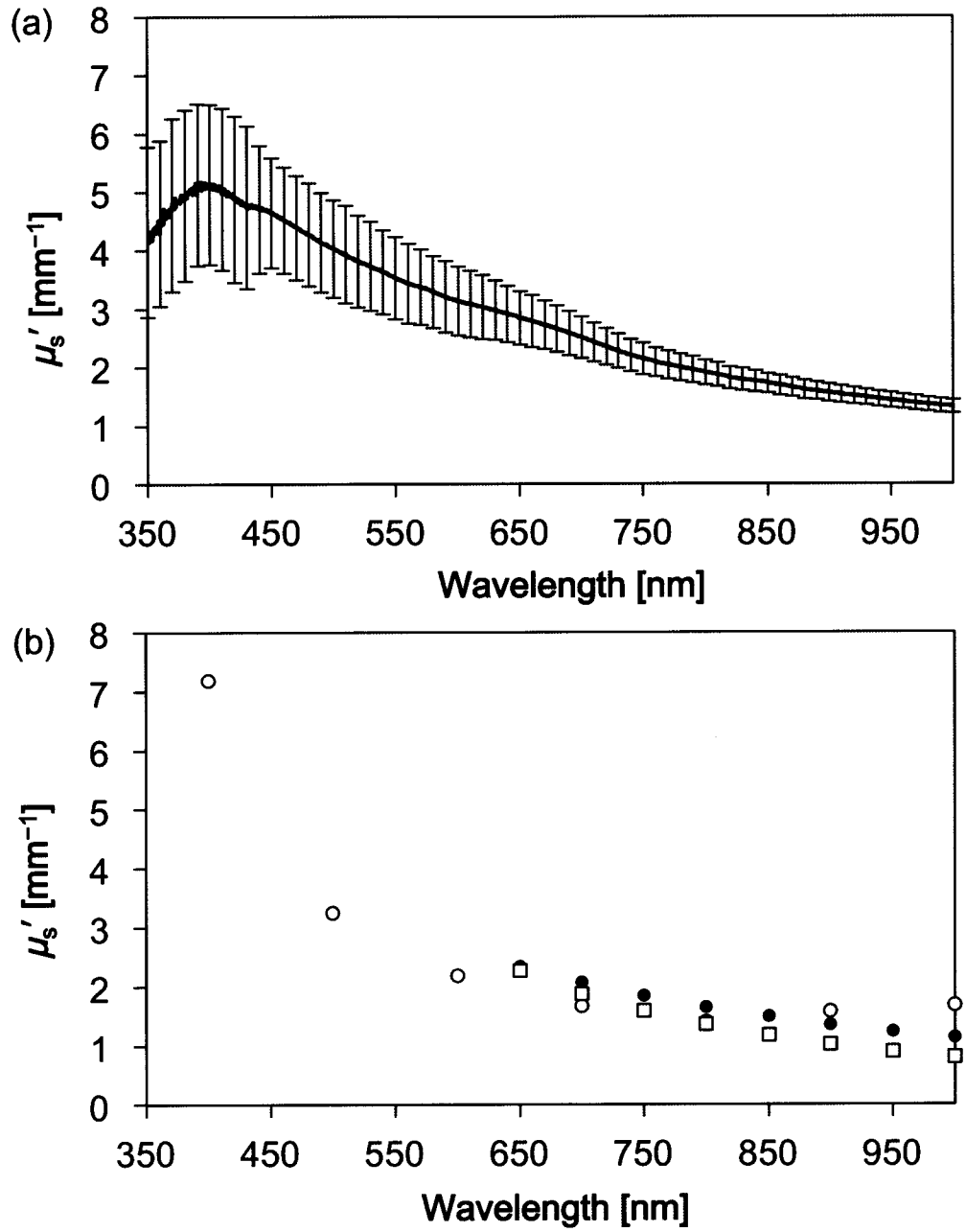

Figure 5.3 (a) Reduced scattering coefficient μ_s' spectra of the normal Japanese skin tissues. The lines and error bars represent the average and standard deviation of over five samples, respectively. (b) The symbols correspond to the experimental data presented in the spectra[9,11]. The open circles correspond to the Caucasian skin data[11], the circles correspond to the Caucasian skin data from graphs[9], and the open squares correspond to the African skin data from graphs[9].

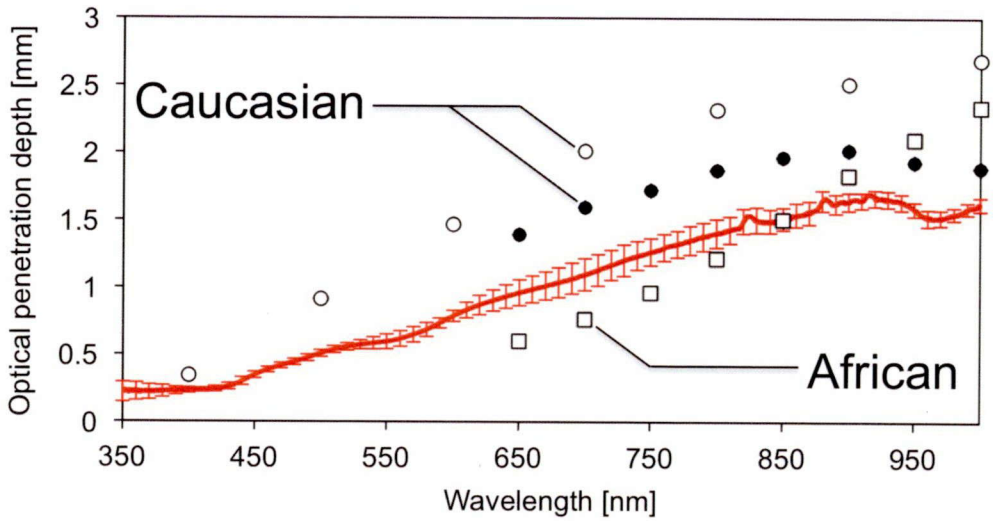

Figure 5.4 Optical penetration depth δ spectra of the normal Japanese skin tissues. The lines and error bars represent the average and standard deviation of over five samples, respectively. The symbols correspond to the experimental data presented in Ref. 11 and 9. The open circles correspond to the Caucasian skin data of Ref. 11, the circles correspond to the Caucasian skin data from graphs of Ref. 9, and the open squares correspond to the African skin data from graphs of Ref. 9.

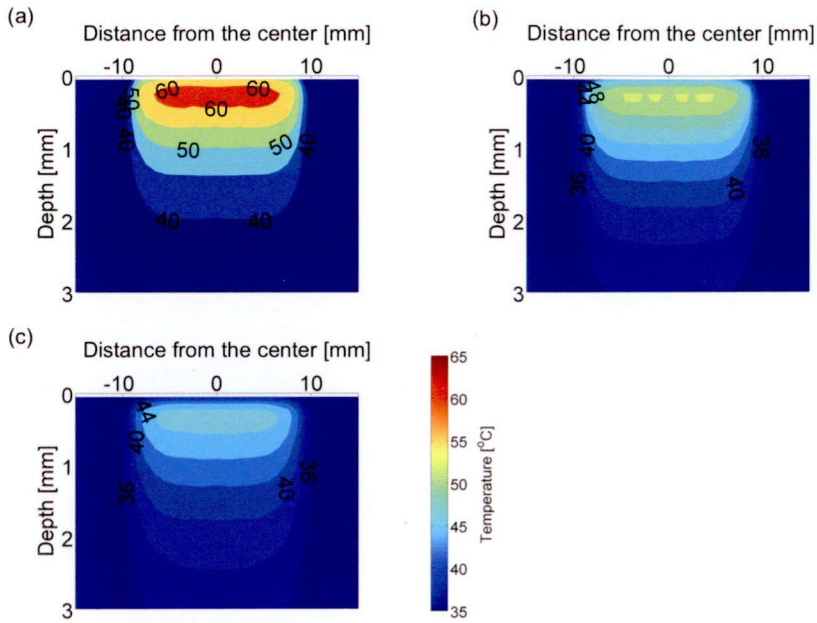

Figure 5.5 Skin temperature response of African skin (a), Japanese skin (b), and Caucasian (c) skin at the end of 755 nm laser pulse irradiation with pulse duration 3 ms, fluence 18 J/cm^2, spot sizes 18 mm.

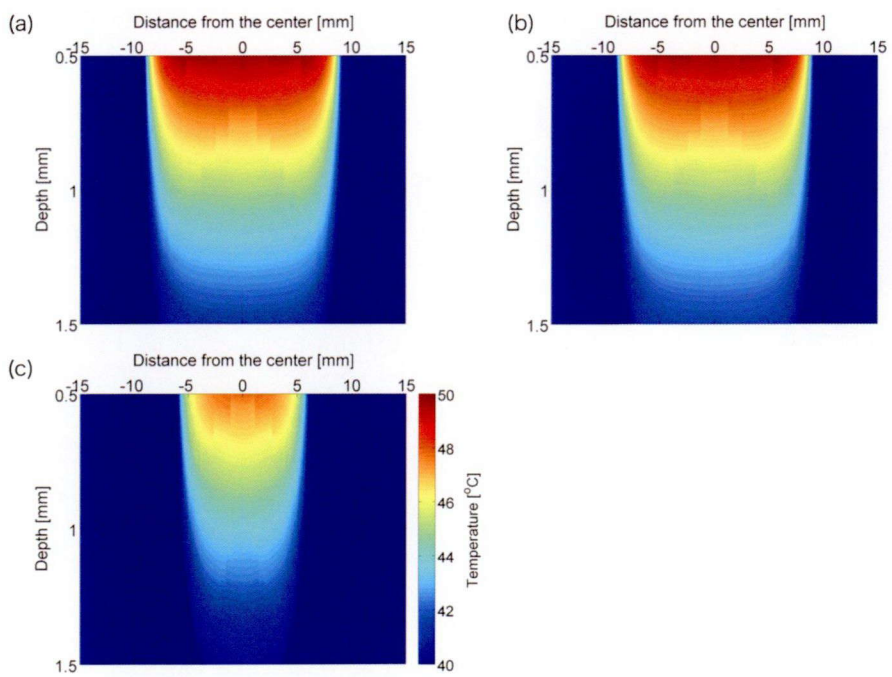

Figure 5.6 Skin temperature response of Japanese skin at the end of 755 nm pulse laser irradiation. (a) with pulse duration 3 ms, fluence 18 J/cm^2, spot sizes 18 mm, 30 ms spurt duration, 30 ms delay. (b) with pulse duration 3 ms, fluence 16 J/cm^2, spot sizes 18 mm, 60 ms spurt duration, 60 ms delay. (c) with pulse duration 3 ms, fluence 16 J/cm^2, spot sizes 12 mm, 60 ms spurt duration, 60 ms delay.

Chapter 6
Summary

I developed the optial properties measurement system in the wavelength range of 350–2100 nm. This system could measure the optical properties with high accuracy. By using this system, the optical properties of the tissue after laser treatment, such as the laser coagulation, and PDT were measured. The optical properties of Japanese skin tissue were measured for estimation of the probabilities of the side effect in laser treatment of the skin.

In Chapter 1, the present state of the medial laser application and the needs for biological tissue optical properties were described.

In Chapter 2, the developed optical properties measurement system by using the double integrating sphere and the inverse MC technique in the wavelength range of 350–2100 nm were described. By validation of the optical properties measurement system, the system allowed the measurement of the μ_a and the μ_s' of the turbid media with high accuracy and precision.

In Chapter 3, the optical properties of the tissue coagulated by the CO_2 laser were measured. The μ_s' in the wide wavelength range was increased after laser coagulation, and results in the δ decreased. Especially, the optical penetration depth of the coagulated tissue was 2 times lower than the optical penetration depth of native state tissue. For realization of the effective laser coagulation therapy, the consideration of the kinetic change of light energy distribution during laser irradiation is important.

In Chapter 4, the optical properties of the tumor tissue after PDT were measured. After PDT, the μ_s' increased with the passage of time. The tumor tissue morphological change by PDT might cause the change of optical properties. Seven days after PDT, the δ of the tumor tissue was a half of the native state of the tumor tissue. Conduction of re-PDT is considered for reduction of the tumor tissue volume. For the effective re-PDT, the consideration of the change of the δ after the first PDT is needed.

In Chapter 5, the optical properties of the Japanese skin consisting of epidermis and dermis were estimated. The μ_s' spectra of the Japanese, Caucasian and African skin tissues are very similar. However, the μ_a spectra of these tissues were different. It seems that when the spurt duration and delay time increased, the probability of burns decreased. The temperature increment in the deep part was confirmed as a result that beam diameter spread.

These results indicate that it is useful to optimize the laser parameters by a simulation model using the optical properties of Japanese human skin tissue.

The results could be useful for evaluation of light distribution in the organ under examination or treatment, e.g., PDT, photothermal-treatment, etc., and for the development of optical techniques. These results indicate that the measured optical properties of the biological tissues are important *in vivo*, and which provides the optimal laser irradiation parameters.

Acknowledgements

I would like to express my gratitude to Prof. Kunio Awazu who provided much perspective, encouraging, and an introduction to the art of absence of intelligence; to Prof. Shigehiro Nishijima for mentoring my development in scientific research and for giving the incisive comments; to Prof. Takayoshi Norimatsu for providing a kindness and a careful advice about my doctor thesis; to Dr. Katsunori Ishii who taught me the rudiments of the research from my master course; to Dr. Hisanao Hazama who always showed me the answer sometimes kindly, and sometime strictly; to Dr. Toshihiro Kushibiki who taught me the biological experiments and encouraged; to Dr. Takaya Terada for having the insightful discussion; to Prof. Steven L. Jacques, Oregon Medical Laser Center, Oregon Health & Science University for providing the idea about optical properties measurement in Chapter 2 and encouraging; to Dr. Hiromichi Yamada, International Goodwill Hospital, who gave the opportunity to work with him, provided the human skin sample used in Chapter 5, and encouraged; to Prof. Miya Ishihara, National Defense Medical College for encouraging and discussion about research; to Prof. Masato Ohmi, Osaka University Graduate School of Medicine for always being very kind and for having the insightful discussion.

I give thanks to all the people with whom I have had the pleasure and pain of insightful discussions. I thank Dr. Sachiko Suzuki, Mrs. Takako Tajiri, Mrs. Yuki Nakata, Mr. Hisanori Matsuoka, Ms. Noriko Hattori, Mr. Akinori Kimura, Mr. Yutaka Tomioka, and Dr. Makoto Sakai who shared my early years. I am also thankful to other various students Mr. Takuya Nanjo, Mr. Yohei Kobayashi, Mr. Naohiro Fujimoto, Mr. Taisuke Ikawa, Mr. Hideki Tsukimoto, Mr. Keisuke Matsumoto, Ms. Saki Nozoe, Mr. Takuro Horibe, Mr. Yoicihiro Kariyama, Mr. Masaya Yamauchi, Mr. Junya Takada, Mr. Hiroki Kannen, and Mr. Keisuke Hashimura. I am thankful to Ms. Akiko Kitayabu for her encouragement. I must thank all the wonderful people to work with. I also thank Prof. Hiroshi Iseki and Mr. Yuki Kawase, the Tokyo Women's Medical University - Waseda University Joint Institution for Advanced Biomedical Sciences group for sharing great discussions over beer. Dr. Yoshinaga Kajimoto and Dr. Takashi Yoneda, the Osaka Medical College group. And hearty thanks goes to Ms. Masako Kudoh and Mrs. Yoko Miyazaki, who provided complete support on research and Awazu Laboratory life.

Finally, I would like to thank my family who allowed me to challenge to research. My parents, Minoru and Sayo give me a supportive push forward and I am very thankful to all they have given me.

January, 2013

Norihiro Honda

List of Publications

［学術論文］

（査読付）

1) Determination of the tumor tissue optical properties during and after photodynamic therapy using inverse Monte Carlo method and double integrating sphere between 350 nm and 1000 nm: Honda N., Ishii K., Terada T., Nanjo T., Awazu K., Journal of Biomedical Optics, vol. 16, no. 5, 058003, 2011

2)近赤外分光分析による微生物生成代謝物の推定に関する基礎的検討：本多 典広，長塩 尚之，吉岡 雅也，粟津 邦男，EICA，vol. 16, no. 2/3, pp. 38, 2011

3)双積分吸光学系と逆モンテカルロ法を用いた組織の可視・近赤外域光学特性値算出システムの開発とその評価：本多 典広，石井 克典，南條 卓也，粟津 邦男，日本レーザー医学会誌，vol.32, no. 4, pp. 421-428, 2012

4)動脈硬化病変ファントムの近赤外ハイパースペクトルイメージング：北籔 晃子，石井 克典，本多 典広，粟津 邦男，レーザー研究，vol. 40, no. 4, pp. 305-309，2012

5)下肢静脈瘤に対する血管内レーザー治療における波長 980 nm および 1470 nm レーザーの有効性および安全性の光学特性値に基づいた比較：野添紗希，本多 典広，石井 克典，粟津 邦男，日本レーザー医学会誌，Vol. 33, No. 1, pp. 7-14，2012

6) 光散乱を用いた微生物群の構成比のモニタリング：本多 典広，長塩 尚之，吉岡 雅也，粟津 邦男，EICA，vol. 17, no. 2/3, pp. 63, 2012

7)波長 350～1000 nm の光学特性に基づく椎間板ヘルニア髄核組織ファントムの開発：井上 惇，石井 克典，伊東 信久，本多 典広，寺田 隆哉，粟津 邦男，日本レーザー医学会誌，vol. 32, no. 4, pp. 375-381，2012

8)生体組織の散乱係数誤算出における Mie 散乱及び Rayleigh 散乱を用いた補正：南條 卓也，石井 克典，本多 典広，粟津 邦男，日本レーザー医学会誌，vol. 32, no. 4, pp. 429-436，2012

9)椎間板ヘルニア髄核組織の光学特性の算出と経皮的レーザー椎間板減圧術の最適波長に関する一考察：石井 克典，伊東 信久，井上 惇，本多 典広，寺田 隆哉，粟津 邦男，日本レーザー医学会誌，vol. 31, no. 2, pp. 152-157，2010

10) OCT を用いたレーザー凝固中における生体軟組織の光減衰係数の連続測定：大宮 孝太、石井 克典，本多 典広，近江 雅人，粟津 邦男，日本レーザー医学会誌，vol. 33, no. 3, pp. 298，2012

（査読無し）

1) Determination of optical property changes by laser treatments using inverse adding-doubling method: Honda N., Ishii K., Kimura A., Sakai M., Awazu K., Proceedings of SPIE, 7175: 71750Q, 2009

2) Determination of the optical property changes by photodynamic therapy using inverse Monte Carlo method between 350 nm and 1000 nm: Honda N., Terada T., Nanjo T., Ishii K., Awazu K., Proceedings of SPIE, 7562: 75620D, 2010

3) 双積分球光学系と inverse Monte Carlo 法を用いた生体組織の光学特性の算出：本多 典広，寺田 隆哉，南條 卓也，小林 洋平，石井 克典，粟津 邦男，電気学会研究会資料（光・量子デバイス研究会 バイオメディカルフォトニクス応用），OQD-10-024，pp. 25-30，2010

4) Optical properties measurement of laser coagulated tissues with double integrating sphere and inverse Monte Carlo technique in the wavelength range from 350 to 2100 nm: Honda N., Nanjo T., Ishii K., Awazu K., Proceedings of SPIE, 8221: 82211F, 2012

5) Optical properties measurement of the laser-ablated tissues for the combined laser ablation with photodynamic therapy: Honda N., Ishii K., Awazu K., Proceedings of SPIE, 8221: 82210F, 2012

6) Monitoring of tissue coagulation during laser therapy using aiming laser during photo therapy: Honda N., Nozoe S., Awazu K., Proceedings of Conference on Laser Surgery and Medicine 2012, CLSM5-1, 34-35, 2012

7) Wavelength dependency of endovenous laser ablation at 980 nm and 1470 nm based on tissue optics: Nozoe S., Honda N., Ishii K., Awazu K., Proceedings of Conference on Laser Surgery and Medicine 2012，CLSM4-2，2012

8) 生体組織の散乱係数誤算出における Mie 理論を用いた補正：南條 卓也，寺田 隆哉，本多 典広，石井 克典，粟津 邦男，電気学会研究会資料，OQD-11-034，2011

9) 下肢静脈瘤レーザー治療の効果-安全性向上に向けた至適照射条件の検討-：野添 紗希，本多 典広，石井 克典，粟津 邦男，電気学会研究会資料，OQD-11-030，2011

10) Quantitative analysis of endovenous laser ablation based on human vein optical properties: Nozoe, S., Honda, N., Ishii, K., Awazu K., Proceedings of SPIE, vol. 8092, 80921J, 2011

11) 近赤外ハイパースペクトルイメージングによる動脈硬化病変の検出：北籔 晃子，本多 典広，石井 克典，粟津 邦男，レーザー学会第 417 回研究会報告，RTM-11-23，2011

12) 生体組織の散乱係数誤算出における Mie 理論を用いた補正：南條 卓也，寺田 隆哉，本多 典広，石井 克典，粟津 邦男，電気学会研究会資料，OQD-11-034，2011

13) 双積分球光学系と inverse Monte Carlo 法を用いた光学特性算出における光学特性値誤算出に関する考察：寺田 隆哉，南條 卓也，本多 典広，石井 克典，粟津 邦男，電気学会研究会資料，OQD-11-011，2011

14) Error analysis of tissue optical properties determined by double-integrating sphere system and inverse Monte Carlo method: Terada T., Nanjo T., Honda N., Ishii K., Awazu K., Proceedings of SPIE, Vol. 7897, 78971W, 2011

15) Transillumination of subcutaneous adipose tissues using near-infrared hyperspectral imaging in the 1100-1800-nm wavelength range: Ishii K., Kitayabu A., Kobayashi Y., Honda N., Awazu K., Proceedings of SPIE, Vol. 7902, 79021X, 2011

［著書］

1) レーザー医療に向けた生体組織光学特性測：粟津 邦男，本多 典広，医学のあゆみ，医歯薬出版株式会社，vol. 240, no. 6, pp. 527-532, 2012

2)生体組織の光散乱：粟津 邦男，本多 典広，Steven L. Jacques，機能材料，シーエムシー出版，vol. 32, no. 5, pp. 55-59, 2012

3)光散乱の理論を用いた生体組織の光学特性値の算出：粟津 邦男，本多 典広，Steven L. Jacques，機能材料，シーエムシー出版，vol. 32, no. 6, pp. 54-59, 2012

4)生体組織内での光伝搬：粟津 邦男，Steven L. Jacques，本多 典広，間 久直，機能材料，シーエムシー出版，vol. 32, no. 10, pp. 62-66, 2012

5) フルエンス測定：粟津 邦男，Steven L. Jacques，本多 典広，間 久直，機能材料，シーエムシー出版，vol. 32, no. 11, pp. 60-64, 2012

6) フルエンスレートの理論的取り扱い：粟津 邦男，Steven L. Jacques，本多 典広，間 久直，機能材料，シーエムシー出版，vol. 32, no. 12, pp. 58-64, 2012

[その他]

総説 （査読付）

1) Inverse Monte Carlo 法による光線力学療法前後の腫瘍組織の光学特性の算出：本多 典広，寺田 隆哉，南條 卓也，石井 克典，粟津 邦男，日本レーザー医学会誌，vol. 31, no. 2，pp. 115-121，2010

解説 （査読無し）

1)レーザ医療における Tissue Optics の重要性–生体組織の吸収，および散乱による光の伝搬–：粟津 邦男，本多 典広，光アライアンス, vol. 24, no.3, pp. 6-11, 2013

学会抄録

(国際会議・口頭発表)

1) Determination of optical property changes by laser treatments using inverse adding-doubling method : Honda N., Ishii K., Kimura A., Sakai M., Awazu K., SPIE Photonics West BiOS 2009, 7175-24, San Jose, USA, (January 2009)

2) Determination of the optical property changes by photodynamic therapy using inverse Monte Carlo method between 350 nm and 1000 nm : Honda N., Terada T., Nanjo T., Ishii K., Awazu K., SPIE Photonics West BiOS 2010, 7562-13, San Francisco, USA, (January 2010)

3) Optical properties measurement of the laser-ablated tissues for the combined laser ablation with photodynamic therapy: Honda N., Ishii K., Awazu K., SPIE Photonics West BiOS 2012, 8221-15, San Francisco, USA, (January 2012)
4) Realtime coagulation monitoring using aiming laser during phototherapy: Awazu K., Honda N., American Society for Laser Medicine and Surgery, #132, Florida, USA, (April 2012)
5) Determination of the optical properties of the tissues treated by photodynamic therapy using Inverse Monte Carlo method between 350 nm and 1000 nm: Honda N., Terada T., Nanjo T., Ishii K., Awazu K., The 2nd Asia Japan-Korea-China PDT Symposium, AS-14, Fukui, Japan, (June 2010)
6) Optical properties of tumor tissues and their application for photodynamic diagnosis and therapy: Honda N., Ishii K., Awazu K., 2012 Optical Society of Korea, W2C-VI3, Korea, (August 2012)
7) Monitoring of tissue coagulation during laser therapy using aiming laser during photo therapy: Honda N., Nozoe S., Awazu K., Proceedings of Conference on Laser Surgery and Medicine 2012 (CLSM 2012), CLSM5-1, Japan, (April 2012)

(国際会議・ポスター)

1) Optical properties measurement of laser coagulated tissues with double integrating sphere and inverse Monte Carlo technique in the wavelength range from 350 to 2100 nm, Awazu K., Honda N., Nanjo T., Ishii K., SPIE Photonics West BiOS 2012, 8221-53, San Francisco, USA, (January 2012)

(国内学会・口頭発表)

1) マウス腫瘍組織の光学特性及び光線力学療法による変化：本多 典広，寺田 隆哉，南條 卓也，石井 克典，粟津 邦男，レーザー学会，4pIII 1，大阪，2010 年 2 月
2) レーザー治療最適化に向けた可視・近赤外域における組織光学特性算出システムの開発：本多 典広，石井 克典，粟津 邦男, I-4，大阪，2011 年 7 月
3) 波長 664 nm における光線力学的療法の再治療の際の腫瘍組織の光学特性に基づいた光ドジメトリー：本多 典広，石井 克典，粟津 邦男， S1-3，大阪，2011 年 7 月

4) 可視・近赤外波長域におけるレーザー凝固組織の光学特性値算出：本多 典広，堀部 拓郎，南條 卓也，石井 克典，粟津 邦男，01pVI-12，仙台，2012 年 1 月

5) 逆モンテカルロ法および双積分球光学系を用いた悪性脳腫瘍皮下移植モデルマウスの腫瘍組織の光学特性値算出：本多 典広，川瀬 悠樹，伊関 洋，粟津 邦男，第 22 回日本光線力学学会学術講演会，S1-1，茨城，2012 年 7 月

6) 波長 350～1000 nm での邦人皮膚組織の光侵達深さの算出：本多 典広，山田 裕道，粟津 邦男，第 33 回日本レーザー医学会総会，O2-1，大阪，2012 年 11 月

(国内学会・ポスター)

1) Inverse Monte Carlo 法による光線力学療法前後の腫瘍組織の光学特性の算出：本多 典広，寺田 隆哉，南條 卓也，石井 克典，粟津 邦男，日本レーザー医学会総会，P2-01，東京，2009 年 12 月

Appendix A

Source Code of the Program of Monte Carlo Simulation Assuming the Port Diameter of Integrating Sphere

The original MC code provided by Lihong Wang and Steven L. Jacques[1] is changed to take into account the exact geometrical configuration of port diameter of the integrating sphere. The file "mcml.h" is the header file, which defines data structures and some constants. The file "mcmlmain.c" contains the function main(). It also deals with the timings and status report. The file "mcmlio.c" reads or writes data from or to data files. The file "mcmlgo.c" does most of the MC simulations. The file "mcmlnr.c" (nr stands for numerical recipes) contains several functions for dynamical data allocations and error report. The program was built with Program C.

1 mcml.h

```
#include <math.h>
#include <stdlib.h>
#include <stdio.h>
#include <stddef.h>
#include <time.h>
#include <string.h>
#include <ctype.h>

#define PI 3.1415926
#define WEIGHT 1E-4                    /* Critical weight for roulette. */
#define CHANCE 0.1              /* Chance of roulette survival. */
#define STRLEN 256              /* String length. */

#define Boolean char

#define SIGN(x) ((x)>=0 ? 1:-1)

/****************** Stuctures *****************************/

/****
 *          Structure used to describe a photon packet.
 ****/
typedef struct {
 double x, y ,z;        /* Cartesian coordinates.[cm] */
 double ux, uy, uz;/* directional cosines of a photon. */
 double w;                      /* weight. */
 Boolean dead;                  /* 1 if photon is terminated. */
 short layer;                   /* index to layer where the photon */
                                                /* packet resides. */
 double s;                      /* current step size. [cm]. */
 double sleft;                  /* step size left. dimensionless [-]. */
} PhotonStruct;

/****
 *          Structure used to describe the geometry and optical
 *          properties of a layer.
 *          z0 and z1 are the z coordinates for the upper boundary
```

2 mcmlmain.c

```
/****
 *          THINKCPROFILER is defined to generate profiler calls in
 *          Think C. If 1, remember to turn on "Generate profiler
 *          calls" in the options menu.
 ****/
#define THINKCPROFILER 0

/* GNU cc does not support difftime() and CLOCKS_PER_SEC.*/
#define GNUCC 0

#if THINKCPROFILER
#include <profile.h>
#include <console.h>
#endif

#include "mcml.h"

/*          Declare before they are used in main(). */
FILE *GetFile(char *);
short ReadNumRuns(FILE* );
void ReadParm(FILE* , InputStruct * );
void CheckParm(FILE* , InputStruct * );
void InitOutputData(InputStruct, OutStruct *);
void FreeData(InputStruct, OutStruct *);
double Rspecular(LayerStruct * );
void LaunchPhoton(double, LayerStruct *, PhotonStruct *);
void HopDropSpin(InputStruct  *,PhotonStruct *,OutStruct *);
void SumScaleResult(InputStruct, OutStruct *);
void WriteResult(InputStruct, OutStruct, char *);


/************************************************************
 *          If F = 0, reset the clock and return 0.
 *
 *          If F = 1, pass the user time to Msg and print Msg on
 *          screen, return the real time since F=0.
 *
 *          If F = 2, same as F=1 except no printing.
 *
 *          Note that clock() and time() return user time and real
 *          time respectively.
 *          User time is whatever the system allocates to the
 *          running of the program;
 *          real time is wall-clock time.  In a time-shared system,
 *          they need not be the same.
 *
 *          clock() only hold 16 bit integer, which is about 32768
 *          clock ticks.
 ****/
time_t PunchTime(char F, char *Msg)
{
#if GNUCC
 return(0);
#else
 static clock_t ut0;    /* user time reference. */
 static time_t  rt0;    /* real time reference. */
 double secs;
 char s[STRLEN];

 if(F==0) {
  ut0 = clock();
  rt0 = time(NULL);
  return(0);
 }
 else if(F==1)  {
  secs = (clock() - ut0)/(double)CLOCKS_PER_SEC;
  if (secs<0) secs=0;  /* clock() can overflow. */
  sprintf(s, "User time: %8.0lf sec = %8.2lf hr.  %s\n",
             secs, secs/3600.0, Msg);
  puts(s);
  strcpy(Msg, s);
  return(difftime(time(NULL), rt0));
 }
 else if(F==2) return(difftime(time(NULL), rt0));
 else return(0);
```

```
#endif
}

/*************************************************************
 *          Print the current time and the estimated finishing time.
 *
 *          P1 is the number of computed photon packets.
 *          Pt is the total number of photon packets.
 ****/
void PredictDoneTime(long P1, long Pt)
{
 time_t now, done_time;
 struct tm *date;
 char s[80];

 now = time(NULL);
 date = localtime(&now);
 strftime(s, 80, "%H:%M %x", date);
 printf("Now %s, ", s);

 done_time = now +
                                (time_t) (PunchTime(2,"")/(double)P1*(Pt-P1));
 date = localtime(&done_time);
 strftime(s, 80, "%H:%M %x", date);
 printf("End %s\n", s);
}

/*************************************************************
 *          Report time and write results.
 ****/
void ReportResult(InputStruct In_Parm, OutStruct Out_Parm)
{
 char time_report[STRLEN];

 strcpy(time_report, " Simulation time of this run.");
 PunchTime(1, time_report);

 SumScaleResult(In_Parm, &Out_Parm);
 WriteResult(In_Parm, Out_Parm, time_report);
}

/*************************************************************
 *          Get the file name of the input data file from the
 *          argument to the command line.
 ****/
void GetFnameFromArgv(int argc,
                                                char * argv[],
                                                char * input_filename)
{
 if(argc>=2) {                          /* filename in command line */
  strcpy(input_filename, argv[1]);
 }
 else
  input_filename[0] = '\0';
}


/*************************************************************
 *          Execute Monte Carlo simulation for one independent run.
 ****/
void DoOneRun(short NumRuns, InputStruct *In_Ptr)
{
 register long i_photon;
          /* index to photon. register for speed.*/
 OutStruct out_parm;            /* distribution of photons.*/
 PhotonStruct photon;
 long num_photons = In_Ptr->num_photons, photon_rep=10;

#if THINKCPROFILER
 InitProfile(200,200); cecho2file("prof.rpt",0, stdout);
#endif

 InitOutputData(*In_Ptr, &out_parm);
 out_parm.Rsp = Rspecular(In_Ptr->layerspecs);
 i_photon = num_photons;
```

```
 PunchTime(0, "");

 do {
  if(num_photons - i_photon == photon_rep) {
   printf("%ld photons & %hd runs left, ", i_photon, NumRuns);
   PredictDoneTime(num_photons - i_photon, num_photons);
   photon_rep *= 10;
  }
  LaunchPhoton(out_parm.Rsp, In_Ptr->layerspecs, &photon);
  do  HopDropSpin(In_Ptr, &photon, &out_parm);
  while (!photon.dead);
 } while(--i_photon);

#if THINKCPROFILER
 exit(0);
#endif

 ReportResult(*In_Ptr, out_parm);
 FreeData(*In_Ptr, &out_parm);
}

/*************************************************************
 *          The argument to the command line is filename, if any.
 *          Macintosh does not support command line.
 ****/
int
main(int argc, char *argv[])
{
 char input_filename[STRLEN];
 FILE *input_file_ptr;
 short num_runs;      /* number of independent runs. */
 InputStruct in_parm;

 //ShowVersion("Version 1.2.2, 2000"); honda changed 121119
 GetFnameFromArgv(argc, argv, input_filename);
 input_file_ptr = GetFile(input_filename);
 CheckParm(input_file_ptr, &in_parm);
 num_runs = ReadNumRuns(input_file_ptr);

 while(num_runs--) {
  ReadParm(input_file_ptr, &in_parm);
          DoOneRun(num_runs, &in_parm);
 }

 fclose(input_file_ptr);
 return(0);
}
```

3 mcmlio.c

```
#include "mcml.h"

/*************************************************************
 *          Structure used to check against duplicated file names.
 ****/
struct NameList {
 char name[STRLEN];
 struct NameList * next;
};

typedef struct NameList NameNode;
typedef NameNode * NameLink;


/*************************************************************
 *          Center a string according to the column width.
 ****/
char * CenterStr(short  Wid,
                                        char * InStr,
                                        char * OutStr)
{
 size_t nspaces;      /* number of spaces to be filled */
                                                /* before InStr. */

 nspaces = (Wid - strlen(InStr))/2;
```

```
  if(nspaces<0) nspaces = 0;

  strcpy(OutStr, "");
  while(nspaces--)  strcat(OutStr, " ");

  strcat(OutStr, InStr);

  return(OutStr);
}

/****************************************************************************
 *          Center a string according to the column width.
 ****/
#define COLWIDTH 80
void
CtrPuts(char *InStr)
{
 short    nspaces;              /* number of spaces to be left-filled. */
 char     outstr[STRLEN];

 nspaces = (COLWIDTH - strlen(InStr)) / 2;
 if (nspaces < 0)
  nspaces = 0;

 strcpy(outstr, "");
 while (nspaces--)
  strcat(outstr, " ");

 strcat(outstr, InStr);

 puts(outstr);
}

/************************************************************
 *          Print some messages before starting simulation.
 *          e.g. author, address, program version, year.
 ****/
#define COLWIDTH 80
void ShowVersion(char *version)
{
 char str[STRLEN];

 CtrPuts(" ");
 CtrPuts(
 "Monte Carlo Simulation of Light Transport in Multi-layered Turbid Media");
 CtrPuts(version);
 CtrPuts(" ");

 CtrPuts("Lihong Wang, Ph.D.");
 CtrPuts("Biomedical Engineering Program, Texas A&M University, 3120 TAMU");
 CtrPuts("College Station, Texas 77843-3120, USA");
 CtrPuts("Email: LWang@tamu.edu");

 CtrPuts(" ");
 CtrPuts("Steven L. Jacques, Ph.D.");
 CtrPuts("Oregon Medical Laser Center");
 CtrPuts("Providence/St. Vincent Hospital");
 CtrPuts("9205 SW Barnes Rd., Portland, OR 97225, USA");
 CtrPuts("Email: SJacques@eeap.ogi.edu");

 CtrPuts(" ");
 CtrPuts("The program can be obtained from http://oilab.tamu.edu");
 CtrPuts("Please cite the following article in your publications:");
 printf("\tL.-H. Wang, S. L. Jacques, and L.-Q. Zheng, MCML - Monte \n");
 printf("\tCarlo modeling of photon transport in multi-layered\n");
 printf("\ttissues, Computer Methods and Programs in Biomedicine, 47,\n");
 printf("\t131-146 (1995)\n");

 puts("\n");
}
#undef COLWIDTH

/************************************************************
 *          Get a filename and open it for reading, retry until
 *          the file can be opened. '.' terminates the program.
```

```
 *
 *          If Fname != NULL, try Fname first.
 ****/
FILE *GetFile(char *Fname)
{
 FILE * file=NULL;
 Boolean firsttime=1;

 do {
  if(firsttime && Fname[0]!='\0') {
            /* use the filename from command line */
   firsttime = 0;
  }
  else {
   printf("Input filename(or . to exit):");
   scanf("%s", Fname);
   firsttime = 0;
  }

  if(strlen(Fname) == 1 && Fname[0] == '.')
   exit(1);                          /* exit if no filename entered. */

  file = fopen(Fname, "r");
 } while(file == NULL);

 return(file);
}

/*************************************************************
 *          Kill the ith char (counting from 0), push the following
 *          chars forward by one.
 ****/
void KillChar(size_t i, char * Str)
{
 size_t sl = strlen(Str);

 for(;i<sl;i++) Str[i] = Str[i+1];
}

/*************************************************************
 *          Eliminate the chars in a string which are not printing
 *          chars or spaces.
 *
 *          Spaces include ' ', '\f', '\t' etc.
 *
 *          Return 1 if no nonprinting chars found, otherwise
 *          return 0.
 ****/
Boolean CheckChar(char * Str)
{
 Boolean found = 0;  /* found bad char. */
 size_t sl = strlen(Str);
 size_t i=0;

 while(i<sl)
  if (Str[i]<0 || Str[i]>255)
   nrerror("Non-ASCII file\n");
  else if(isprint(Str[i]) || isspace(Str[i]))
   i++;
  else {
   found = 1;
   KillChar(i, Str);
   sl--;
  }

 return(found);
}

/*************************************************************
 *          Return 1 if this line is a comment line in which the
 *          first non-space character is "#".
 *
 *          Also return 1 if this line is space line.
 ****/
Boolean CommentLine(char *Buf)
```

```
{
 size_t spn, cspn;

 spn = strspn(Buf, " \t");
 /* length spanned by space or tab chars. */

 cspn = strcspn(Buf, "#\n");
 /* length before the 1st # or return. */

 if(spn == cspn)        /* comment line or space line. */
          return(1);
 else                                          /* the line has data. */
          return(0);
}

/*************************************************************
 *          Skip space or comment lines and return a data line only.
 ****/
char * FindDataLine(FILE *File_Ptr)
{
 static char buf[STRLEN];        /* LW 1/11/2000. Added static. */

 buf[0] = '\0';
 do {       /* skip space or comment lines. */
  if(fgets(buf, 255, File_Ptr) == NULL)  {
   printf("Incomplete data\n");
   buf[0]='\0';
   break;
  }
  else
   CheckChar(buf);
 } while(CommentLine(buf));

 return(buf);
}

/*************************************************************
 *          Skip file version, then read number of runs.
 ****/
short ReadNumRuns(FILE* File_Ptr)
{
 char buf[STRLEN];
 short n=0;

 FindDataLine(File_Ptr); /* skip file version. */

 strcpy(buf, FindDataLine(File_Ptr));
 if(buf[0]=='\0') nrerror("Reading number of runs\n");
 sscanf(buf, "%hd",&n);
 return(n);
}


/*************************************************************
 *          Read the file name and the file format.
 *
 *          The file format can be either A for ASCII or B for
 *          binary.
 ****/
void ReadFnameFormat(FILE *File_Ptr, InputStruct *In_Ptr)
{
 char buf[STRLEN];

 /** read in file name and format. **/
 strcpy(buf, FindDataLine(File_Ptr));
 if(buf[0]=='\0')
          nrerror("Reading file name and format.\n");
 sscanf(buf, "%s %c",
          In_Ptr->out_fname, &(In_Ptr->out_fformat) );
 if(toupper(In_Ptr->out_fformat) != 'B')
          In_Ptr->out_fformat = 'A';
}


/*************************************************************
```

```
 *           Read the number of photons.
 ****/
void ReadNumPhotons(FILE *File_Ptr, InputStruct *In_Ptr)
{
 char buf[STRLEN];

 /** read in number of photons. **/
 strcpy(buf, FindDataLine(File_Ptr));
 if(buf[0]=='\0')
           nrerror("Reading number of photons.\n");
 sscanf(buf, "%ld", &In_Ptr->num_photons);
 if(In_Ptr->num_photons<=0)
           nrerror("Nonpositive number of photons.\n");
}


/************************************************************
 *           Read the members dz and dr.
 ****/
void ReadDzDr(FILE *File_Ptr, InputStruct *In_Ptr)
{
 char buf[STRLEN];

 /** read in dz, dr. **/
 strcpy(buf, FindDataLine(File_Ptr));
 if(buf[0]=='\0') nrerror("Reading dz, dr.\n");
 sscanf(buf, "%lf%lf", &In_Ptr->dz, &In_Ptr->dr);
 if(In_Ptr->dz<=0) nrerror("Nonpositive dz.\n");
 if(In_Ptr->dr<=0) nrerror("Nonpositive dr.\n");
}


/************************************************************
 *           Read the members nz, nr, na.
 ****/
void ReadNzNrNa(FILE *File_Ptr, InputStruct *In_Ptr)
{
 char buf[STRLEN];

 /** read in number of dz, dr, da. **/
 strcpy(buf, FindDataLine(File_Ptr));
 if(buf[0]=='\0')
           nrerror("Reading number of dz, dr, da's.\n");
 sscanf(buf, "%hd%hd%hd",
           &In_Ptr->nz, &In_Ptr->nr, &In_Ptr->na);
 if(In_Ptr->nz<=0)
           nrerror("Nonpositive number of dz's.\n");
 if(In_Ptr->nr<=0)
           nrerror("Nonpositive number of dr's.\n");
 if(In_Ptr->na<=0)
           nrerror("Nonpositive number of da's.\n");
 In_Ptr->da = 0.5*PI/In_Ptr->na;
}


/************************************************************
 *           Read the number of layers.
 ****/
void ReadNumLayers(FILE *File_Ptr, InputStruct *In_Ptr)
{
 char buf[STRLEN];

 /** read in number of layers. **/
 strcpy(buf, FindDataLine(File_Ptr));
 if(buf[0]=='\0')
           nrerror("Reading number of layers.\n");
 sscanf(buf, "%hd", &In_Ptr->num_layers);
 if(In_Ptr->num_layers<=0)
           nrerror("Nonpositive number of layers.\n");
}


/************************************************************
 *           Read the refractive index n of the ambient.
 ****/
```

```
void ReadAmbient(FILE *File_Ptr,
                                        LayerStruct * Layer_Ptr,
                                        char *side)
{
 char buf[STRLEN], msg[STRLEN];
 double n;

 strcpy(buf, FindDataLine(File_Ptr));
 if(buf[0]=='\0') {
  sprintf(msg, "Rading n of %s ambient.\n", side);
          nrerror(msg);
 }

 sscanf(buf, "%lf", &n );
 if(n<=0) nrerror("Wrong n.\n");
 Layer_Ptr->n = n;
}


/*************************************************************
 *          Read the parameters of one layer.
 *
 *          Return 1 if error detected.
 *          Return 0 otherwise.
 *
 *          *Z_Ptr is the z coordinate of the current layer, which
 *          is used to convert thickness of layer to z coordinates
 *          of the two boundaries of the layer.
 ****/
Boolean ReadOneLayer(FILE *File_Ptr,
                                                LayerStruct * Layer_Ptr,
                                                double *Z_Ptr)
{
 char buf[STRLEN], msg[STRLEN];
 double d, n, mua, mus, g;          /* d is thickness. */

 strcpy(buf, FindDataLine(File_Ptr));
 if(buf[0]=='\0') return(1);          /* error. */

 sscanf(buf, "%lf%lf%lf%lf%lf", &n, &mua, &mus, &g, &d);
 if(d<0 || n<=0 || mua<0 || mus<0 || g<0 || g>1)
  return(1);                                    /* error. */

 Layer_Ptr->n          = n;
 Layer_Ptr->mua = mua;
 Layer_Ptr->mus = mus;
 Layer_Ptr->g   = g;
 Layer_Ptr->z0         = *Z_Ptr;
 *Z_Ptr += d;
 Layer_Ptr->z1         = *Z_Ptr;

 return(0);
}

/*************************************************************
 *          Read the parameters of one layer at a time.
 ****/
void ReadLayerSpecs(FILE *File_Ptr,
                                                short Num_Layers,
                                                LayerStruct ** Layerspecs_PP)
{
 char msg[STRLEN];
 short i=0;
 double z = 0.0;        /* z coordinate of the current layer. */

 /* Allocate an array for the layer parameters. */
 /* layer 0 and layer Num_Layers + 1 are for ambient. */
 *Layerspecs_PP = (LayerStruct *)
  malloc((unsigned) (Num_Layers+2)*sizeof(LayerStruct));
 if (!(*Layerspecs_PP))
  nrerror("allocation failure in ReadLayerSpecs()");

 ReadAmbient(File_Ptr, &((*Layerspecs_PP)[i]), "top");
 for(i=1; i<=Num_Layers; i++)
  if(ReadOneLayer(File_Ptr, &((*Layerspecs_PP)[i]), &z)) {
```

```
    sprintf(msg, "Error reading %hd of %hd layers\n",
                                        i, Num_Layers);
            nrerror(msg);
  }
 ReadAmbient(File_Ptr, &((*Layerspecs_PP)[i]), "bottom");
}

/*************************************************************
 *          Compute the critical angles for total internal
 *          reflection according to the relative refractive index
 *          of the layer.
 *          All layers are processed.
 ****/
void CriticalAngle( short Num_Layers,
                                                LayerStruct ** Layerspecs_PP)
{
 short i=0;
 double n1, n2;

 for(i=1; i<=Num_Layers; i++) {
  n1 = (*Layerspecs_PP)[i].n;
  n2 = (*Layerspecs_PP)[i-1].n;
  (*Layerspecs_PP)[i].cos_crit0 = n1>n2 ?
                        sqrt(1.0 - n2*n2/(n1*n1)) : 0.0;

  n2 = (*Layerspecs_PP)[i+1].n;
  (*Layerspecs_PP)[i].cos_crit1 = n1>n2 ?
                        sqrt(1.0 - n2*n2/(n1*n1)) : 0.0;
 }
}

/*************************************************************
 *          Read in the input parameters for one run.
 ****/
void ReadParm(FILE* File_Ptr, InputStruct * In_Ptr)
{
 char buf[STRLEN];

 In_Ptr->Wth = WEIGHT;

 ReadFnameFormat(File_Ptr, In_Ptr);
 ReadNumPhotons(File_Ptr, In_Ptr);
 ReadDzDr(File_Ptr, In_Ptr);
 ReadNzNrNa(File_Ptr, In_Ptr);
 ReadNumLayers(File_Ptr, In_Ptr);

 ReadLayerSpecs(File_Ptr, In_Ptr->num_layers,
                                        &In_Ptr->layerspecs);
 CriticalAngle(In_Ptr->num_layers, &In_Ptr->layerspecs);
}

/*************************************************************
 *          Return 1, if the name in the name list.
 *          Return 0, otherwise.
 ****/
Boolean NameInList(char *Name, NameLink List)
{
 while (List != NULL) {
          if(strcmp(Name, List->name) == 0)
            return(1);
          List = List->next;
 };
 return(0);
}

/*************************************************************
 *          Add the name to the name list.
 ****/
void AddNameToList(char *Name, NameLink * List_Ptr)
{
 NameLink list = *List_Ptr;

 if(list == NULL) {   /* first node. */
          *List_Ptr = list = (NameLink)malloc(sizeof(NameNode));
          strcpy(list->name, Name);
```

```
            list->next = NULL;
 }
 else {                                          /* subsequent nodes. */
            /* Move to the last node. */
            while(list->next != NULL)
              list = list->next;

            /* Append a node to the list. */
            list->next = (NameLink)malloc(sizeof(NameNode));
            list = list->next;
            strcpy(list->name, Name);
            list->next = NULL;
 }
}

/************************************************************
 *          Check against duplicated file names.
 *
 *          A linked list is set up to store the file names used
 *          in this input data file.
 ****/
Boolean FnameTaken(char *fname, NameLink * List_Ptr)
{
 if(NameInList(fname, *List_Ptr))
            return(1);
 else {
            AddNameToList(fname, List_Ptr);
            return(0);
 }
}

/************************************************************
 *          Free each node in the file name list.
 ****/
void FreeFnameList(NameLink List)
{
 NameLink next;

 while(List != NULL) {
            next = List->next;
            free(List);
            List = next;
 }
}

/************************************************************
 *          Check the input parameters for each run.
 ****/
void CheckParm(FILE* File_Ptr, InputStruct * In_Ptr)
{
 short i_run;
 short num_runs;      /* number of independent runs. */
 NameLink head = NULL;
 Boolean name_taken;/* output files share the same */
                                                 /* file name.*/
 char msg[STRLEN];

 num_runs = ReadNumRuns(File_Ptr);
 for(i_run=1; i_run<=num_runs; i_run++) {
  printf("Checking input data for run %hd\n", i_run);
  ReadParm(File_Ptr, In_Ptr);

            name_taken = FnameTaken(In_Ptr->out_fname, &head);
            if(name_taken)
              sprintf(msg, "file name %s duplicated.\n",
                                                 In_Ptr->out_fname);

  free(In_Ptr->layerspecs);
            if(name_taken) nrerror(msg);
 }
 FreeFnameList(head);
 rewind(File_Ptr);
}
```

```
/************************************************************
 *          Allocate the arrays in OutStruct for one run, and
 *          array elements are automatically initialized to zeros.
 ****/
void InitOutputData(InputStruct In_Parm,
                                                    OutStruct * Out_Ptr)
{
 short nz = In_Parm.nz;
 short nr = In_Parm.nr;
 short na = In_Parm.na;
 short nl = In_Parm.num_layers;
 /* remember to use nl+2 because of 2 for ambient. */

 if(nz<=0 || nr<=0 || na<=0 || nl<=0)
  nrerror("Wrong grid parameters.\n");

 /* Init pure numbers. */
 Out_Ptr->Rsp = 0.0;
 Out_Ptr->Rd  = 0.0;
 Out_Ptr->A   = 0.0;
 Out_Ptr->Tt  = 0.0;

 Out_Ptr->Rd_Port  =0.0; /* honda */
 Out_Ptr->Tt_Port  =0.0; /* honda */

 /* Allocate the arrays and the matrices. */
 Out_Ptr->Rd_ra = AllocMatrix(0,nr-1,0,na-1);
 Out_Ptr->Rd_r  = AllocVector(0,nr-1);
 Out_Ptr->Rd_a  = AllocVector(0,na-1);

 Out_Ptr->A_rz  = AllocMatrix(0,nr-1,0,nz-1);
 Out_Ptr->A_z   = AllocVector(0,nz-1);
 Out_Ptr->A_l   = AllocVector(0,nl+1);

 Out_Ptr->Tt_ra = AllocMatrix(0,nr-1,0,na-1);
 Out_Ptr->Tt_r  = AllocVector(0,nr-1);
 Out_Ptr->Tt_a  = AllocVector(0,na-1);
}

/************************************************************
 *          Undo what InitOutputData did.
 *  i.e. free the data allocations.
 ****/
void FreeData(InputStruct In_Parm, OutStruct * Out_Ptr)
{
 short nz = In_Parm.nz;
 short nr = In_Parm.nr;
 short na = In_Parm.na;
 short nl = In_Parm.num_layers;
 /* remember to use nl+2 because of 2 for ambient. */

 free(In_Parm.layerspecs);

 FreeMatrix(Out_Ptr->Rd_ra, 0,nr-1,0,na-1);
 FreeVector(Out_Ptr->Rd_r, 0,nr-1);
 FreeVector(Out_Ptr->Rd_a, 0,na-1);

 FreeMatrix(Out_Ptr->A_rz, 0, nr-1, 0,nz-1);
 FreeVector(Out_Ptr->A_z, 0, nz-1);
 FreeVector(Out_Ptr->A_l, 0,nl+1);

 FreeMatrix(Out_Ptr->Tt_ra, 0,nr-1,0,na-1);
 FreeVector(Out_Ptr->Tt_r, 0,nr-1);
 FreeVector(Out_Ptr->Tt_a, 0,na-1);
}

/************************************************************
 *          Get 1D array elements by summing the 2D array elements.
 ****/
void Sum2DRd(InputStruct In_Parm, OutStruct * Out_Ptr)
{
 short nr = In_Parm.nr;
 short na = In_Parm.na;
 short ir,ia;
 double sum;
```

```
  /*double nr_Port = nr/2; /* honda */
  double sum_Port; /* honda */

  for(ir=0; ir<nr; ir++)  {
   sum = 0.0;
   for(ia=0; ia<na; ia++) sum += Out_Ptr->Rd_ra[ir][ia];
   Out_Ptr->Rd_r[ir] = sum;
  }

  for(ia=0; ia<na; ia++)  {
   sum = 0.0;
   for(ir=0; ir<nr; ir++) sum += Out_Ptr->Rd_ra[ir][ia];
   Out_Ptr->Rd_a[ia] = sum;
  }

  sum = 0.0;
  for(ir=0; ir<nr; ir++) sum += Out_Ptr->Rd_r[ir];
  Out_Ptr->Rd = sum;

  sum_Port = 0.0; /* honda */
  for(ir=0; ir<250; ir++) sum_Port += Out_Ptr->Rd_r[ir]; /* honda */
  Out_Ptr->Rd_Port = sum_Port; /* honda */
 }

 /*************************************************************
  *          Return the index to the layer according to the index
  *          to the grid line system in z direction (Iz).
  *
  *          Use the center of box.
  ****/
 short IzToLayer(short Iz, InputStruct In_Parm)
 {
  short i=1;/* index to layer. */
  short num_layers = In_Parm.num_layers;
  double dz = In_Parm.dz;

  while( (Iz+0.5)*dz >= In_Parm.layerspecs[i].z1
            && i<num_layers) i++;

  return(i);
 }

 /*************************************************************
  *          Get 1D array elements by summing the 2D array elements.
  ****/
 void Sum2DA(InputStruct In_Parm, OutStruct * Out_Ptr)
 {
  short nz = In_Parm.nz;
  short nr = In_Parm.nr;
  short iz,ir;
  double sum;


  for(iz=0; iz<nz; iz++)  {
   sum = 0.0;
   for(ir=0; ir<nr; ir++) sum += Out_Ptr->A_rz[ir][iz];
   Out_Ptr->A_z[iz] = sum;
  }

  sum = 0.0;
  for(iz=0; iz<nz; iz++) {
   sum += Out_Ptr->A_z[iz];
   Out_Ptr->A_l[IzToLayer(iz, In_Parm)]
            += Out_Ptr->A_z[iz];
  }
  Out_Ptr->A = sum;
 }

 /*************************************************************
  *          Get 1D array elements by summing the 2D array elements.
  ****/
 void Sum2DTt(InputStruct In_Parm, OutStruct * Out_Ptr)
 {
  short nr = In_Parm.nr;
```

```
 short na = In_Parm.na;
 short ir,ia;
 double sum;

 /*double nr_Port = nr/2; /* honda */
 double sum_Port; /* honda */

 for(ir=0; ir<nr; ir++)  {
  sum = 0.0;
  for(ia=0; ia<na; ia++) sum += Out_Ptr->Tt_ra[ir][ia];
  Out_Ptr->Tt_r[ir] = sum;
 }

 for(ia=0; ia<na; ia++)  {
  sum = 0.0;
  for(ir=0; ir<nr; ir++) sum += Out_Ptr->Tt_ra[ir][ia];
  Out_Ptr->Tt_a[ia] = sum;
 }

 sum = 0.0;
 for(ir=0; ir<nr; ir++) sum += Out_Ptr->Tt_r[ir];
 Out_Ptr->Tt = sum;

 sum_Port = 0.0;       /* honda */
 for(ir=0; ir<250; ir++) sum_Port += Out_Ptr->Tt_r[ir]; /* honda */
 Out_Ptr->Tt_Port = sum_Port;  /* honda */
}

/*********************************************************
 *          Scale Rd and Tt properly.
 *
 *          "a" stands for angle alpha.
 ****
 *          Scale Rd(r,a) and Tt(r,a) by
 *    (area perpendicular to photon direction)
 *                    x(solid angle)x(No. of photons).
 *          or
 *                    [2*PI*r*dr*cos(a)]x[2*PI*sin(a)*da]x[No. of photons]
 *          or
 *                    [2*PI*PI*dr*da*r*sin(2a)]x[No. of photons]
 ****
 *          Scale Rd(r) and Tt(r) by
 *                    (area on the surface)x(No. of photons).
 ****
 *          Scale Rd(a) and Tt(a) by
 *                    (solid angle)x(No. of photons).
 ****/
void ScaleRdTt(InputStruct In_Parm, OutStruct *        Out_Ptr)
{
 short nr = In_Parm.nr;
 short na = In_Parm.na;
 double dr = In_Parm.dr;
 double da = In_Parm.da;
 short ir,ia;
 double scale1, scale2;

 scale1 = 4.0*PI*PI*dr*sin(da/2)*dr*In_Parm.num_photons;
          /* The factor (ir+0.5)*sin(2a) to be added. */

 for(ir=0; ir<nr; ir++)
  for(ia=0; ia<na; ia++) {
   scale2 = 1.0/((ir+0.5)*sin(2.0*(ia+0.5)*da)*scale1);
   Out_Ptr->Rd_ra[ir][ia] *= scale2;
   Out_Ptr->Tt_ra[ir][ia] *= scale2;
  }

 scale1 = 2.0*PI*dr*dr*In_Parm.num_photons;
          /* area is 2*PI*[(ir+0.5)*dr]*dr.*/
          /* ir+0.5 to be added. */

 for(ir=0; ir<nr; ir++) {
  scale2 = 1.0/((ir+0.5)*scale1);
  Out_Ptr->Rd_r[ir] *= scale2;
  Out_Ptr->Tt_r[ir] *= scale2;
 }
```

```
  scale1  = 2.0*PI*da*In_Parm.num_photons;
   /* solid angle is 2*PI*sin(a)*da. sin(a) to be added. */

  for(ia=0; ia<na; ia++) {
   scale2 = 1.0/(sin((ia+0.5)*da)*scale1);
   Out_Ptr->Rd_a[ia] *= scale2;
   Out_Ptr->Tt_a[ia] *= scale2;
  }

  scale2 = 1.0/(double)In_Parm.num_photons;
  Out_Ptr->Rd *= scale2;
  Out_Ptr->Tt *= scale2;

  Out_Ptr->Rd_Port *= scale2; /* honda */
  Out_Ptr->Tt_Port *= scale2; /* honda */

 }

 /************************************************************
  *          Scale absorption arrays properly.
  ****/
 void ScaleA(InputStruct In_Parm, OutStruct * Out_Ptr)
 {
  short nz = In_Parm.nz;
  short nr = In_Parm.nr;
  double dz = In_Parm.dz;
  double dr = In_Parm.dr;
  short nl = In_Parm.num_layers;
  short iz,ir;
  short il;
  double scale1;

  /* Scale A_rz. */
  scale1 = 2.0*PI*dr*dr*dz*In_Parm.num_photons;
            /* volume is 2*pi*(ir+0.5)*dr*dr*dz.*/
            /* ir+0.5 to be added. */
  for(iz=0; iz<nz; iz++)
   for(ir=0; ir<nr; ir++)
    Out_Ptr->A_rz[ir][iz] /= (ir+0.5)*scale1;

  /* Scale A_z. */
  scale1 = 1.0/(dz*In_Parm.num_photons);
  for(iz=0; iz<nz; iz++)
   Out_Ptr->A_z[iz] *= scale1;

  /* Scale A_l. Avoid int/int. */
  scale1 = 1.0/(double)In_Parm.num_photons;
  for(il=0; il<=nl+1; il++)
   Out_Ptr->A_l[il] *= scale1;

  Out_Ptr->A *=scale1;
 }

 /************************************************************
  *          Sum and scale results of current run.
  ****/
 void SumScaleResult(InputStruct In_Parm,
                                                  OutStruct * Out_Ptr)
 {
  /* Get 1D & 0D results. */
  Sum2DRd(In_Parm, Out_Ptr);
  Sum2DA(In_Parm,  Out_Ptr);
  Sum2DTt(In_Parm, Out_Ptr);

  ScaleRdTt(In_Parm, Out_Ptr);
  ScaleA(In_Parm, Out_Ptr);
 }

 /************************************************************
  *          Write the version number as the first string in the
  *          file.
  *          Use chars only so that they can be read as either
  *          ASCII or binary.
  ****/
```

```
void WriteVersion(FILE *file, char *Version)
{
 fprintf(file,
          "%s \t# Version number of the file format.\n\n",
          Version);
 fprintf(file, "####\n# Data categories include: \n");
 fprintf(file, "# InParm, RAT, \n");
 fprintf(file, "# A_l, A_z, Rd_r, Rd_a, Tt_r, Tt_a, \n");
 fprintf(file, "# A_rz, Rd_ra, Tt_ra \n####\n\n");
}

/*************************************************************
 *          Write the input parameters to the file.
 ****/
void WriteInParm(FILE *file, InputStruct In_Parm)
{
 short i;

 fprintf(file,
          "InParm \t\t\t# Input parameters. cm is used.\n");

 fprintf(file,
          "%s \tA\t\t# output file name, ASCII.\n",
          In_Parm.out_fname);
 fprintf(file,
          "%ld \t\t\t# No. of photons\n", In_Parm.num_photons);

 fprintf(file,
          "%G\t%G\t\t# dz, dr [cm]\n", In_Parm.dz,In_Parm.dr);
 fprintf(file, "%hd\t%hd\t%hd\t# No. of dz, dr, da.\n\n",
           In_Parm.nz, In_Parm.nr, In_Parm.na);

 fprintf(file,
          "%hd\t\t\t\t\t# Number of layers\n",
          In_Parm.num_layers);
 fprintf(file,
          "#n\tmua\tmus\tg\td\t# One line for each layer\n");
 fprintf(file,
          "%G\t\t\t\t\t# n for medium above\n",
          In_Parm.layerspecs[0].n);
 for(i=1; i<=In_Parm.num_layers; i++)  {
  LayerStruct s;
  s = In_Parm.layerspecs[i];
  fprintf(file, "%G\t%G\t%G\t%G\t%G\t# layer %hd\n",
            s.n, s.mua, s.mus, s.g, s.z1-s.z0, i);
 }
 fprintf(file, "%G\t\t\t\t\t# n for medium below\n\n",
          In_Parm.layerspecs[i].n);
}

/*************************************************************
 *          Write reflectance, absorption, transmission.
 ****/
void WriteRAT(FILE * file, OutStruct Out_Parm)
{
  fprintf(file,
          "%-14.6G \t", Out_Parm.Rd_Port); /* honda */
 fprintf(file,
          "%-14.6G ", Out_Parm.Tt_Port); /* honda */

 fprintf(file, "\n");
}

/*************************************************************
 *          Write absorption as a function of layer.
 ****/
void WriteA_layer(FILE * file,
                                        short Num_Layers,
                                        OutStruct Out_Parm)
{
 short i;

 fprintf(file,
          "A_l #Absorption as a function of layer. [-]\n");
          /* flag. */
```

```
 for(i=1; i<=Num_Layers; i++)
  fprintf(file, "%12.4G\n", Out_Parm.A_l[i]);
 fprintf(file, "\n");
}

/************************************************************
 *          5 numbers each line.
 ****/
void WriteRd_ra(FILE * file,
                                        short Nr,
                                        short Na,
                                        OutStruct Out_Parm)
{
 short ir, ia;

 fprintf(file,
          "%s\n%s\n%s\n%s\n%s\n%s\n",          /* flag. */
          "# Rd[r][angle]. [1/(cm2sr)].",
          "# Rd[0][0], [0][1],..[0][na-1]",
          "# Rd[1][0], [1][1],..[1][na-1]",
          "# ...",
          "# Rd[nr-1][0], [nr-1][1],..[nr-1][na-1]",
          "Rd_ra");

 for(ir=0;ir<Nr;ir++)
  for(ia=0;ia<Na;ia++)  {
   fprintf(file, "%12.4E ", Out_Parm.Rd_ra[ir][ia]);
   if( (ir*Na + ia + 1)%5 == 0) fprintf(file, "\n");
  }

 fprintf(file, "\n");
}

/************************************************************
 *          1 number each line.
 ****/
void WriteRd_r(FILE * file,
                                    short Nr,
                                    OutStruct Out_Parm)
{
 short ir;

 fprintf(file,
          "Rd_r #Rd[0], [1],..Rd[nr-1]. [1/cm2]\n");   /* flag. */

 for(ir=0;ir<Nr;ir++) {
  fprintf(file, "%12.4E\n", Out_Parm.Rd_r[ir]);
 }

 fprintf(file, "\n");
}

/************************************************************
 *          1 number each line.
 ****/
void WriteRd_a(FILE * file,
                                    short Na,
                                    OutStruct Out_Parm)
{
 short ia;

 fprintf(file,
          "Rd_a #Rd[0], [1],..Rd[na-1]. [sr-1]\n");     /* flag. */

 for(ia=0;ia<Na;ia++) {
  fprintf(file, "%12.4E\n", Out_Parm.Rd_a[ia]);
 }

 fprintf(file, "\n");
}

/************************************************************
 *          5 numbers each line.
 ****/
```

```
void WriteTt_ra(FILE * file,
                                        short Nr,
                                        short Na,
                                        OutStruct Out_Parm)
{
 short ir, ia;

 fprintf(file,
          "%s\n%s\n%s\n%s\n%s\n%s\n",          /* flag. */
          "# Tt[r][angle]. [1/(cm2sr)].",
          "# Tt[0][0], [0][1],..[0][na-1]",
          "# Tt[1][0], [1][1],..[1][na-1]",
          "# ...",
          "# Tt[nr-1][0], [nr-1][1],..[nr-1][na-1]",
          "Tt_ra");

 for(ir=0;ir<Nr;ir++)
  for(ia=0;ia<Na;ia++)  {
   fprintf(file, "%12.4E ", Out_Parm.Tt_ra[ir][ia]);
   if( (ir*Na + ia + 1)%5 == 0) fprintf(file, "\n");
  }

 fprintf(file, "\n");
}

/************************************************************
 *          5 numbers each line.
 ****/
void WriteA_rz(FILE * file,
                                  short Nr,
                                  short Nz,
                                  OutStruct Out_Parm)
{
 short iz, ir;

 fprintf(file,
          "%s\n%s\n%s\n%s\n%s\n%s\n", /* flag. */
          "# A[r][z]. [1/cm3]",
          "# A[0][0], [0][1],..[0][nz-1]",
          "# A[1][0], [1][1],..[1][nz-1]",
          "# ...",
          "# A[nr-1][0], [nr-1][1],..[nr-1][nz-1]",
          "A_rz");

 for(ir=0;ir<Nr;ir++)
  for(iz=0;iz<Nz;iz++)  {
   fprintf(file, "%12.4E ", Out_Parm.A_rz[ir][iz]);
   if( (ir*Nz + iz + 1)%5 == 0) fprintf(file, "\n");
  }

 fprintf(file, "\n");
}

/************************************************************
 *          1 number each line.
 ****/
void WriteA_z(FILE * file,
                                  short Nz,
                                  OutStruct Out_Parm)
{
 short iz;

 fprintf(file,
          "A_z #A[0], [1],..A[nz-1]. [1/cm]\n");          /* flag. */

 for(iz=0;iz<Nz;iz++) {
  fprintf(file, "%12.4E\n", Out_Parm.A_z[iz]);
 }

 fprintf(file, "\n");
}

/************************************************************
 *          1 number each line.
 ****/
```

```
void WriteTt_r(FILE * file,
                                    short Nr,
                                    OutStruct Out_Parm)
{
 short ir;

 fprintf(file,
          "Tt_r #Tt[0], [1],..Tt[nr-1]. [1/cm2]\n"); /* flag. */

 for(ir=0;ir<Nr;ir++) {
  fprintf(file, "%12.4E\n", Out_Parm.Tt_r[ir]);
 }

 fprintf(file, "\n");
}

/*************************************************************
 *          1 number each line.
 ****/
void WriteTt_a(FILE * file,
                                    short Na,
                                    OutStruct Out_Parm)
{
 short ia;

 fprintf(file,
          "Tt_a #Tt[0], [1],..Tt[na-1]. [sr-1]\n"); /* flag. */

 for(ia=0;ia<Na;ia++) {
  fprintf(file, "%12.4E\n", Out_Parm.Tt_a[ia]);
 }

 fprintf(file, "\n");
}

/*************************************************************
 ****/
void WriteResult(InputStruct In_Parm,
                                          OutStruct Out_Parm,
                                          char * TimeReport)
{
 FILE *file;

 file = fopen(In_Parm.out_fname, "w");
 if(file == NULL) nrerror("Cannot open file to write.\n");

  WriteRAT(file, Out_Parm);
          /* reflectance, absorption, transmittance. honda */

 fclose(file);
}
```

4 mcmlgo.c

```
#include "mcml.h"

#define STANDARDTEST 0
 /* testing program using fixed rnd seed. */

#define PARTIALREFLECTION 0
 /* 1=split photon, 0=statistical reflection. */

#define COSZERO (1.0-1.0E-12)
 /* cosine of about 1e-6 rad. */

#define COS90D  1.0E-6
 /* cosine of about 1.57 - 1e-6 rad. */


/*************************************************************
 *          A random number generator from Numerical Recipes in C.
 ****/
#define MBIG 1000000000
#define MSEED 161803398
```

```
#define MZ 0
#define FAC 1.0E-9

float ran3(int *idum)
{
 static int inext,inextp;
 static long ma[56];
 static int iff=0;
 long mj,mk;
 int i,ii,k;

 if (*idum < 0 || iff == 0) {
  iff=1;
  mj=MSEED-(*idum < 0 ? -*idum : *idum);
  mj %= MBIG;
  ma[55]=mj;
  mk=1;
  for (i=1;i<=54;i++) {
   ii=(21*i) % 55;
   ma[ii]=mk;
   mk=mj-mk;
   if (mk < MZ) mk += MBIG;
   mj=ma[ii];
  }
  for (k=1;k<=4;k++)
   for (i=1;i<=55;i++) {
          ma[i] -= ma[1+(i+30) % 55];
          if (ma[i] < MZ) ma[i] += MBIG;
   }
  inext=0;
  inextp=31;
  *idum=1;
 }
 if (++inext == 56) inext=1;
 if (++inextp == 56) inextp=1;
 mj=ma[inext]-ma[inextp];
 if (mj < MZ) mj += MBIG;
 ma[inext]=mj;
 return mj*FAC;
}

#undef MBIG
#undef MSEED
#undef MZ
#undef FAC


/*************************************************************
 *          Generate a random number between 0 and 1.  Take a
 *          number as seed the first time entering the function.
 *          The seed is limited to 1<<15.
 *          We found that when idum is too large, ran3 may return
 *          numbers beyond 0 and 1.
 ****/
double RandomNum(void)
{
 static Boolean first_time=1;
 static int idum;       /* seed for ran3. */

 if(first_time) {
#if STANDARDTEST /* Use fixed seed to test the program. */
  idum = - 1;
#else
  idum = -(int)time(NULL)%(1<<15);
          /* use 16-bit integer as the seed. */
#endif
  ran3(&idum);
  first_time = 0;
  idum = 1;
 }

 return( (double)ran3(&idum) );
}

/*************************************************************
```

```
 *          Compute the specular reflection.
 *
 *          If the first layer is a turbid medium, use the Fresnel
 *          reflection from the boundary of the first layer as the
 *          specular reflectance.
 *
 *          If the first layer is glass, multiple reflections in
 *          the first layer is considered to get the specular
 *          reflectance.
 *
 *          The subroutine assumes the Layerspecs array is correctly
 *          initialized.
 ****/
double Rspecular(LayerStruct * Layerspecs_Ptr)
{
 double r1, r2;
          /* direct reflections from the 1st and 2nd layers. */
 double temp;

 temp =(Layerspecs_Ptr[0].n - Layerspecs_Ptr[1].n)
           /(Layerspecs_Ptr[0].n + Layerspecs_Ptr[1].n);
 r1 = temp*temp;

 if((Layerspecs_Ptr[1].mua == 0.0)
 && (Layerspecs_Ptr[1].mus == 0.0)) { /* glass layer. */
  temp = (Layerspecs_Ptr[1].n - Layerspecs_Ptr[2].n)
                    /(Layerspecs_Ptr[1].n + Layerspecs_Ptr[2].n);
  r2 = temp*temp;
  r1 = r1 + (1-r1)*(1-r1)*r2/(1-r1*r2);
 }

 return (r1);
}

/*****************************************************************
 *          Initialize a photon packet.
 ****/
void LaunchPhoton(double Rspecular,
                                        LayerStruct  * Layerspecs_Ptr,
                                        PhotonStruct * Photon_Ptr)
{
 Photon_Ptr->w                = 1.0 - Rspecular;
 Photon_Ptr->dead    = 0;
 Photon_Ptr->layer = 1;
 Photon_Ptr->s        = 0;
 Photon_Ptr->sleft= 0;

 Photon_Ptr->x        = 0.0;
 Photon_Ptr->y                = 0.0;
 Photon_Ptr->z                = 0.0;
 Photon_Ptr->ux       = 0.0;
 Photon_Ptr->uy       = 0.0;
 Photon_Ptr->uz       = 1.0;

 if((Layerspecs_Ptr[1].mua == 0.0)
 && (Layerspecs_Ptr[1].mus == 0.0)) { /* glass layer. */
  Photon_Ptr->layer  = 2;
  Photon_Ptr->z        = Layerspecs_Ptr[2].z0;
 }
}

/*****************************************************************
 *          Choose (sample) a new theta angle for photon propagation
 *          according to the anisotropy.
 *
 *          If anisotropy g is 0, then
 *                    cos(theta) = 2*rand-1.
 *          otherwise
 *                    sample according to the Henyey-Greenstein function.
 *
 *          Returns the cosine of the polar deflection angle theta.
 ****/
double SpinTheta(double g)
{
 double cost;
```

```
 if(g == 0.0)
  cost = 2*RandomNum() -1;
 else {
  double temp = (1-g*g)/(1-g+2*g*RandomNum());
  cost = (1+g*g - temp*temp)/(2*g);
            if(cost < -1) cost = -1;
            else if(cost > 1) cost = 1;
 }
 return(cost);
}


/*************************************************************
 *          Choose a new direction for photon propagation by
 *          sampling the polar deflection angle theta and the
 *          azimuthal angle psi.
 *
 *          Note:
 *          theta: 0 - pi so sin(theta) is always positive
 *          feel free to use sqrt() for cos(theta).
 *
 *          psi:  0 - 2pi
 *          for 0-pi  sin(psi) is +
 *          for pi-2pi sin(psi) is -
 ****/
void Spin(double g,
                        PhotonStruct * Photon_Ptr)
{
 double cost, sint;     /* cosine and sine of the */
                                                    /* polar deflection angle theta. */
 double cosp, sinp;     /* cosine and sine of the */
                                                    /* azimuthal angle psi. */
 double ux = Photon_Ptr->ux;
 double uy = Photon_Ptr->uy;
 double uz = Photon_Ptr->uz;
 double psi;

 cost = SpinTheta(g);
 sint = sqrt(1.0 - cost*cost);
            /* sqrt() is faster than sin(). */

 psi = 2.0*PI*RandomNum(); /* spin psi 0-2pi. */
 cosp = cos(psi);
 if(psi<PI)
  sinp = sqrt(1.0 - cosp*cosp);
             /* sqrt() is faster than sin(). */
 else
  sinp = - sqrt(1.0 - cosp*cosp);

 if(fabs(uz) > COSZERO) {       /* normal incident. */
  Photon_Ptr->ux = sint*cosp;
  Photon_Ptr->uy = sint*sinp;
  Photon_Ptr->uz = cost*SIGN(uz);
             /* SIGN() is faster than division. */
 }
 else {                 /* regular incident. */
  double temp = sqrt(1.0 - uz*uz);
  Photon_Ptr->ux = sint*(ux*uz*cosp - uy*sinp)
                                                    /temp + ux*cost;
  Photon_Ptr->uy = sint*(uy*uz*cosp + ux*sinp)
                                                    /temp + uy*cost;
  Photon_Ptr->uz = -sint*cosp*temp + uz*cost;
 }
}

/*************************************************************
 *          Move the photon s away in the current layer of medium.
 ****/
void Hop(PhotonStruct *         Photon_Ptr)
{
 double s = Photon_Ptr->s;

 Photon_Ptr->x += s*Photon_Ptr->ux;
 Photon_Ptr->y += s*Photon_Ptr->uy;
```

```
 Photon_Ptr->z += s*Photon_Ptr->uz;
}

/*************************************************************
 *      If uz != 0, return the photon step size in glass,
 *      Otherwise, return 0.
 *
 *      The step size is the distance between the current
 *      position and the boundary in the photon direction.
 *
 *      Make sure uz !=0 before calling this function.
 ****/
void StepSizeInGlass(PhotonStruct *  Photon_Ptr,
                                                InputStruct  *  In_Ptr)
{
 double dl_b;          /* step size to boundary. */
 short  layer = Photon_Ptr->layer;
 double uz = Photon_Ptr->uz;

 /* Stepsize to the boundary. */
 if(uz>0.0)
  dl_b = (In_Ptr->layerspecs[layer].z1 - Photon_Ptr->z)
                        /uz;
 else if(uz<0.0)
  dl_b = (In_Ptr->layerspecs[layer].z0 - Photon_Ptr->z)
                        /uz;
 else
  dl_b = 0.0;

 Photon_Ptr->s = dl_b;
}

/*************************************************************
 *      Pick a step size for a photon packet when it is in
 *      tissue.
 *      If the member sleft is zero, make a new step size
 *      with: -log(rnd)/(mua+mus).
 *      Otherwise, pick up the leftover in sleft.
 *
 *      Layer is the index to layer.
 *      In_Ptr is the input parameters.
 ****/
void StepSizeInTissue(PhotonStruct * Photon_Ptr,
                                                InputStruct  * In_Ptr)
{
 short  layer = Photon_Ptr->layer;
 double mua = In_Ptr->layerspecs[layer].mua;
 double mus = In_Ptr->layerspecs[layer].mus;

 if(Photon_Ptr->sleft == 0.0) {  /* make a new step. */
  double rnd;

  do rnd = RandomNum();
   while( rnd <= 0.0 );   /* avoid zero. */
        Photon_Ptr->s = -log(rnd)/(mua+mus);
 }
 else {     /* take the leftover. */
        Photon_Ptr->s = Photon_Ptr->sleft/(mua+mus);
        Photon_Ptr->sleft = 0.0;
 }
}

/*************************************************************
 *      Check if the step will hit the boundary.
 *      Return 1 if hit boundary.
 *      Return 0 otherwise.
 *
 *      If the projected step hits the boundary, the members
 *      s and sleft of Photon_Ptr are updated.
 ****/
Boolean HitBoundary(PhotonStruct *  Photon_Ptr,
                                                InputStruct  *  In_Ptr)
{
 double dl_b;  /* length to boundary. */
 short  layer = Photon_Ptr->layer;
```

```
 double uz = Photon_Ptr->uz;
 Boolean hit;

 /* Distance to the boundary. */
 if(uz>0.0)
  dl_b = (In_Ptr->layerspecs[layer].z1
                                - Photon_Ptr->z)/uz;   /* dl_b>0. */
 else if(uz<0.0)
  dl_b = (In_Ptr->layerspecs[layer].z0
                                - Photon_Ptr->z)/uz;   /* dl_b>0. */

 if(uz != 0.0 && Photon_Ptr->s > dl_b) {
            /* not horizontal & crossing. */
  double mut = In_Ptr->layerspecs[layer].mua
                                        + In_Ptr->layerspecs[layer].mus;

  Photon_Ptr->sleft = (Photon_Ptr->s - dl_b)*mut;
  Photon_Ptr->s    = dl_b;
  hit = 1;
 }
 else
  hit = 0;

 return(hit);
}

/*************************************************************
 *          Drop photon weight inside the tissue (not glass).
 *
 * The photon is assumed not dead.
 *
 *          The weight drop is dw = w*mua/(mua+mus).
 *
 *          The dropped weight is assigned to the absorption array
 *          elements.
 ****/
void Drop(InputStruct  *          In_Ptr,
                        PhotonStruct *      Photon_Ptr,
                        OutStruct *                 Out_Ptr)
{
 double dwa;                    /* absorbed weight.*/
 double x = Photon_Ptr->x;
 double y = Photon_Ptr->y;
 double izd, ird;       /* LW 5/20/98. To avoid out of short range.*/
 short  iz, ir;         /* index to z & r. */
 short  layer = Photon_Ptr->layer;
 double mua, mus;

 /* compute array indices. */
 izd = Photon_Ptr->z/In_Ptr->dz;
 if(izd>In_Ptr->nz-1) iz=In_Ptr->nz-1;
 else iz = izd;

 ird = sqrt(x*x+y*y)/In_Ptr->dr;
 if(ird>In_Ptr->nr-1) ir=In_Ptr->nr-1;
 else ir = ird;

 /* update photon weight. */
 mua = In_Ptr->layerspecs[layer].mua;
 mus = In_Ptr->layerspecs[layer].mus;
 dwa = Photon_Ptr->w * mua/(mua+mus);
 Photon_Ptr->w -= dwa;

 /* assign dwa to the absorption array element. */
 Out_Ptr->A_rz[ir][iz]          += dwa;
}

/*************************************************************
 *          The photon weight is small, and the photon packet tries
 *          to survive a roulette.
 ****/
void Roulette(PhotonStruct * Photon_Ptr)
{
 if(Photon_Ptr->w == 0.0)
  Photon_Ptr->dead = 1;
```

```
  else if(RandomNum() < CHANCE) /* survived the roulette.*/
    Photon_Ptr->w /= CHANCE;
  else
    Photon_Ptr->dead = 1;
 }

 /*************************************************************
  *          Compute the Fresnel reflectance.
  *
  *          Make sure that the cosine of the incident angle a1
  *          is positive, and the case when the angle is greater
  *          than the critical angle is ruled out.
  *
  *          Avoid trigonometric function operations as much as
  *          possible, because they are computation-intensive.
  ****/
 double RFresnel(double n1,      /* incident refractive index.*/
                                 double n2, /* transmit refractive index.*/
                                 double ca1,          /* cosine of the incident */
                                                      /* angle. 0<a1<90 degrees. */
                                 double * ca2_Ptr)  /* pointer to the */
                                                      /* cosine of the transmission */
                                                      /* angle. a2>0. */
 {
  double r;

  if(n1==n2) {                                  /** matched boundary. **/
    *ca2_Ptr = ca1;
    r = 0.0;
  }
  else if(ca1>COSZERO) {        /** normal incident. **/
    *ca2_Ptr = ca1;
    r = (n2-n1)/(n2+n1);
    r *= r;
  }
  else if(ca1<COS90D)  {        /** very slant. **/
    *ca2_Ptr = 0.0;
    r = 1.0;
  }
  else  {                                       /** general. **/
    double sa1, sa2;
              /* sine of the incident and transmission angles. */
    double ca2;

    sa1 = sqrt(1-ca1*ca1);
    sa2 = n1*sa1/n2;
    if(sa2>=1.0) {
              /* double check for total internal reflection. */
      *ca2_Ptr = 0.0;
      r = 1.0;
    }
    else  {
      double cap, cam;  /* cosines of the sum ap or */
                                                      /* difference am of the two */
                                                      /* angles. ap = a1+a2 */
                                                      /* am = a1 - a2. */
      double sap, sam;  /* sines. */

      *ca2_Ptr = ca2 = sqrt(1-sa2*sa2);

      cap = ca1*ca2 - sa1*sa2; /* c+ = cc - ss. */
      cam = ca1*ca2 + sa1*sa2; /* c- = cc + ss. */
      sap = sa1*ca2 + ca1*sa2; /* s+ = sc + cs. */
      sam = sa1*ca2 - ca1*sa2; /* s- = sc - cs. */
      r = 0.5*sam*sam*(cam*cam+cap*cap)/(sap*sap*cam*cam);
                        /* rearranged for speed. */
    }
  }
  return(r);
 }

 /*************************************************************
  *          Record the photon weight exiting the first layer(uz<0),
  *          no matter whether the layer is glass or not, to the
  *          reflection array.
```

```
 *
 *          Update the photon weight as well.
 ****/
void RecordR(double                     Refl,       /* reflectance. */
                                InputStruct *       In_Ptr,
                                PhotonStruct *      Photon_Ptr,
                                OutStruct *         Out_Ptr)
{
 double x = Photon_Ptr->x;
 double y = Photon_Ptr->y;
 short  ir, ia;          /* index to r & angle. */
 double ird, iad;        /* LW 5/20/98. To avoid out of short range.*/

 ird = sqrt(x*x+y*y)/In_Ptr->dr;
 if(ird>In_Ptr->nr-1) ir=In_Ptr->nr-1;
 else ir = ird;

 iad = acos(-Photon_Ptr->uz)/In_Ptr->da;
 if(iad>In_Ptr->na-1) ia=In_Ptr->na-1;
 else ia = iad;

 /* assign photon to the reflection array element. */
 Out_Ptr->Rd_ra[ir][ia] += Photon_Ptr->w*(1.0-Refl);

 Photon_Ptr->w *= Refl;
}

/****************************************************************
 *          Record the photon weight exiting the last layer(uz>0),
 *          no matter whether the layer is glass or not, to the
 *          transmittance array.
 *
 *          Update the photon weight as well.
 ****/
void RecordT(double             Refl,
                                InputStruct *       In_Ptr,
                                PhotonStruct *      Photon_Ptr,
                                OutStruct *         Out_Ptr)
{
 double x = Photon_Ptr->x;
 double y = Photon_Ptr->y;
 short  ir, ia;          /* index to r & angle. */
 double ird, iad;        /* LW 5/20/98. To avoid out of short range.*/

 ird = sqrt(x*x+y*y)/In_Ptr->dr;
 if(ird>In_Ptr->nr-1) ir=In_Ptr->nr-1;
 else ir = ird;

 iad = acos(Photon_Ptr->uz)/In_Ptr->da; /* LW 1/12/2000. Removed -. */
 if(iad>In_Ptr->na-1) ia=In_Ptr->na-1;
 else ia = iad;

 /* assign photon to the transmittance array element. */
 Out_Ptr->Tt_ra[ir][ia] += Photon_Ptr->w*(1.0-Refl);

 Photon_Ptr->w *= Refl;
}

/****************************************************************
 *          Decide whether the photon will be transmitted or
 *          reflected on the upper boundary (uz<0) of the current
 *          layer.
 *
 *          If "layer" is the first layer, the photon packet will
 *          be partially transmitted and partially reflected if
 *          PARTIALREFLECTION is set to 1,
 *          or the photon packet will be either transmitted or
 *          reflected determined statistically if PARTIALREFLECTION
 *          is set to 0.
 *
 *          Record the transmitted photon weight as reflection.
 *
 *          If the "layer" is not the first layer and the photon
 *          packet is transmitted, move the photon to "layer-1".
 *
```

```
 *           Update the photon parmameters.
 ****/
 void CrossUpOrNot(InputStruct *          In_Ptr,
                                          PhotonStruct *      Photon_Ptr,
                                          OutStruct *                 Out_Ptr)
 {
  double uz = Photon_Ptr->uz; /* z directional cosine. */
  double uz1;          /* cosines of transmission alpha. always */
                                          /* positive. */
  double r=0.0;        /* reflectance */
  short  layer = Photon_Ptr->layer;
  double ni = In_Ptr->layerspecs[layer].n;
  double nt = In_Ptr->layerspecs[layer-1].n;

  /* Get r. */
  if( - uz <= In_Ptr->layerspecs[layer].cos_crit0)
    r=1.0;                 /* total internal reflection. */
  else r = RFresnel(ni, nt, -uz, &uz1);

 #if PARTIALREFLECTION
  if(layer == 1 && r<1.0) {      /* partially transmitted. */
    Photon_Ptr->uz = -uz1;       /* transmitted photon. */
    RecordR(r, In_Ptr, Photon_Ptr, Out_Ptr);
    Photon_Ptr->uz = -uz;        /* reflected photon. */
  }
  else if(RandomNum() > r) {/* transmitted to layer-1. */
    Photon_Ptr->layer--;
    Photon_Ptr->ux *= ni/nt;
    Photon_Ptr->uy *= ni/nt;
    Photon_Ptr->uz = -uz1;
  }
  else                                          /* reflected. */
    Photon_Ptr->uz = -uz;
 #else
  if(RandomNum() > r) {              /* transmitted to layer-1. */
    if(layer==1) {
      Photon_Ptr->uz = -uz1;
      RecordR(0.0, In_Ptr, Photon_Ptr, Out_Ptr);
      Photon_Ptr->dead = 1;
    }
    else {
      Photon_Ptr->layer--;
      Photon_Ptr->ux *= ni/nt;
      Photon_Ptr->uy *= ni/nt;
      Photon_Ptr->uz = -uz1;
    }
  }
  else                                          /* reflected. */
    Photon_Ptr->uz = -uz;
 #endif
 }

 /****************************************************************
  *           Decide whether the photon will be transmitted  or be
  *           reflected on the bottom boundary (uz>0) of the current
  *           layer.
  *
  *           If the photon is transmitted, move the photon to
  *           "layer+1". If "layer" is the last layer, record the
  *           transmitted weight as transmittance. See comments for
  *           CrossUpOrNot.
  *
  *           Update the photon parmameters.
  ****/
 void CrossDnOrNot(InputStruct *          In_Ptr,
                                          PhotonStruct *      Photon_Ptr,
                                          OutStruct *                 Out_Ptr)
 {
  double uz = Photon_Ptr->uz; /* z directional cosine. */
  double uz1;          /* cosines of transmission alpha. */
  double r=0.0;        /* reflectance */
  short  layer = Photon_Ptr->layer;
  double ni = In_Ptr->layerspecs[layer].n;
  double nt = In_Ptr->layerspecs[layer+1].n;
```

```
 /* Get r. */
 if( uz <= In_Ptr->layerspecs[layer].cos_crit1)
  r=1.0;                /* total internal reflection. */
 else r = RFresnel(ni, nt, uz, &uz1);

#if PARTIALREFLECTION
 if(layer == In_Ptr->num_layers && r<1.0) {
  Photon_Ptr->uz = uz1;
  RecordT(r, In_Ptr, Photon_Ptr, Out_Ptr);
  Photon_Ptr->uz = -uz;
 }
 else if(RandomNum() > r) {/* transmitted to layer+1. */
  Photon_Ptr->layer++;
  Photon_Ptr->ux *= ni/nt;
  Photon_Ptr->uy *= ni/nt;
  Photon_Ptr->uz = uz1;
 }
 else                                                    /* reflected. */
  Photon_Ptr->uz = -uz;
#else
 if(RandomNum() > r) {                  /* transmitted to layer+1. */
  if(layer == In_Ptr->num_layers) {
   Photon_Ptr->uz = uz1;
   RecordT(0.0, In_Ptr, Photon_Ptr, Out_Ptr);
   Photon_Ptr->dead = 1;
  }
  else {
   Photon_Ptr->layer++;
   Photon_Ptr->ux *= ni/nt;
   Photon_Ptr->uy *= ni/nt;
   Photon_Ptr->uz = uz1;
  }
 }
 else                                                    /* reflected. */
  Photon_Ptr->uz = -uz;
#endif
}

/*****************************************************
 ****/
void CrossOrNot(InputStruct  *   In_Ptr,
                                        PhotonStruct *      Photon_Ptr,
                                        OutStruct    *      Out_Ptr)
{
 if(Photon_Ptr->uz < 0.0)
  CrossUpOrNot(In_Ptr, Photon_Ptr, Out_Ptr);
 else
  CrossDnOrNot(In_Ptr, Photon_Ptr, Out_Ptr);
}

/*****************************************************
 *      Move the photon packet in glass layer.
 *      Horizontal photons are killed because they will
 *      never interact with tissue again.
 ****/
void HopInGlass(InputStruct  * In_Ptr,
                                        PhotonStruct * Photon_Ptr,
                                        OutStruct    * Out_Ptr)
{
 double dl;    /* step size. 1/cm */

 if(Photon_Ptr->uz == 0.0) {
        /* horizontal photon in glass is killed. */
  Photon_Ptr->dead = 1;
 }
 else {
  StepSizeInGlass(Photon_Ptr, In_Ptr);
  Hop(Photon_Ptr);
  CrossOrNot(In_Ptr, Photon_Ptr, Out_Ptr);
 }
}

/*****************************************************
 *      Set a step size, move the photon, drop some weight,
 *      choose a new photon direction for propagation.
```

```
 *
 *          When a step size is long enough for the photon to
 *          hit an interface, this step is divided into two steps.
 *          First, move the photon to the boundary free of
 *          absorption or scattering, then decide whether the
 *          photon is reflected or transmitted.
 *          Then move the photon in the current or transmission
 *          medium with the unfinished stepsize to interaction
 *          site. If the unfinished stepsize is still too long,
 *          repeat the above process.
 ****/
void HopDropSpinInTissue(InputStruct  *  In_Ptr,
                                                    PhotonStruct *  Photon_Ptr,
                                                    OutStruct    *  Out_Ptr)
{
 StepSizeInTissue(Photon_Ptr, In_Ptr);

 if(HitBoundary(Photon_Ptr, In_Ptr)) {
  Hop(Photon_Ptr);   /* move to boundary plane. */
  CrossOrNot(In_Ptr, Photon_Ptr, Out_Ptr);
 }
 else {
  Hop(Photon_Ptr);
  Drop(In_Ptr, Photon_Ptr, Out_Ptr);
  Spin(In_Ptr->layerspecs[Photon_Ptr->layer].g,
                    Photon_Ptr);
 }
}

/*************************************************************
 ****/
void HopDropSpin(InputStruct  *  In_Ptr,
                                        PhotonStruct *  Photon_Ptr,
                                        OutStruct    *  Out_Ptr)
{
 short layer = Photon_Ptr->layer;

 if((In_Ptr->layerspecs[layer].mua == 0.0)
 && (In_Ptr->layerspecs[layer].mus == 0.0))
          /* glass layer. */
  HopInGlass(In_Ptr, Photon_Ptr, Out_Ptr);
 else
  HopDropSpinInTissue(In_Ptr, Photon_Ptr, Out_Ptr);

 if( Photon_Ptr->w < In_Ptr->Wth && !Photon_Ptr->dead)
  Roulette(Photon_Ptr);
}
```

5 mcmlnr.c

```
#include <stdlib.h>
#include <stdio.h>
#include <math.h>

/*************************************************************
 *          Report error message to stderr, then exit the program
 *          with signal 1.
 ****/
void nrerror(char error_text[])

{
 fprintf(stderr,"%s\n",error_text);
 fprintf(stderr,"...now exiting to system...\n");
 exit(1);
}

/*************************************************************
 *          Allocate an array with index from nl to nh inclusive.
 *
 *          Original matrix and vector from Numerical Recipes in C
 *          don't initialize the elements to zero. This will
 *          be accomplished by the following functions.
 ****/
double *AllocVector(short nl, short nh)
```

```
{
 double *v;
 short i;

 v=(double *)malloc((unsigned) (nh-nl+1)*sizeof(double));
 if (!v) nrerror("allocation failure in vector()");

 v -= nl;
 for(i=nl;i<=nh;i++) v[i] = 0.0;   /* init. */
 return v;
}

/*************************************************************
 *          Allocate a matrix with row index from nrl to nrh
 *          inclusive, and column index from ncl to nch
 *          inclusive.
 ****/
double **AllocMatrix(short nrl,short nrh,
                                                    short ncl,short nch)
{
 short i,j;
 double **m;

 m=(double **) malloc((unsigned) (nrh-nrl+1)
                                                    *sizeof(double*));
 if (!m) nrerror("allocation failure 1 in matrix()");
 m -= nrl;

 for(i=nrl;i<=nrh;i++) {
  m[i]=(double *) malloc((unsigned) (nch-ncl+1)
                                                    *sizeof(double));
  if (!m[i]) nrerror("allocation failure 2 in matrix()");
  m[i] -= ncl;
 }

 for(i=nrl;i<=nrh;i++)
  for(j=ncl;j<=nch;j++) m[i][j] = 0.0;
 return m;
}

/*************************************************************
 *          Release the memory.
 ****/
void FreeVector(double *v,short nl,short nh)
{
 free((char*) (v+nl));
}

/*************************************************************
 *          Release the memory.
 ****/
void FreeMatrix(double **m,short nrl,short nrh,
                                    short ncl,short nch)
{
 short i;

 for(i=nrh;i>=nrl;i--) free((char*) (m[i]+ncl));
 free((char*) (m+nrl));
}
```

Reference

1. Web site of Oregon Medical Laser Center at Providence St. Vincent Medical Center, http://omlc.ogi.edu/software/mc/

Appendix B
Validation of Difference Method to Solve the One-Dimensional Transient Form of the Heat Conduction Problems

The intended application requires the model to predict the surface temperature given the thermal properties, thickness, L, and initial temperature, T_i. Specifically, it is needed to assess whether the model can be used to assess compliance with the regulatory requirement given in Eq. (5.2). Comparison with the exact solution is planned to understand the accuracy of the model for the intended application. These activities are discussed next.

Imposed Boundary Temperature in Cartesian Coordinates

A simple but important conduction heat transfer problem consists of determining the temperature history inside a solid flat wall which is quenched from a high temperature. More specifically, consider the homogeneous problem of finding the one-dimensional temperature distribution inside a slab of thickness L and thermal diffusivity α, initially at some specified temperature $T(x, 0) = f(x)$ and exposed to heat extraction at its boundaries $x = 0$ and $x = L$ such that $T(0, t) = T(L, t) = 0$ (Dirichlet homogeneous conditions), for $t > 0$. The thermal properties are assumed constant.

The mathematical statement of the heat equation for this problem is[1,2]:

$$\frac{\partial T(x,t)}{\partial t} = \alpha \frac{\partial T(x,t)}{\partial x^2} \tag{B.1}$$

subject to

$$T(0,t) = T(L,t) = 0 \tag{B.2}$$

and

$$T(x,0) = f(x) \tag{B.3}$$

for all x when $t = 0$.

As indicated before, the method of separation of variables starts by assuming the solution to this problem has the following particular form

$$T(x,t) = X(x)\Gamma(t) \tag{B.4}$$

Introducing the above assumption into the heat equation and rearranging yields

$$\frac{1}{X}\frac{\mathrm{d}^2X}{\mathrm{d}x^2} = \frac{1}{\alpha\Gamma}\frac{\mathrm{d}\Gamma}{\mathrm{d}t} \tag{B.5}$$

However since $X(x)$ and $\Gamma(t)$, the left hand side of this equation is only a function of x while the right hand side is a function only of t. For this to avoid being a contradiction (for arbitrary values of x and t) both sides must be equal to a constant. For physical reasons (in this case we obviously are after a temperature function that either increases or decreases monotonically depending on the initial conditions and the imposed boundary conditions), the required constant must be negative; let me call it $-\omega^2$.

Therefore, the original heat equation, (a partial differential equation) is transformed into the following equivalent system of ordinary differential equations

$$\frac{1}{\alpha\Gamma}\frac{\mathrm{d}\Gamma}{\mathrm{d}t} = -\omega^2 \tag{B.6}$$

and

$$\frac{1}{X}\frac{\mathrm{d}^2X}{\mathrm{d}x^2} = -\omega^2 \tag{B.7}$$

General solutions to these equations are readily obtained by direct integration and are

$$\Gamma(t) = C\exp(-\omega^2\alpha t) \tag{B.8}$$

and

$$X(x) = A'\cos(\omega x) + B'\sin(\omega x) \tag{B.9}$$

Substituting back into our original assumption yields

$$T(x,t) = X(x)\Gamma(t) = [A\cos(\omega x) + B\sin(\omega x)]\exp(-\omega^2\alpha t) \tag{B.10}$$

where the constant C has been combined with A′ and B′ to give A and B without loosing any generality.

Now we introduce the boundary conditions. Since $T(0, t) = 0$, necessarily A = 0. Furthermore, since also $T(L, t) = 0$, then $\sin(\omega L) = 0$ (since $B = 0$ is an uninteresting trivial solution.) There is an infinite number of values of ω which satisfy this conditions, i.e.

$$\omega_n = \frac{n\pi}{L} \tag{B.11}$$

with $n = 1, 2, 3, \ldots$. The ω_n's are the eigenvalues and the functions $\sin(\omega_n x)$ are the eigenfunctions of the Sturm-Liouville problem satisfied by the function $X(x)$. These

eigenvalues and eigenfunctions play a role in heat conduction analogous to that of the deflection modes in structural dynamics, the vibration modes in vibration theory and the quantum states in wave mechanics.

Note that each value of ω_n yields an independent solution satisfying the heat equation as well as the two boundary conditions. Therefore we have now an infinite number of independent solutions $T_n(x, t)$ for $n = 1, 2, 3, \ldots$ given by

$$T_n(x,t) = [B_n \sin(\omega_n x)]\exp(-\omega_n^2 \alpha t) \tag{B.12}$$

The principle of superposition allows the creation of a more general solution from the particular solutions above by simple linear combination to give

$$T(x,t) = \sum_{n=1}^{\infty}[B_n \sin(\omega_n x)]\exp(-\omega_n^2 \alpha t) = \sum_{n=1}^{\infty}[B_n \sin(\frac{n\pi x}{L})]\exp(-(\frac{n\pi}{L})^2 \alpha t) \tag{B.13}$$

The final step is to ensure the values of the constants B_n are such that they satisfy the initial condition, i.e.

$$T(x,0) = f(x) = \sum_{n=1}^{\infty} B_n \sin(\frac{n\pi x}{L}) \tag{B.14}$$

But this is just the Fourier sine series representation of the function $f(x)$.

Recall that a key property of the eigenfunctions is that of orthonormality property. This is expressed here as

$$\int_0^L \sin(\frac{n\pi x}{L})\sin(\frac{m\pi x}{L})\mathrm{d}x = 0, (when\ n \neq m)\ or\ L/2, (when\ n = m) \tag{B.15}$$

Using the orthonormality property one can multiply the Fourier sine series representation of $f(x)$ by $\sin(m\pi x/L)$ and integrate from $x = 0$ to $x = L$ to produced the result

$$B_n = \frac{2}{L}\int_0^L f(x)\sin(\frac{n\pi x}{L})\mathrm{d}x \tag{B.16}$$

for $n = 1,2,3,....$

Finally, the resulting B_n's can be substituted into the general solution above to give

$$T(x,t) = \sum_{n=1}^{\infty} T_n(x,t) = \sum_{n=1}^{\infty}[\frac{2}{L}\int_0^L f(x')\sin(\frac{n\pi x'}{L})]\sin(\frac{n\pi x}{L})\exp(-\frac{n^2\pi^2\alpha t}{L^2}) \tag{B.17}$$

Explicit expressions for the B_n's can be readily obtained for simple $f(x)$'s, for instance if

$$f(x) = T_i = \text{constant} \tag{B.18}$$

then

$$B_n = -T_i \frac{2(-1+(-1)^n)}{n\pi} \tag{B.19}$$

Simulation Parameters

The parameters in difference method used as shown in table B.1. Length of the space is fixed as 6 m. Simulation #1 mimics the low spatial resolution Δx. Simulation #2 mimics the higher time resolution Δt than simulation #1. Simulation #3 mimics the higher spatial resolution than simulation #1. The initial temperature was 20 ˚C. After time $t = 0$, the temperature at the boundaries are simulated as 0 ˚C. The exact solution is calculated with parameter in table B.1 and Eq. (B.13).

Results and Discussion

Figure B.1 shows the results of simulation #1. Temperature of difference method is not coincident with the exact solution. Figure B.2 indicates the relative error of difference method in the simulation #1. The maximum error was 14% at $t = 1$ s. Figure B.3 and B.4 show the results of simulation #2. The maximum error of temperature distribution was 2.5%. The error decreased by increase of time resolution. Figure B.5 and B.6 show the results of simulation #3. The solution of difference method is consistent with the exact solution. The error was under 0.5% in the simulation #3.

These results indicate that the time resolution and spatial resolution are the important parameter for accurate simulation. For the appropriate simulation with difference method, the spatial resolution of ten-to-one of the length of geometry may be better.

Conclusions

The precision of difference method was validated by comparison with exact results. The difference method had high precision. The validation of the difference method was observed.

Reference

1. Rensselaer Hartford, http://www.ewp.rpi.edu/hartford/

2. 登坂宣好、大西和榮、偏微分方程式の数値シミュレーション、平文社、1991.

Figures

Table B.1 Simulation parameters in difference method and exact solution.

	Simulation #1	Simulation #2	Simulation #3
L [m]	6	6	6
α [m^2/s]	1	1	1
Δt [s]	0.5	0.01	0.005
Δx [m]	1	1	0.1

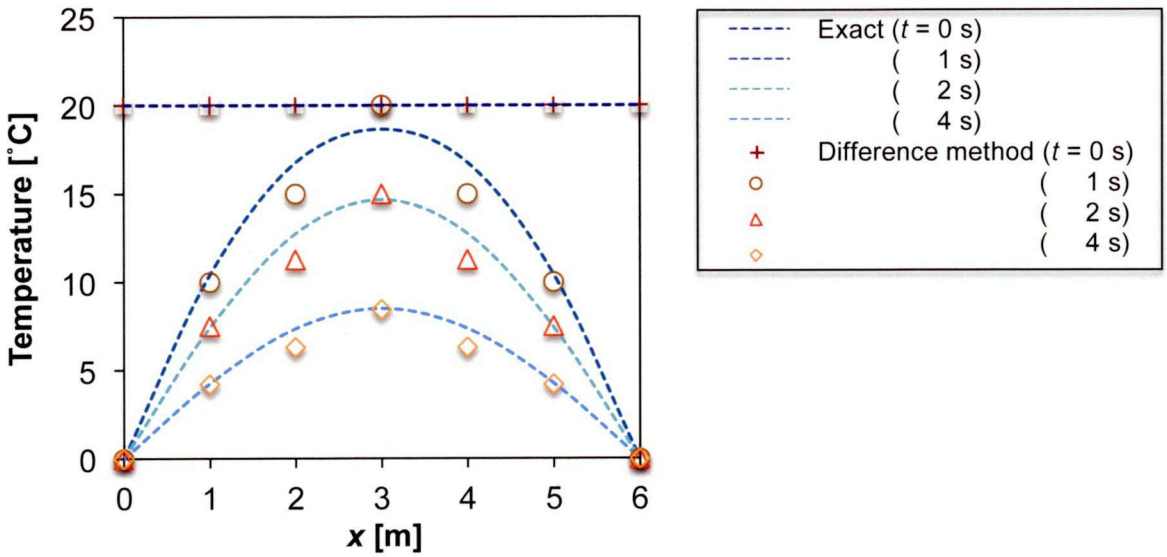

Fig. B.1 Temperature distribution in simulation #1.

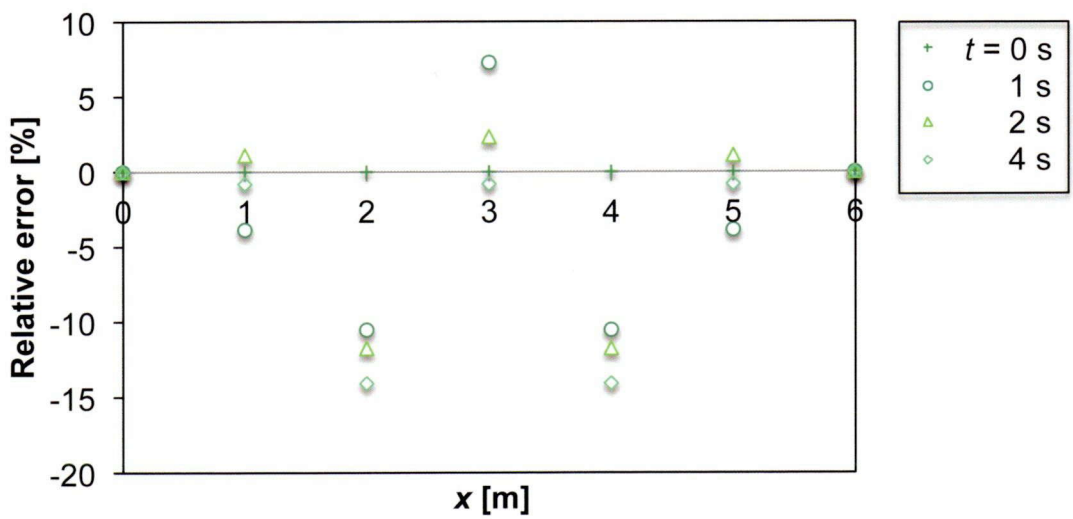

Fig. B.2 Relative error in simulation #1.

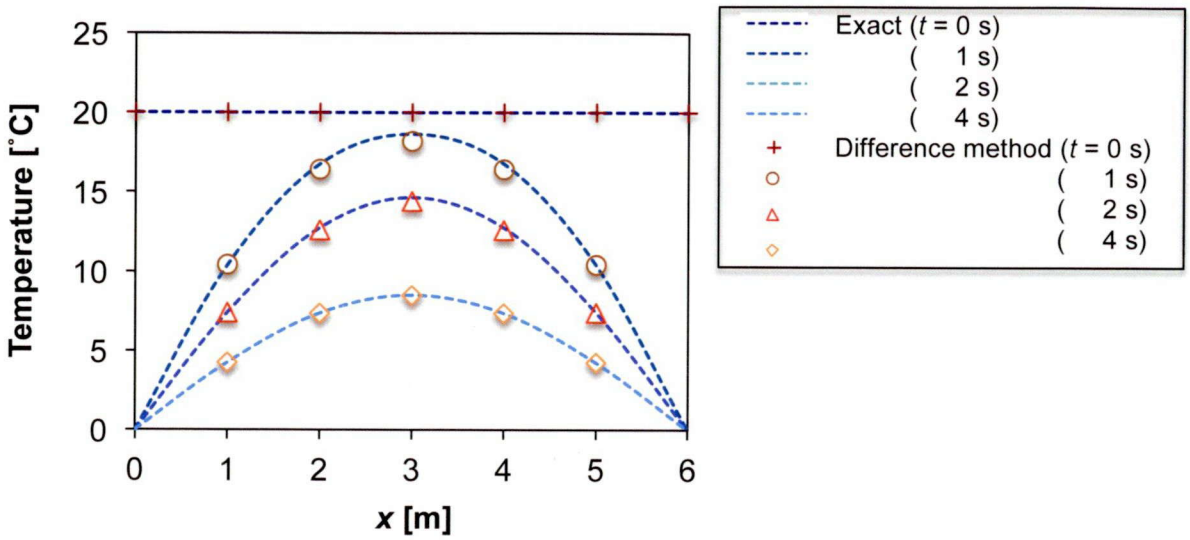

Fig. B.3 Temperature distribution in simulation #2.

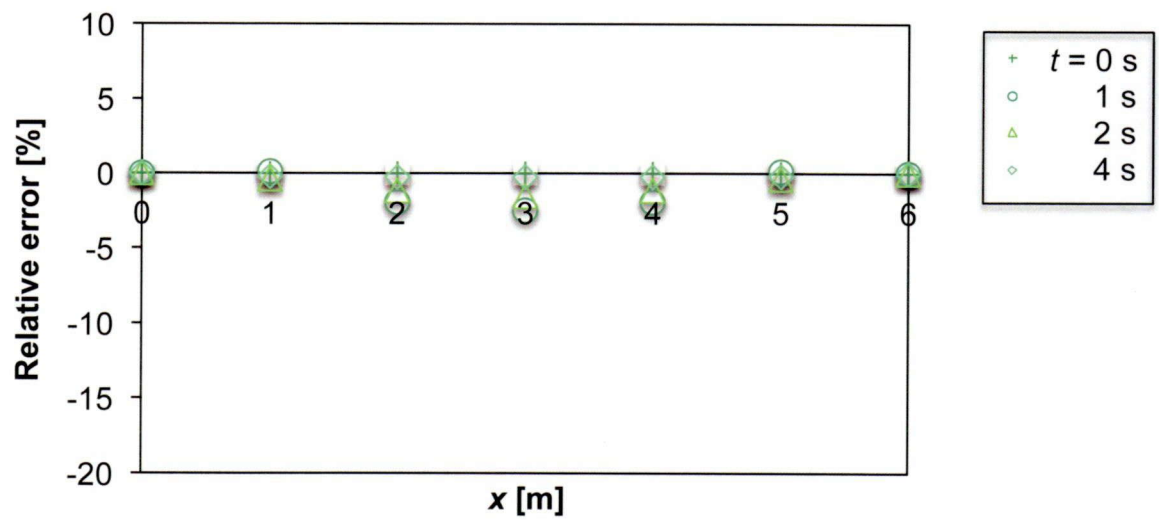

Fig. B.4 Temperature distribution in simulation #2.

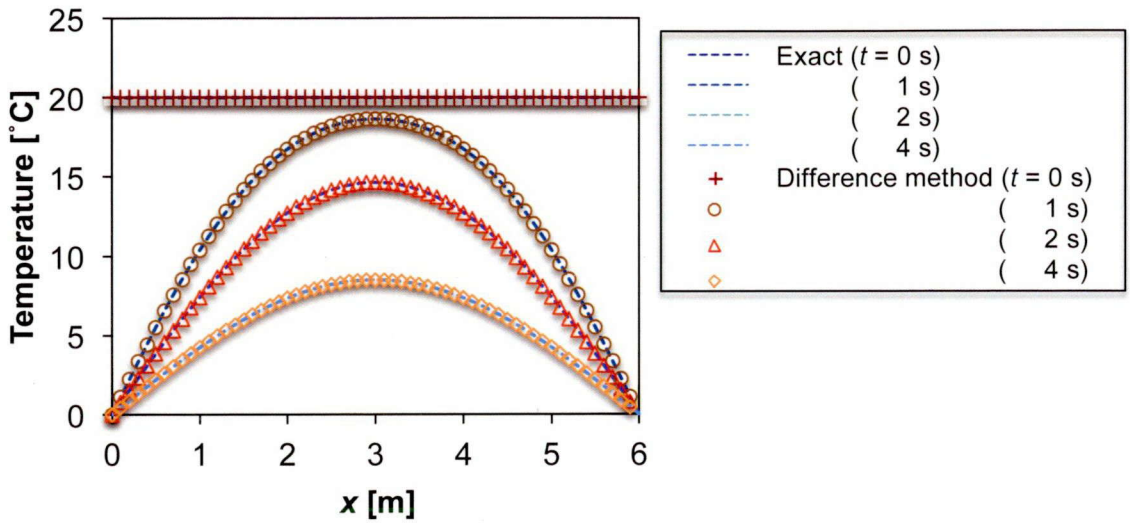

Fig. B.5 Temperature distribution in simulation #3.

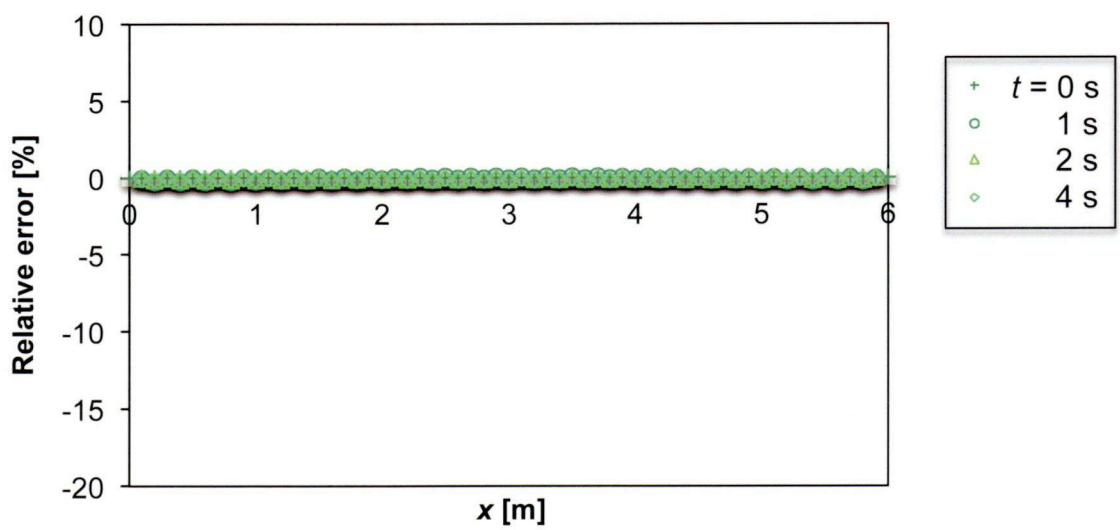

Fig. B.6 Relative error in simulation #3.